Synthesis and Photoluminescence Properties of Novel Red Phosphors for White Light Emitting Diode Applications

Thesis submitted to
Cochin University of Science and Technology

In partial fulfillment of the requirements for the award of the degree of

Doctor of Philosophy

in
Physics

under
The Faculty of Science

by
LINDA FRANCIS T.

**Materials Science and Technology Division
CSIR - National Institute for Interdisciplinary
Science and Technology (NIIST)
Thiruvananthapuram - 695019
Kerala, India**

Synthesis and Photoluminescence Properties of Novel Red Phosphors for White Light Emitting Diode Applications

PhD Thesis in the field of Materials Science

_____

Author:
Linda Francis T.
Materials Science and Technology Division
National Institute for Interdisciplinary
Science and Technology (NIIST)
Thiruvananthapuram - 695019, Kerala, India

Supervising Guide:
Dr. P. Prabhakar Rao
Materials Science and Technology Division
National Institute for Interdisciplinary
Science and Technology (NIIST)
Thiruvananthapuram - 695019, Kerala, India

_____

August 2015

DECLARATION

       I hereby declare that the work presented in this thesis entitled "**Synthesis and Photoluminescence Properties of Novel Red Phosphors for White Light Emitting Diode Applications**" is based on the original research work done by me at the Materials Science and Technology Division, National Institute for Interdisciplinary Science and Technology (NIIST), CSIR, Thiruvananthapuram, under the supervision of **Dr. P. Prabhakar Rao**, Chief Scientist and has not been included in any other thesis submitted previously for the award of any degree.

Linda Francis T.

Thiruvananthapuram
Date:

COUNCIL OF SCIENTIFIC AND INDUSTRIAL RESEARCH
NATIONAL INSTITUTE FOR INTERDISCIPLINARY
SCIENCE AND TECHNOLOGY (CSIR-NIIST)
Industrial Estate P.O., Trivandrum - 695 019
Kerala, India

ISO 9001 REGISTERED

MGMT. SYS.
RvA C 074
DNV Certification B V The Netherlands

Dr. P. Prabhakar Rao
Chief Scientist & Head
Materials Science and Technology
Division

Tel: 91-471-2515 311
Fax: +91-471-2491 712
E-mail: padala_rao@yahoo.com

CERTIFICATE

Certified that the work presented in this thesis entitled **"Synthesis and Photoluminescence Properties of Novel Red Phosphors for White Light Emitting Diode Applications"** is based on the authentic record of research done by Ms. Linda Francis T. under my guidance in the Materials Science and Technology Division of National Institute for Interdisciplinary Science and Technology (NIIST), CSIR, Thiruvananthapuram, for the degree of Doctor of Philosophy under the faculty of Science, Cochin University of Science and Technology and has not been included in any other thesis submitted for the award of any degree.

Thiruvananthapuram
Date: 10 · 08 · 2015

Dr. P. Prabhakar Rao
(Supervising guide)

An experiment is a question which science poses to Nature,
and a measurement is the recording of Nature's answer

Max Planck (1858-1947)

Acknowledgements

Life at NIIST was made easier and happier with a bunch of dear friends who always wished for my happiness and who constantly supported me. I truly cherish the memories with Mrs. Reshmi, Mrs. Anupama, Ms. Subha, Mrs. Sumi, Mrs. Ramya, Ms. Usha and Ms. Sudhakshina. We had our second home together on the upstairs of our dear house owner Sishupalan sir, where our loud laughters and silly jokes took over every tensions from work. I remember the beautiful times spent with Mr. Maneesh, Mr. Sudhish, Mr. Vijay, Mr. Binish, Mr. Vaisakhan, Ms. Lekshmi and Mr. Suneesh over these years. I love them for being with me. I would like to have more cups of coffee from NIIST kiosk together with Divya, Parvathi, Vaisakhan, Arya, Dhaneesh, Shaban, Hari and Suneeth. I was thinking for days how to express my love for my girls, Mrs. Ramya and Ms. Usha. I declare my failure for their care and support.

With a heart full gratitude and love, I mark my gratefulness to all my teachers, especially from St. Thomas College, Thrissur and Cochin University of Science and technology, who taught me the beautiful subject of physics opening my way to research life. I truly treasure the friendship with people from CUSAT specially Ms. Arya, Mrs. Monisha, Ms. Jerin, Mrs. Sumithra, Mr. Anand, Mr. Shijeesh, Mr. Sajan who always supported me even after joining NIIST. I also remember Mr. Arun Aravind and Mr. Aneesh P. M. for their affection and care.

Words really turns off to express my happiness to have found my partner and best friend in Mr. Joseph Dony, who could perfectly understand my words, silence and even more. He was the sole reason for the completion of this work which might have been dropped at many stages.

I always had three people behind me, loving, pampering, supporting, encouraging and understanding me from my very first day in life. I feel extremely blessed to have been born as the daughter of Mr. Francis T. A. and Mrs. Jessy Francis, and as a little sister to my lovely brother Dr. Shinto Francis. I love my parents-in-law, (Mr. Dony C. J. and Mrs. Maria Dony) for treating me like a daughter. I am extremely happy to have two dear sisters, Dr. Elizabeth Dony and Dr. Ann Thomas who supports me always.

Writing this thanking note was more like a walk through my life where many faces came in and out. I missed many names; some because of my poor memory and some as the list is getting longer and longer. I thank one and all for your timely interference into my life making it happier and meaningful. Thank you all.

Linda Francis T.

CONTENTS

List of Tables

List of Figures

xv

Abbreviations

SSL	: Solid State Lighting
CCT	: Correlated Color Temperature
CRI	: Color Rendering Index
CIE	: Commission Internationale de I' Eclairage
K	: Kelvin
LED	: Light Emitting Device
OLED	: Organic Light Emitting Diodes
WLED	: White Light Emitting Diode
RGB	: Red Green and Blue
UV	: Ultraviolet
pc-WLED	: Phosphor Converted White Light Emitting Diode
YAG	: Yttrium Aluminium garnet
InGaN	: Indium Gallium Nitride
CN	: Co-ordination Number
ET	: Energy transfer
CTS	: Charge Transfer States
CRT	: Cathode Ray Tube
QE	: Quantum Efficiency
RE	: Rare Earth
PL	: Photoluminescence
Ln	: Lanthanide
XRD	: X-Ray Diffraction
SEM	: Scanning Electron Microscope
EDS	: Energy Dispersive Spectroscopy
FT-IR	: Fourier Transform Infrared
ED	: Electric Dipole
MD	: Magnetic Dipole
CTB	: Charge Transfer Band
EM	: Emission
EX	: Excitation
SG	: Space Group
FWHM	: Full Width at Half Maximum
PL	: Photoluminescence
J-O	: Judd O-Felt
ICDD	: International Centre for diffraction data
NTSC	: National Television Standards Committee

PREFACE

White light emitting diodes (WLEDs) are considered to be the next generation lighting devices. Their substitution for fluorescent or incandescent lamps would lead to considerable energy savings. Apart from that, they can offer benefits in terms of high luminous efficiency, good reliability, long lifetime and environmental protection. Different methods are available to mimic white light from blue/near-UV LEDs. The combination of blue chip and yellow phosphors has already been developed and is commercially available which has poor color rendering index (CRI) due to deficiency in the red region. To overcome this problem, another method is to employ a soft UV chip emitting ~400 nm wavelength with red, green and blue (RGB) phosphors. Most of current red phosphors are based on Eu^{2+} ions in different hosts like nitrides, silicates and oxides whose emission is very broad, spilling over to deep red emission which are undesirable as human eye is insensitive to that wavelength region. Eu^{3+} ions are considered to be preferable choice of activators for narrow red luminescence as they exhibit a high lumen equivalent, quantum efficiency and photostability. Sulfide based red phosphors are currently used in that approach which is highly harmful to the environment and lacks chemical stability. In addition, the current red phosphor cannot absorb light efficiently in UV region and its brightness is about 8 times less than that of the available green and blue phosphors. Thus in view of the great importance of red phosphors in the development of white LEDs in the lighting industry, the study of Eu^{3+} luminescence in various host systems gains attraction. The emission characteristics of Eu^{3+} highly depend on the crystal structure of the host lattice, doping site, doping concentration, cationic ordering of the host lattice, uniformity in the activator distribution and various other factors. Rare earth niobates, antimonates and tantalates

with a general formula, Ln_3MO_7 have huge compositional and structural diversity and gained much attraction as functional materials in various applications. The proposed system, Ln_3TaO_7 provides an ample scope to study the photoluminescence properties in relation with their crystal structures. Also, Eu^{3+} activated Ln_3MO_7 structures have good absorptions in the near UV region matching well to the emissions of UV chip. The main objective of the present research work is to determine various structural influencing parameters and thereby develop novel red phosphor materials for phosphor converted (pc) WLEDs.

The present thesis is organized into seven chapters. Introduction chapter details solid state lighting technology and various approaches to white light generation. Emphasis is given on the electronic and luminescence properties of Eu^{3+} along with a brief literature review of Eu^{3+} luminescence in various host lattices. Main objectives of the current work are highlighted and the motivation and importance of choosing Ln_3MO_7 host structures is stressed. A brief discussion on the conventional solid state reaction route adopted for the preparation of the samples under study and different characterization techniques employed are given in chapter two.

Third chapter correlates the photoluminescence properties of $Gd_{3-x}MO_7$ (M = Nb, Sb, Ta) : xEu^{3+} phosphors to their crystal structure. It was observed that more ordering occurs in the lattice when an M site is doped from Sb to Nb to Ta. Due to the more ordered structure of the Gd_3TaO_7 host lattice resulting in a more uniform distribution of Eu^{3+} ions, the tantalate system showed better luminescence properties. The variation in the luminescence intensity with various Eu^{3+} concentrations in the Gd_3TaO_7 host lattice was also studied to calculate the optimum doping concentration.

Influence of various lanthanide ion (Lu, Y, Gd, La) substitution on the Eu^{3+} photoluminescence properties in Ln_3MO_7 host structures

are discussed in the fourth chapter. Results demonstrate that the long range ordering, coordination of cations and ligand polarizability influenced significantly the emission probabilities, intensity and quantum efficiency of these phosphor materials. An unusual photoluminescence of almost equally competing intensities from all the 4f transitions of Eu^{3+} ($^5D_0 \rightarrow {}^7F_{0,1,2,4}$) was noticed for La_3TaO_7 system. The effect of Eu^{3+} doping concentration on the emission characteristics of La_3TaO_7 phosphors was also discussed in relation to the phase evolution.

Based on the studies described in the chapters three and four we further tried to enhance the photoluminescence properties by compositional variation. With a view to increase the polarizability around the Eu^{3+} ion and for improving the ordering in the host lattice Ba^{2+} ions were introduced in La^{3+} site. The trend in the photoluminescence properties with respect to Ba^{2+} substitution was analysed and the influencing parameters were well studied which are discussed in chapter five.

Chapter six details the synthesis and characterization of novel red phosphor materials $Gd_{2-x}GaTaO_7 : xEu^{3+}$ that could be effectively excited by UV light exhibiting intense red emissions. Red-shift in the charge transfer band coupled with increased emission intensity in the red region ~ 612 nm was observed with Bi^{3+} co-doping. Optimal doping level of Eu^{3+} and Bi^{3+} in Gd_2GaTaO_7 host was determined from the photoluminescence studies. The prepared samples exhibited higher emission intensities than the standard $Y_2O_3 : Eu^{3+}$ red phosphors.

Conclusions drawn from the studies on the structural aspects and the Eu^{3+} photoluminescence properties in these closely related host structures which will help in the design of efficient red phosphors for pc-WLED applications are presented in chapter seven.

<div align="right">

1

</div>

PHOSPHORS - AN OVERVIEW

_____

Solid state lighting technology and the study of phosphor materials are the hot topics of current research. In this chapter, a revision on the various lighting techniques and a basic understanding of the solid state lighting are discussed. Emphasis is given to the electronic and luminescence properties of Eu^{3+} ions as a component for red phosphors along with a brief literature review of Eu^{3+} luminescence in various host lattices. Key objectives of the current work are highlighted and the motivation and importance of choosing Ln_3MO_7 host structures are stressed.
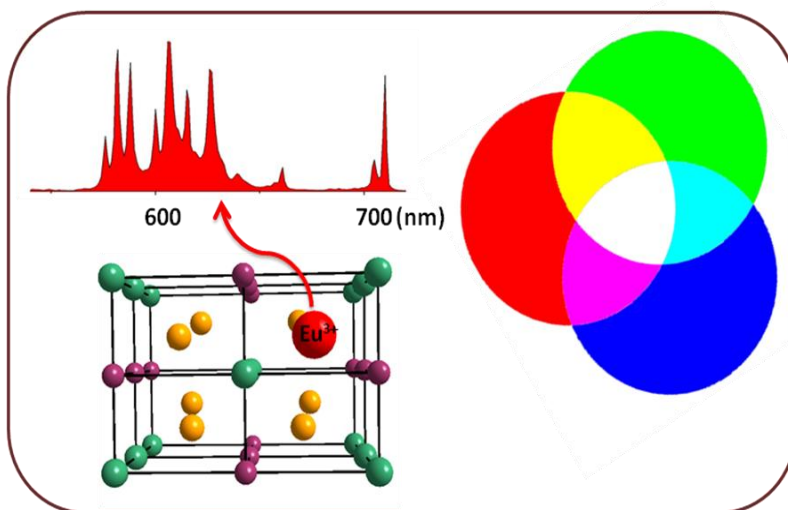
1.1 General introduction

Energy is an essential commodity in our lives, and the use of energy is increasing with industrial development. Lighting plays a vital role in our everyday lives as well as in commerce and industry worldwide, and it consumes considerable amount of the total energy produced. Energy efficiency is one of the most effective means to meet the requirements. Considering the growing demand for high - efficiency lighting devices, various scientists all over the world are working to meet this challenge. For the near future, solid state lighting (SSL) is emerging as a promising lighting technology replacing conventional lighting sources like incandescent, fluorescent and high intensity discharge lamps. Coupled with the energy savings, environmental safety and aesthetic quality are dealt in the solid state lighting technology.

1.2 Common lighting technologies: A comparative study

Discovery of fire by the very ancient people marks the earliest form of artificial lighting. Over the time, human brain worked to meet the need for a better light source and therefore various technologies were developed. Among them, incandescent and fluorescent lights ruled the lighting industry for a long time. Incandescent bulbs emit light when an electrical current causes a tungsten filament to glow. But the major limitation is the lesser efficiency (efficacy) when evaluating them on a lumen (amount of light emitted) output to energy input basis. About 90 percent of the energy used for the bulb is emitted as heat rather than light [1]. Halogen bulbs are a type of incandescent lamps that are slightly more efficient than standard incandescent. Fluorescent lights offered somewhat better efficiency using about 75% lesser energy than the incandescent lamps [2]. The phenomenon of fluorescence occurs as the electric current in the gas excites mercury vapour which produces short

wave ultraviolet light that then causes a phosphor coating on the inside of the bulb to glow. They come in different shapes and sizes like fluorescent tubes, CFL (compact fluorescent lamps) with varying efficiencies. The hazardous waste mercury used in this makes the light sources a threat to the environment. High intensity discharge lamps and low pressure sodium lamps also find a place in this list of lighting devices but are limited to certain outdoor applications due to long startup and cool down time. Unlike incandescent or fluorescent lamps which create light with filaments and gasses encased in a glass bulb, solid state lighting uses semiconductors that convert electricity into light [3]. As per the data and studies by US department of energy, with this new array of lighting sources (LED) an energy saving of about 217 terawatt hours, 31.4 million metric ton reduction in carbon is expected by the year 2025 [4]. As this technology develops, the cost of production of these LED lights is likely to decline, making them more economical. In order to choose a suitable light source a basic understanding of some defining factors like efficacy, lifetime, correlated color temperature (CCT), color rendering index (CRI), CIE (Commission Internationale de l'Eclairage) color coordinates etc is needed. Brief description of these factors is given below.

1.2.1 Efficacy

This term determines how much energy is converted to light by the source, and how well the emitted radiation is detected by the human eye. A more accurate way to compare the performance of various sources is to measure the luminaries designed for and lamped with each type of source. The metric used for comparison is called luminarie efficacy, expressed in lumens per watt (lm/W). It is the ratio of luminous flux to power [5].

1.2.2 Lifetime

The lifetime of a lamp depends on the application as well as the environment in which it is used. Incandescent or florescent lights burn out over time. In LED lighting lumen depreciation (slowly dimming overtime due to the heating at the junction) occurs. The lifetime of LEDs is measured based on the number of operating hours until the LED is emitting 70 percent of its initial light output.

1.2.3 Correlated color temperature (CCT)

CCT is defined as the absolute temperature of a black body that has the same color as that of the light source [5, 6]. As the temperature increases, hot objects will sequentially glow in red, orange, yellowish white and bluish white. Most simply, CCT can be explained as a method of describing the color characteristics of light, usually either warm (yellowish, low CCT) or cool (bluish, high CCT), by measuring it in degrees of Kelvin (K). Typical CCT of the white region in the diagram range between 2500 and 10000 K. Light sources that are not incandescent radiators have a correlated color temperature. Lights with a correlated color temperature does not have an equal radiation at all wavelengths in their spectrum. As a result, they can have disproportionate levels (both high & low) when rendering certain colors.

1.2.4 Color rendering index (CRI)

It is a figure of merit, on a scale of 0 to 100, which gives a quantitative measure of the ability of a light source to reproduce the colours of various objects faithfully in comparison with an ideal or natural light source [5]. The lower the CRI rating, the less accurately colors will be reproduced. Light sources that are incandescent radiators have high CRI since all colors in their spectrum are rendered equally. A

light source with CRI greater than 90 can be considered good in color rendering. CRI is calculated from the differences in the chromaticities of eight CIE standard color samples (CIE 1995) when illuminated by a light source and by a reference illuminate of the same correlated color temperature [5]. The smaller the average differences in chromaticities, the higher the CRI.

1.2.5 CIE color coordinates

CIE color coordinate diagram as introduced by Commission Internationale de l'Eclairage in 1931 represents all of the chromaticities visible to the average person on a scale of *x* and *y* [7 - 10]. Results from a series of experiments by William David Wright and John Guild were combined into the specification of the CIE red, green and blue (RGB) color space, from which the CIE XYZ color space was derived. A color space is a three dimensional space specified by a set of three numbers (tristimulus values X, Y and Z) which determine the color and brightness of a particular homogeneous visual stimulus. A chromaticity is a color projected into a two dimensional space that ignores brightness. The standard CIE XYZ color space projects directly to the corresponding chromaticity space specified by the two chromaticity coordinates known as x and y, creating the familiar chromaticity diagram shown in figure 1.1. The "horseshoe" curve consists of the chromaticity points of every color of light whose spectrum consists of only a single wavelength. All colors of visible light have chromaticities represented by points inside the region bounded by the horseshoe. According to the chromaticity diagram, the primary colors red, blue and green are represented as (0.67, 0.33), (0.14, 0.08), (0.21, 0.71) respectively. The CIE color coordinate of pure white is (0.33, 0.33).
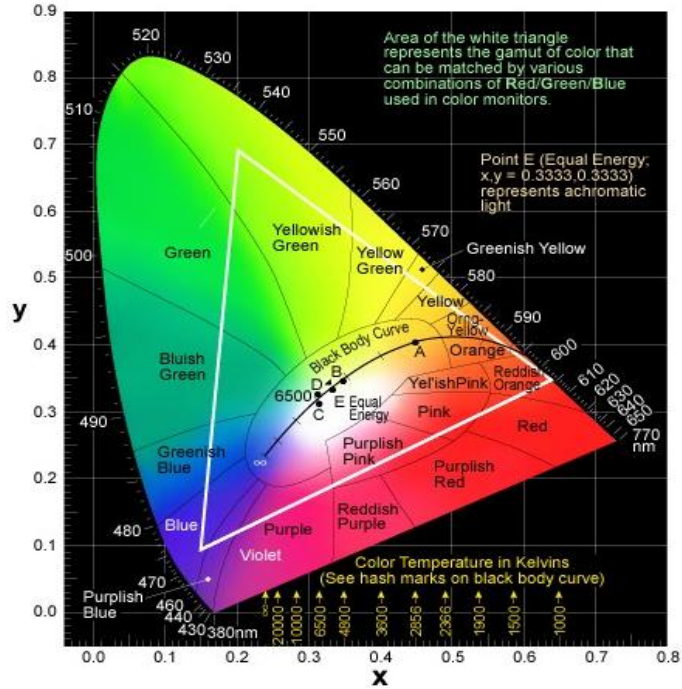
Figure 1.1 1931 CIE chromaticity coordinate diagram.

A comparative analysis of various light sources in terms of these defining parameters are given in table 1.1. A very quick look itself proves the importance of LED light sources over other traditional sources.

Table 1.1 Efficacy, lifetime, CCT and CRI of various light sources [11, 12, 13].

Light source	Incandescent	Halogen	Fluorescent	Metal halide	White LED
Efficacy (lm/W)	7 - 20	15 - 20	50 - 100	80 - 110	90 - 120
Lifetime (hrs)	750 - 2000	2000 - 4000	9000 - 20000	5000 - 20000	50000+
CCT (K)	2500 - 3000	2800 - 3150	2700 - 7500	4000	2700- 10000
CRI	>95	100	70-85	70	70-90

1.3 Solid state lighting: LED technology

The rapid improvement of the white light efficacy achievable with light emitting diodes (LEDs) opens up new opportunities in the general illumination market. Lighting applications using light emitting diodes, organic light emitting diodes (OLEDs), or light emitting polymers are commonly referred to as solid state lighting. The history of solid state lighting dates back to 1907 when H. J. Round discovered a green glow in the silicon carbide diode junction [14]. Another contemporary scientist Losev, also made the similar observation [15]. However, these major invention remained largely unnoticed for a long period. The first commercial LEDs were introduced in the 1960s, but there was almost no application besides those in numeric displays or indicator lights [16]. A significant development took place as the scientist Shuji Nakamura fabricated double-heterostructure InGaN/GaN blue LED chips in 1993 [17]. The first white light emitting diode (WLED) was brought to the commercial market by Nichia Corporation in 1996 [18]. The emphasis on research on SSL has gained tremendous momentum in the past decade due to their inherent advantages like high light efficiency, low energy consumption and long service lifetime compared to other conventional light sources. Thus, SSL is emerging as an extremely competent field and a possible alternative to existing lighting technologies. These systems are still on its way to out throw fluorescent lighting in price and efficiency. However, the already achieved performance concerning the lifetime and internal efficiency clearly indicates their future potential.

Unlike other light sources, LEDs are not inherently white light sources and they emit nearly monochromatic light. This makes them highly efficient for colored light applications such as traffic lights and exit signs. LEDs are basically semiconductor materials doped with

impurity elements to create a p-n junction. These diodes emit light when a suitable voltage is applied between their leads, and the color of the light depends on the bandgap of the semiconductor materials. However, to be used as a general light source, generation of white light from these monochromatic sources is needed.

1.4 Approaches towards white light generation

There are various approaches to get efficient solid state sources for the white light generation [19, 20]. Three different methods are employed most commonly. In the first approach, light from three monochromatic LED sources, red, green and blue (RGB) are mixed directly so as to produce a white light. Second method is to use an ultraviolet (UV) LED to excite three different phosphors (red, green and blue) coated over the epoxy layers in such a way that none of the pump LED light is allowed to escape. In this case the emission from the three different phosphors results in the mixing of primary colors producing white light. One can also adopt the binary complimentary method for white light generation. Here a blue LED is used to pump a yellow phosphor that has been integrated into the phosphor converted LED (pc-LED) package. The pc-LED is designed to leak some of the blue light beyond the phosphor to generate the blue portion of the spectrum, while the phosphor emits yellow light. In order to improve the color rendering, more visible light emitting phosphors can be coated to convert the remainder of the blue light into the red and green portions of the spectrum. These three different approaches for the white light generation are schematically represented in figure 1.2. The potential advantages and technical challenges in each of the methods are listed in table 1.2.

RED+GREEN+BLUE LEDs   UVLED + RGB Phosphors   BLUE LED + Yellow Phosphor
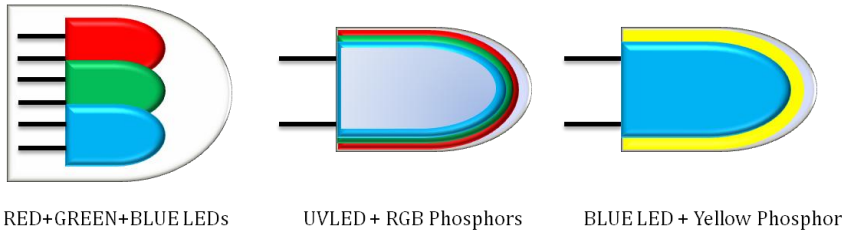
Figure 1.2 Different approaches to generate white light.

Table 1.2 Advantages and disadvantages of various white light generation approaches.

Method	Advantages	Disadvantages
RBG LEDs	• No quantum deficit • White point control • Excellent CRI	• No control on CCT • Needs independent output power control • Variable lifetimes of each LEDs
Blue LED & Yellow phosphor	• Small, light weight • Easy to operate • Long lifetime	• Less efficient • Poor color rendering
UV LED & RBG phosphors	• Cheaper than RGB-LED matrix • Gives good white color • Excellent color rendering	• Less efficient due to stokes conversion • Difficult to control the uniformity of the phosphor coating • Phosphor aging faster than LED

Currently, commercially available white LEDs consist of a blue InGaN LED coated with YAG : Ce inorganic phosphor. The InGaN LED generates blue light at a peak wavelength of about 460 nm, which excites the YAG : Ce^{3+} phosphor to emit yellow light. This design fails to give uniform white light as the escaped blue light is observed at the edges of the diode. And more importantly, the CRI value is still low. Nowadays the second method of using UV LEDs and three different phosphors is gaining more attention. Both blue and near UV LEDs are based on solid solutions of InN and GaN. As the InN content increases, the external quantum efficiency of the LED chip increases accompanied by a red-shift of the emitted radiation [21]. At wavelengths longer than 450 nm, the external quantum efficiency decreases rapidly toward the green part of the spectrum, a phenomenon referred to as the green gap in the SSL technology. Near UV LEDs also finds advantages in less current drooping and significantly less binning [19]. The improved efficiency allows the near UV LEDs to produce a greater photon density at higher currents than the blue LEDs helping to compensate for the increased Stokes loss.

1.5 Phenomenon of luminescence

Luminescence is light that usually occurs at low temperatures and is thus a form of cold body radiation [22, 23]. This cold body radiation can be caused by various types of energy sources such as chemical reactions, electrical energy, subatomic motions, stress on crystal and so on except high temperature. Photoluminescence is the process in which the compound absorbs photons or electromagnetic radiation, and the electrons gets excited to a higher electron energy state and then radiates the photons back out, returning to a lower energy state. In most cases (a complex or a metal center in a crystal)

the electronic excitation turns to vibrational energy resulting in the non-radiative transition (heat). Depending on the lifetime and the process of the radiation transition, luminescence can be classified to fluorescence and phosphorescence. The fluorescence has no change of electron spin and is caused by singlet to singlet or triplet to triplet transition ($S_N \rightarrow S_{N-1 \text{ or } 0}$, $T_N \rightarrow T_{N-1}$; N ≥2) with the lifetime ~ 10^{-9} - 10^{-5} seconds. Phosphorescence has emission involving spin changes transition ($S_N \rightarrow T_{N-1}$, $T_N \rightarrow S_{N \text{ or } 0}$; N ≥2) having longer lifetime >10^{-5} seconds. The electronic states of a molecule and the transitions between them is illustrated in the Jablonski diagram given in figure 1.3. The states are arranged vertically by energy and grouped horizontally by spin multiplicity. The straight arrows indicates radiative transitions and squiggly arrows represents non-radiative transitions.
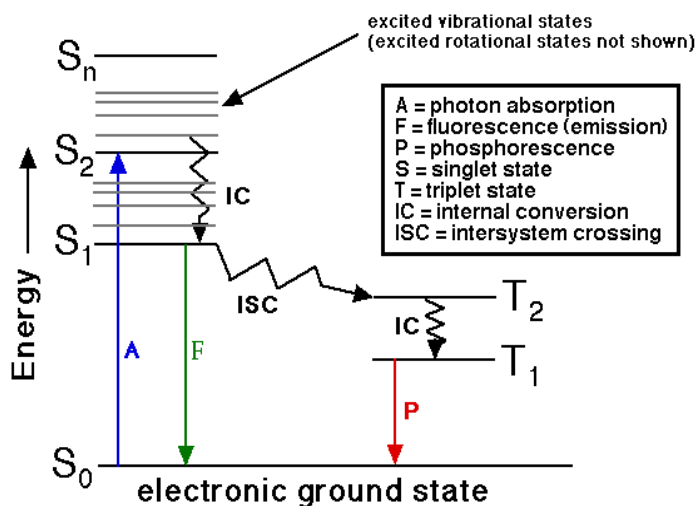
Figure 1.3 Jablonski diagram illustrating electronic states of a molecule and the transitions.

1.6 Phosphors: A basic understanding

Phosphors are materials capable of emitting light when subjected to UV radiation, X-rays, electron bombardment, friction or some other form of excitation [24]. A typical phosphor material and the physical processes involved in the phenomenon of characteristic luminescence are presented schematically in figure 1.4.
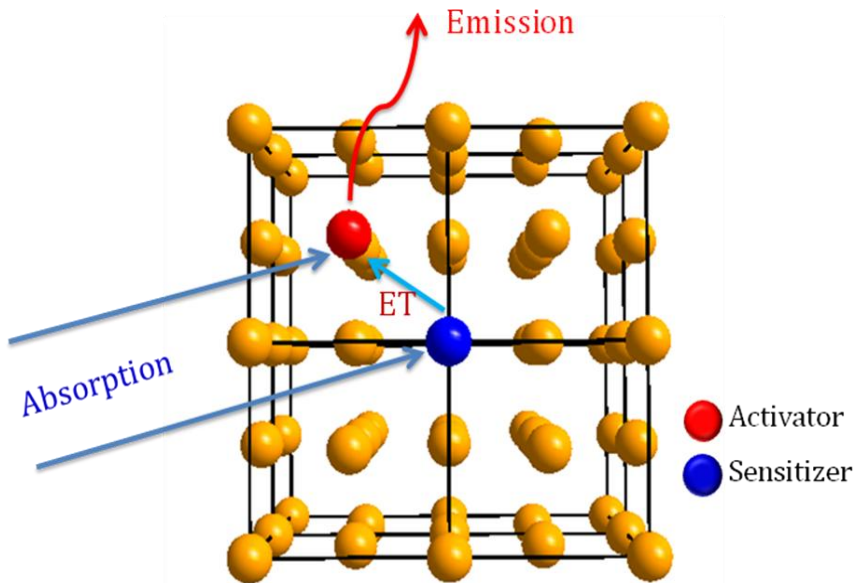
Figure 1.4 Schematic representation of a typical phosphor material.

Phosphors are usually made from a suitable host material, to which an activator is added. Activators are the luminescent centers in the host lattice. At these sites the electron relaxes radiatively. They can prolong the emission time. For a given host lattice, each activator can give a characteristic spectrum. Rare earth elements play an important role in both sides. Commonly used activators are Eu^{3+}, Eu^{2+}, Ce^{3+}, Dy^{3+}, Er^{3+}, Pr^{3+} etc. If the activator does not absorb the excitation radiation effectively, it is possible to excite the activator indirectly by energy transfer (ET) method. In such cases, sensitizers performs this role.

Sensitizers are ions or ionic groups incorporated into the host lattice. The underlying processes taking place during phosphorescence within a phosphor include incident light absorption, energy transfers between the various dopants present in the host, radiative relaxation of the excited ions *via* photon emission, and non-radiative relaxation processes *via* phonon emission or transfer of energy [25]. The luminescence of phosphors is determined by the local environment that surrounds the activator ions. Luminescence properties of phosphors are sensitive to this crystal field. Lanthanide ions can exhibit three types of excitation transitions: 4f - 4f transitions, 4f - 5d transitions, and charge - transfer state transitions [26].

4f - 4f transitions

4f - 4f transitions are very important in most of the practical phosphors containing rare earth activator ions and they involve movements of electrons between the different energy levels of the 4f orbitals of the same lanthanide ion. 4f - 4f electric - dipole transitions are in theory forbidden by the parity rule. However, in practice they are generally observed, but the corresponding emission bands are usually narrow.

4f - 5d transitions

In 4f - 5d transitions, one of the 4f electrons is excited to a 5d orbital of higher energy. This type of excitation absorption is usually denoted as $4f^n$ - $4f^{n-1}5d$ and is typically observed in Ce^{3+} ions ($4f^1$ configuration). Since empty, half filled or completely filled electron shell configurations are the most stable ones, the excess 4f electron of Ce^{3+} is easily transferred to the 5d orbital. Unlike 4f - 4f transitions, 4f - 5d transitions are allowed, which results in strong and broad absorption cross-sections.

Charge - transfer state (CTS) transitions

The last possible excitation mechanism is the charge-transfer state (CTS) transition, in which 2p electrons from the neighboring anions (e.g. O^{2-} in oxides) are transferred to a 4f orbital. This is typically observed in Eu^{3+} ($4f^6$) which needs an additional electron to reach the half filled configuration. These transitions are allowed and result in broad and intense absorptions.

1.7 Applications of various phosphor materials

Phosphors are technologically brilliant as they cover a broad range of applications. Many of the materials developed in the earlier stages of phosphor research were used in emissive display devices like color projection televisions [27-31], amplifiers in optical communication [32, 33] cathode ray tubes (CRTs), fluorescent tubes, and lasers [34 - 37]. In addition, phosphors also find applications in X-ray detector systems [38 - 48] and scintillators [49 - 57]. Phosphor research was extended to the areas such as solar cells [58 - 61] and white light emitting LEDs over the last two decades. Now these phosphor materials are gearing up towards its application as general illumination sources as solid state lighting devices to replace all existing sources. As the focus of the work lies towards the synthesis and characterization of phosphors for pc-WLEDs a survey in that area is given in the next part.

1.8 Basic requirement of a phosphor to be used in pc-WLEDs

All the compounds that show luminescence under excitation cannot be used in white light application. There are several prerequisites that a phosphor should simultaneously possess when they are taken to application. Most important requirements are listed as follows:

1. The phosphor must have a high absorption rate in the LED emission range and the excitation maximum should fall in the range of the pumping LED.

2. The emissions of the developed phosphor in combination with the emissions from other phosphor must lead to the generation of pure white light with good CRI and CCT.

3. The quantum efficiency (QE) of the phosphors should be as high as possible maximizing the electrical to optical conversion efficiency of the LED package.

4. The phosphor layers are expected to operate at elevated temperatures. Therefore, they should have reduced thermal quenching.

5. The phosphor must possess chemical and thermal stability and should be free from photo-bleaching.

6. In the economic aspect, synthesis route should be easy so as to manufacture the phosphor on a large scale.

7. The phosphor should be non-toxic, and the fabrication, use, and disposal of the phosphor should be as environmentally benign as possible.

1.9 Literature on various phosphors developed

Extensive research in the field of developing novel and stable phosphors for pc-WLEDs was carried out by many research groups. A complete listing is practically difficult as a large number of phosphors have been developed with this aim. In this section, major phosphor families that contributed to the SSL development are discussed briefly. Some of the phosphor materials whose emission wavelengths are falling under red, green and blue regions upon blue or/and UV excitations are listed in table 1.3.

Table 1.3 Some of red, green and blue phosphors for solid state lighting applications.

	Composition	Excitation Peak (nm)	Emission Peak (nm)	Ref.
RED	$M_2Si_5N_8(M = Eu, Ba, Sr, Ca) : Eu^{2+}$	465	570 - 680 609 - 680 515 - 606	62, 63
	$CaAlSiN_3 : Eu^{2+}$	460	634 649	64, 65
	$Lu_2CaMg_2(Si,Ge)_3O_{12} : Ce^{3+}$	470	605	66
	$Ln_2MoO_6, AMO_4,(A = Ca, Sr; M = Mo, W): Eu^{3+}$	394, 465	615	67 - 71
	$K_2SiF_6: Mn^{4+}$	460	646	72, 73
	$Mg_3Y_2Ge_3O_{12} : Ce^{3+}$	460	604	74
	$Y_2O_3, Y_2O_2S : Eu^{3+}$	395	612	75 - 78
	$(Sr, Ca)AlSiN_3 : Eu^{2+}$	455	650	79
GREEN	$SrGa_2S_4 : Eu^{2+}$ $BaGa_2S_4 : Eu^{2+}$	405 460	503 540	80, 81
	$Sr_{2-x}BaSiO_4 : Eu$	400	510 - 570	82
	$MSi_2O_2N_2 : Eu^{2+}$ (M = Sr, Ca, Ba)	400	538 - 564	83
	β -SIALON : Eu	275	416,525	84
	$Ba_3Si_6O_{12}N_2 : Eu$	450	529	85
	$CaSc_2O_4 : Ce$	437, 460	515	86
	$(Ba,Sr)MgAl_{10}O_{17} : Mn, Eu$	340	487	87
	$Ca_8Zn(SiO_4)_4Cl_2 : Eu^{2+}$	365, 405	510	88
	$Sr_4La_2Ca_4(PO_4)O_2 : Ce^{3+}$	352	506	89
BLUE	$Sr-Al-O : Eu^{2+}$	365	456	90
	$LiSrPO_4 : Eu^{2+}$	396	450	91
	$CaLaGa_3S_6O : Ce^{3+}$	398	478	92
	$(Sr,Ba)_3MgSi_2O_8 : Eu$	147	435, 460	93
	$LaOX (X = Cl, Br, I)$	300	425, 427, 435	94
	$KSrBP_2O_8$	365	462	95

1.10   Why more research on red phosphors?

As already discussed in the section of various approaches towards white light generation; two methods to generate white light using (i) a blue LED and yellow phosphor and (ii) a UV LED and tricolor phosphors are mostly adopted. Commercial pc-WLEDs generally use a 450 – 470 nm blue GaN LED chip covered by a yellowish phosphor coating, which is usually made of YAG : Ce^{3+}. They suffer from some weaknesses, such as poor color rendering index and low stability of color temperature. The color rendering index of white LEDs made by blue LED with yellow emitting phosphor method is low due to lack of red light component. So for developing white light one should combine a UV chip with tricolor (red, green and blue) phosphors or compensate the red light deficiency of YAG : Ce^{3+} based LED with a separate red emitting phosphor[96]. Currently in near UV LEDs method, Y_2O_2S : Eu^{3+} for red, ZnS : Cu^{2+}, Al^{3+} for green and $BaMgAl_{10}O_{17}$: Eu^{2+} for blue are used [97, 98]. The current red phosphor cannot absorb light efficiently in the UV region and its brightness is about eight times less than that of the available green and blue phosphors. This sulfide based red phosphors lacks chemical stability and is highly harmful to the environment. Other major red phosphors in today's market also fall in the sulfide family. Thus novel red phosphor materials that could be effectively excited in the near UV and visible region with good absorption and emission properties, good thermal and chemical stability, minimal thermal quenching, high quantum yield and preferably with low cost should be developed to meet the requirements.

1.11 Eu^{3+} activated phosphor

An appreciable amount of research has been performed for the synthesis and the development of different red phosphors in various

hosts and activator ions. Literature shows that various broad band emitting Mn^{2+}, Eu^{2+} activated red phosphors were developed. However, broad emission leads to a spillover into the deep red where the human eye is insensitive, and a decrease in spectral efficiency [67]. Therefore, narrow emitters are in demand. Rare earth ions (RE^{3+}) particularly Eu^{3+}, Sm^{3+}, Pr^{3+} and Dy^{3+} are suitable as activators, due to their well defined transitions within the 4f shell. They exhibit narrow emission lines due to internal f - f transitions and are widely used as the activators for red emission. Eu^{3+} ions are considered to be the preferable choice of activators for red luminescence as they exhibit a high lumen equivalent, quantum efficiency, and photostability [21, 99]. In the periodic table, Eu^{3+} lies among the lanthanides, 6 electrons past Xe, which ends period 5 leaving the 5d and the 4f subshells empty, therefore [Xe]4f electronic configuration. They form a number of discrete energy levels owing to the presence of these deep lying 4f shell which is not entirely filled. Luminescence originating from electronic transitions between 4f levels is predominantly due to magnetic dipole or electric dipole interactions that offer the possibility of efficient emissions. Electric dipole f – f transitions are parity forbidden; the intensity of these transitions depends strongly on the site symmetry in a host crystal. Magnetic dipole transitions are not affected much by the site symmetry because they are parity allowed. Red luminescence of trivalent europium (Eu^{3+}) ions due to intraconfigurational f - f transitions is of technological importance because it has been widely applied to phosphors for color displays and fluorescent lamps. It is known that emission wavelengths of Eu^{3+} are determined primarily by their local environment in host crystals. When the Eu^{3+} ions are embedded in a site with inversion symmetry, the $^5D_0 \rightarrow$ $^7F_1$ magnetic dipole transition ($\sim$ 592 nm) is dominating, while in a site without inversion symmetry the $^5D_0 \rightarrow {}^7F_2$ electric dipole transition

(with emission wavelengths $\sim$ 610 - 620 nm) is the strongest [26]. Actually, both the electric-dipole and the magnetic-dipole transitions appear simultaneously in practical inorganic luminescent materials, although their intensities are different and, in most cases, one of which is much stronger. Therefore the fluorescence intensity ratio of $^5D_0 \rightarrow {}^7F_2$ to $^5D_0 \rightarrow {}^7F_1$; called as asymmetry ratio (which is always far from unity) gives a measure of the degree of distortion from inversion symmetry of the local environment around the Eu^{3+} ions in the host matrix [100]. Energy level diagram of Eu^{3+} ion is given in figure 1.5.
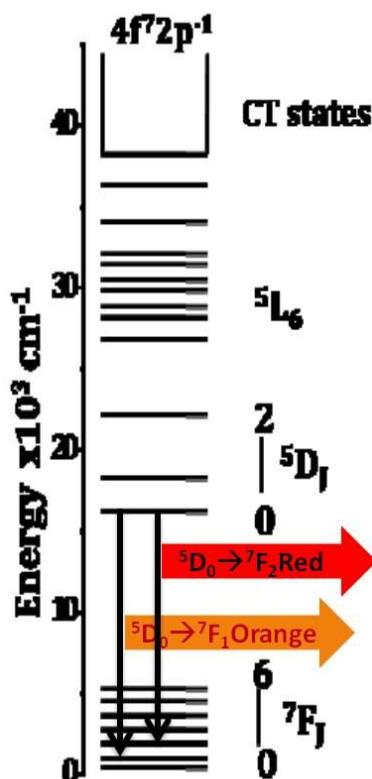
Figure 1.5 Energy level diagram of Eu^{3+} ion.

Interesting properties of Eu^{3+} in brief:

- ✓ *Emission wavelengths of Eu^{3+} strongly depend on local structures, coordination numbers, ordering and degree of distortion.*
- ✓ *Magnetic dipole f – f transitions are parity allowed.*
- ✓ *Electric dipole f – f transitions are parity forbidden*
- ✓ *When Eu^{3+} ion occupies a site with inversion symmetry, ($\Delta J = \pm 1$) the $^5D_0 \rightarrow {}^7F_1$ MD transition (orange) is dominating.*
- ✓ *When Eu^{3+} ion occupy a site without inversion symmetry, ($\Delta J = \pm 2$, 4, 6) the $^5D_0 \rightarrow {}^7F_2$ ED transition (red) is the strongest.*
- ✓ *Asymmetric ratio (red to orange ratio) provides a degree of local distortion and the nature of the doping sites.*
- ✓ *Split in the $^5D_0 \rightarrow {}^7F_0$ transition asses the site occupancy of Eu^{3+}.*

Eu³⁺ ions has a lot of technological applications and therefore its luminescence in numerous host lattices like various phosphates, silicates, halides, nitrides, oxynitrides, borates, fluorides, oxyfluorides etc are well studied. Each of these host matrices have its own merits and demerits. As already mentioned most of the well known red emitting phosphors for white LEDs are usually sulfide semiconductors such as $Zn_{1-x}Cd_xS$: Ag [101, 102], SrY_2S_4 : Eu [103, 104], CaS : Eu [105, 106], SrS : Eu, $Ca_{1-x}Sr_xS$: Eu [107], Ba_2ZnS_3 : Mn [108], etc. Another class of potential host for Eu^{3+} luminescence are molybdates or tungstates due to the intense charge transfer band absorption in UV region, effective f – f transition of Eu^{3+} at 394 nm and 465 nm and excellent thermal and hydrolytic stability, [109 - 111]. Alkaline earth borate is an important luminescent material because of its excellent chemistry and thermal stabilization, facile synthesis and cheap raw material (H_3BO_3), so it has been extensively applied to phosphor for lamps [112]. Silicate based phosphor materials have also been explored as silicate material has

good thermal and chemical stability although it is difficult to form phase pure compositions [113]. Doped rare earth tellurides (Ln_2TeO_6) are also suitable for use as inorganic phosphors. The La_2TeO_6 phosphors doped with Eu^{3+} have been synthesized and its photoluminescent properties were investigated [114]. Even the complex fluorides and oxyfluorides were studied as possible host matrices and a high quantum efficiency was observed [115, 116]. Rare earth tantalates and niobates like $LnMO_4$ (Ln = La, Gd, Y; M = Nb, Ta) also proved be to better host lattice for Eu^{3+} luminescence and has drawn the research interest significantly [117-121]. Different groups tried to enhance the photoluminescence properties of Eu^{3+} in various host by various approaches like co-doping, use of various fluxes, use of different synthesis procedures and processing temperatures etc. Bi^{3+} and Sm^{3+} were found to be excellent co-dopant and helped in improving luminescence characteristics [121 - 126].

1.12   Importance of Ln_3MO_7 structures

Various performance parameters of a phosphor material depends on the selection of a suitable host lattice. Red luminescence from the Eu^{3+} ions occurs when these activator ions are suitably incorporated into the host lattice. As already discussed, the probability of electronic transitions from the lowest $^5D_0$ excited state to the $^7F_{0-6}$ ground states differs depending on site symmetries. Thus the crystal structure of the host lattice, symmetry and coordination of the doping site, ordering of the host lattice etc. should be studied in detail. Activator doping concentration, uniformity in the activator distribution and various other factors also depend on the host lattice. Ln_3MO_7 forms a right choice of host family for studying the photoluminescence properties of Eu^{3+} as

this class of closely related compounds could form diverse structures with different site symmetries.

Ln_3MO_7 structure can be classified as a class of typical weberite structure ($A_2B_2X_7$; A and B are cations and X an anion, O or F) with three lanthanoid cations, one transiton metal cation and oxygen anions. Various compounds possess similar stoichiometry but fall under different crystal structures due to the difference in the cations and anions occupied. However, all these compounds of this stoichiometry could be explained as a superstructure of fluorite (AO_2 or A_4O_8) structure. Crystal structure of these compounds varies from defect fluorite or pyrochlore type cubic to weberite type orthorhombic with increasing ionic radius of the Ln^{3+} ion [127 - 130]. The relationships between these structures are given in figure 1.6. Weberite structure also shows a wide variety of modifications including monoclinic and trigonal structures.

Bixbyite:
$A_3{}^{3+}B^{3+}O_6\square_2$, *Ia-3*
A (24*d*)   x 0 ¼
B (8*b*)   ¼ ¼ ¼
O (48*e*)   x y z
$\square$ (16*c*)   x x x
$a = 2a_F$

Fluorite:
A_4O_8, *Fm-3m*
A (4*a*) 0 0 0
O (8*c*) ½ ½ ½

Pyrochlore:
$A_2{}^{3+}B_2{}^{4+}O_6O\square$, *Fd-3m*
A (16*d*)   ½ ½ ½
B (16*c*)   0 0 0
O (48*f*)   x ⅛ ⅛
O' (8*b*)   ⅜ ⅜ ⅜
$\square$ (8*a*)   ⅛ ⅛ ⅛
$a = 2a_F$

Weberite:
$A^{3+}A'^{3+}{}_2B^{5+}OO'_4O''_2\square$,
Cmcm or *C222₁*
A (4*b*)   0 ½ 0
A' (8*g*)   x y ½
B (4*a*)   0 0 0
O (4*c*)   ½ y ¼
O' (16*h*)   x y z
O'' (8*g*)   x y ¼
$\square$ (4*c*)   0 y ¼
$a \sim 2a_F, b \sim \sqrt{2}a_F, c \sim \sqrt{2}a_F$
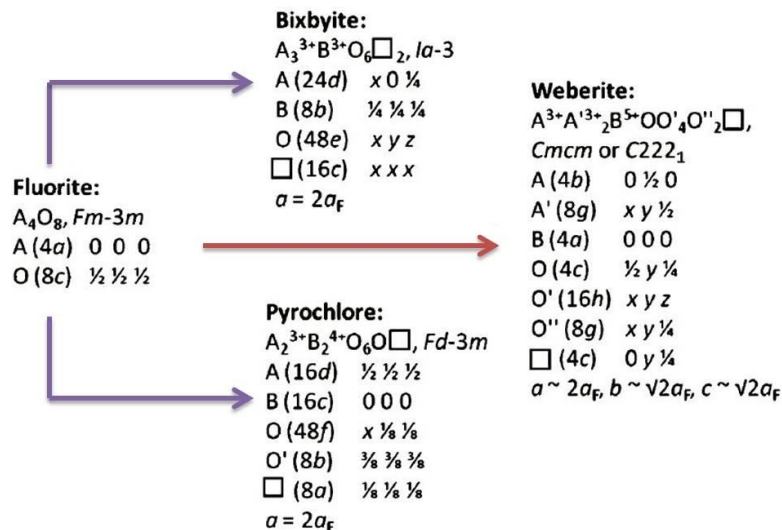
Figure 1.6 Wyckoff coordinates of fluorite and some superstructures [130].

In a basic fluorite structure, all the cations are equally coordinated to anions forming regular AO_8 cubes [131]. The preferential coordination and the number of anions are dependent on the size and the valency of the cation with respect to the anionic radius. In Ln_3MO_7, four tetravalent metal ions in the A site are replaced by three trivalent (Ln) and one pentavalent (M) ions forming one oxide vacancy per fluorite cell [132]. This reduction in the number of anions from eight to seven leads to a decrease in the coordination number of B cations (VI coordination) with respect to the A cations (VIII coordination) and introduces a variation in the cation coordination to keep the compound neutral. However, the compounds with smaller Ln cation (ionic radius within the tolerance limit) could occupy to form a stable and anion deficient defect fluorite structures. Typical fluorite and a defect fluorite unit cells are given in figure 1.7.
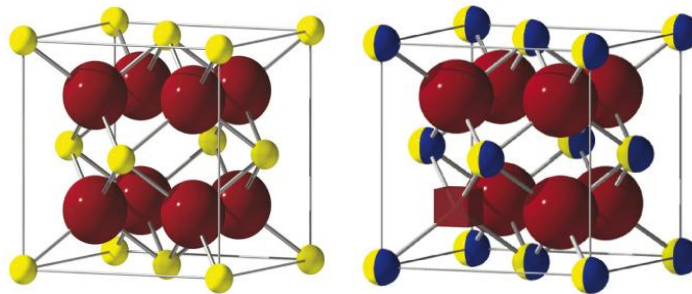
Figure 1.7 Typical fluorite and defect fluorite crystal structure.

Pyrochlore structure (*Fd-3m*) can be considered as an ordered, defective fluorite solid solution derived by ordering the cation sublattice and creating ordered oxygen vacancies in such a way that coordination of A atoms remains cubic, as in fluorite, but coordination of B cations

decreases to octahedral thereby doubling the unit cell with respect to the fluorite. In cubic pyrochlore, about $1/8$th of the oxygen (anion) atoms are orderly replaced [128]. A comparison of the unit cells of fluorite and pyrochlore is given in figure 1.8. C-type or bixbyite structures is another modification of fluorite formed by removing $1/4$th of the oxygen atoms in an orderly manner.
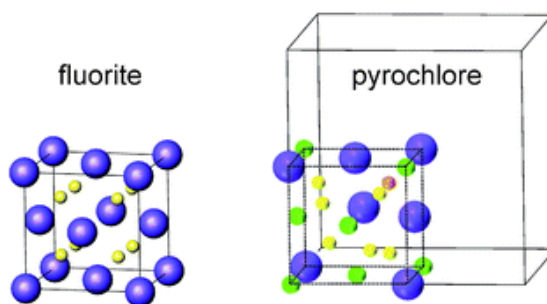
Figure 1.8 Comparison of a fluorite and pyrochlore unit cell.

Crystallographic aspects of orthorhombic class of Ln_3MO_7 compounds are extensively studied [131, 133 - 141]. The M^{5+} ion is coordinated with six oxygen ions, forming an MO_6 octahedron. These octahedra share corners forming one dimensional chains which are oriented along the c-axis. One third of the La cations are 8 - coordinated and lie in (001) rows which alternate with parallel rows of corner-linked MO, coordination octahedra within slabs parallel to (100). The remaining Ln cations lie in between these slabs in seven - fold coordination. Ln_3MO_7 orthorhombic crystal can possess a variety of space groups like Pnma, Cmcm, $C222_1$, Ccmm, $P2_12_12_1$ etc. with difference in the symmetry elements [130 - 132]. Crystal structure of a typical weberite is given in figure 1.9. Fluorite and weberite lattices are

compared in figure 1.10. Polymorphic modifications in these crystallographic structures are produced as the processing conditions changes.
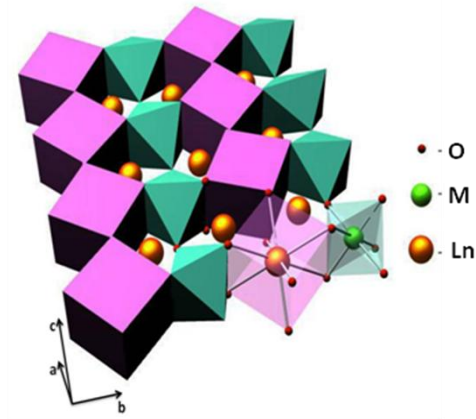
Figure 1.9 Representation of a typical weberite structure.
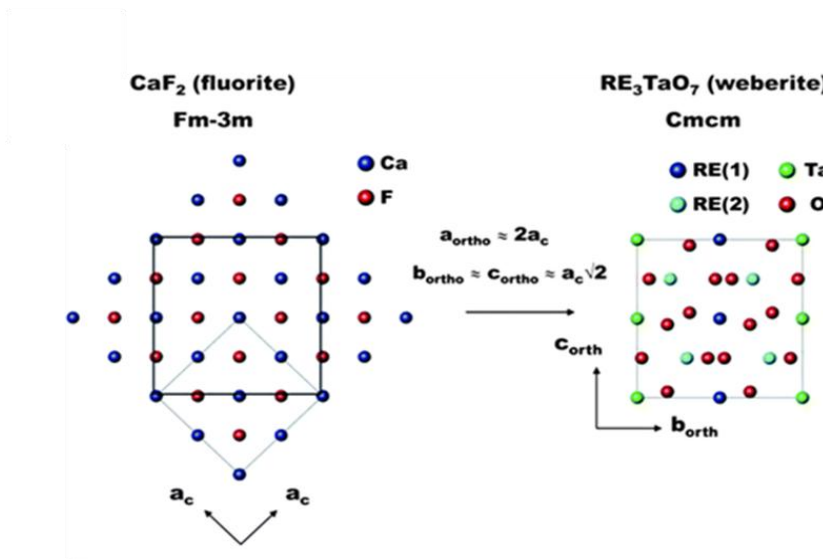
Figure 1.10 Comparison of a fluorite and a weberite structure [130].

1.13   Earlier works on Ln$_3$MO$_7$ structures

Compounds with anion deficient fluorite related structure exhibit various interesting properties including conductivity, dielectric properties, ferroelectric properties, magnetic properties as well as photocatalytic activity due to the large structural flexibility and diverse nature of the phase formation. Crystallographic investigations on Ln$_3$MO$_7$ can be found dating as far back as 1964. The parent structure of this family of compounds, La$_3$NbO$_7$ was first determined by Rossell [129]. His studies revealed the structure as an orthorhombic superstructure of cubic fluorite type with space group Cmcm bearing three distinct cation sites (one distorted cubic Ln^{3+}, one distorted pentagonal bipyramidal Ln^{3+} site and one octahedral M^{5+} site). Further the investigations on Ln$_3$MO$_7$ compounds were focused on the crystallographic aspects due to their confusing nature and the close relationship with fluorite and pyrochlore type structures. Owing to a number of polymorphic modifications under different conditions this class of compounds possess structural transitions between various space groups. This type of studies on the structural transitions were extensively done [130 - 132]. As a direct consequence of a large number of chemical combinations between the lanthanoid ion Ln^{3+} and metal element M, a great deal of discrepancies is associated with these structures. As various magnetic, dielectric, photocatalytic properties have a close association with the crystal structure, the determination of right space groups are essential.

Among the wide range of electronic properties occurring in these compounds due to the presence of both 4f and 4d or 5d metals, their magnetic properties are investigated broadly [142 - 145]. Detailed reports on the magnetic and thermal properties of ruthenium - iridium - and osmium containing compounds gave evidence for the existence of

low temperature structural phase transitions [146]. *Greedan et al.* studied the electronic and thermal properties of La_3MoO_7 by magnetic susceptibility, electric resistivity and neutron diffraction measurements [147].

The series of Ln_3MO_7 compounds provides an interesting stage to study the structure - dielectric property relationships since the lanthanides show a nearly linear relationship between the ionic radius and polarizability. Dielectric properties of Ln_3NbO_7 (Ln = Nd, Gd, Dy, Er, Yb and Y) over a broad range of frequencies and temperature was studied and reported by *Cai et al.* [148]. Various literature on dielectric relaxation and other dielectric properties of many more compounds of Ln_3MO_7 and even its expanded family $Ln_2(MM')_2O_7$ are available [149, 150].

Literature shows that these highly versatile compounds could even function as a photocatalyst for splitting water and as a possible electrolyte for solid oxide fuel cell [151, 152]. There are some recent reports on the photoluminescence properties of this class of compounds. *Yanyan et al.* reported the Eu^{3+} luminescence of hydrothermally synthesized Lu_3TaO_7, Lu_3NbO_7 and Y_3TaO_7 nanophosphors which could be used as a red phosphor component for WLEDs upon further improvement [153]. The group tried to enhance the luminescent properties by coating the Lu_3TaO_7 shell on the surface of the Lu_3TaO_7 : Eu^{3+} core, thereby increasing the distance of the luminescent Eu^{3+} and reducing the non-radiative pathways [154]. Structural and luminescent properties of ternary rare earth antimonates R_3SbO_7 was recently reported by *Wang et al.* [155]. The growing interest towards these type of host matrices clearly indicates the potential of Ln_3MO_7 structures as a possible host matrix with improved photoluminescence properties.

1.14   Objectives of the present work

From the literature review, the overwhelming need for an intense, stable and efficient red phosphor material is clear. The phosphor research group is still keen on understanding the factors deciding the luminescence performance of various host and activator materials. The primary aim of this research work is to develop novel and potential red phosphor candidates to be used in pc-WLEDs. Our objective also include correlating various aspects like structure, morphology and photoluminescence properties of developed phosphors. Through this research work, a proper understanding of different influencing parameters that could be adopted to other host families is also expected. Focus will be given to the methods for improving the Eu^{3+} luminescence in Ln_3MO_7 host structures through compositional and structural variation and thereafter optimizing the activator doping concentration.

2

SYNTHESIS & CHARACTERIZATION METHODS
_____

The developments in material science need adequate knowledge on the synthesis methodologies along with the simultaneous characterization of developed materials by employing different characterization tools. The first part of this chapter describes the synthesis method adopted in the present studies. The powder phosphor samples are structurally, morphologically and optically characterized using various analytical tools namely X-ray diffraction, scanning electron microscopy, energy dispersive spectroscopy, X-ray dot mapping, Raman spectroscopy, Absorption spectroscopy, Luminescence spectroscopy etc. A background of the working principles and experimental setup used in the study are also explained in this chapter.

2.1 Introduction

A lot of experimental procedures including the synthesis and characterization of compounds are required for the development of phosphor materials along with a basic understanding of the theoretical aspects. There are many preparation methods and choosing the most suitable synthesis route for developing new and promising compounds is important. Characterization techniques are very essential for understanding the complete picture of the crystal phase, particle distribution, morphology and various other properties of the prepared samples.

2.2 Synthesis of phosphor materials

Synthesis routes play a crucial role in preparing the target product and determining its properties. Solid state reaction is the most commonly adopted synthesis route for producing multi component oxides. In the literature, many phosphors are synthesized by solid state reactions between starting materials, at high temperature, in an air or a reducing atmosphere. High purity solid reactants are usually ground together, sometimes pelletized, and placed in a crucible. They then undergo several sintering stages, usually with intermediate grinding. Fluxes are sometimes added to the raw material mixture to help crystal growth, to accelerate it, or to lower the activation energy. Solid state reactions present a number of advantages over liquid routes, including the ease to carry them out, the large availability of the starting materials, and the possibility of preparing compounds in large amount. In the works presented in this thesis, high temperature solid state reaction route is mainly employed. The stepwise procedures involved in the synthesis [156, 157] are as given below and is schematically illustrated in figure 2.1.

2.2.1 Stoichiometric weighing of raw materials.

The raw materials are selected depending on the composition, purity, particle size, distribution and reactivity. On the basis of chemical composition, stoichiometric quantities of each component is calculated and weighed. Heating the chemicals before weighing helps evaporating any moisture absorbed by the chemicals. In the present thesis, mostly high purity (99.99%) oxides and carbonates are used as starting materials.

2.2.2 Mixing and drying

Stoichiometrically weighed chemicals are mixed in an acetone medium using an agate mortar and pestle, and the resulting powder is dried in hot air oven (~100°C for 30 mint). This process is repeated three times to acquire a homogeneous and fine powder. Homogeneity of the samples is extremely important in the phase formation of the samples reducing porosity and agglomeration.

2.2.3 Pelletization

The homogeneously mixed powders are made into pellets using a pelletizer so as to enhance intimate contact of reactants and to minimize contact with the crucible.

2.2.4 Calcination

Calcination is a process of heating the samples at a temperature well below the melting point in a supply of air. The compound formation occurs during this step and the heat treatment is given to promote sufficient interaction between the constituents. During calcination, the volatile impurities are removed. Alumina or platinum plates with high melting points are usually used to place the samples. Calcination is used

for achieving the optimum particle size and desired crystal phase. One of the important uses of calcination is coarsening, that is, increasing the particle size of a very fine powder with improved packing properties. Solid phase chemical reactions are carried out during this operation and the calcinations are repeated until the final compounds are formed. The calcined pellets are finely ground to fine powders so as to obtain the final products.
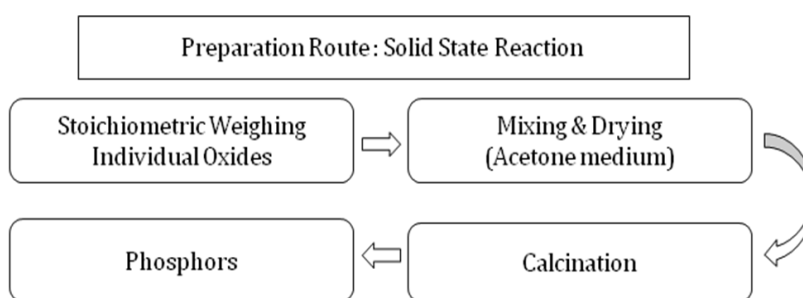
Figure 2.1 Schematic illustration of phosphor preparation by solid state reaction route.

2.3 Characterization of the samples

Proper knowledge on the working principles and operation of various characterization tools along with the capability in analyzing the obtained results forms the most important part in materials research. In the present study, structural and morphological studies were carried out using powder X-ray diffraction (XRD) and scanning electron microscopy (SEM) respectively. Raman analysis of the samples helped in understanding more about the structure in association with its optical properties. Absorbance and photoluminescent properties of the prepared powders were well studied using UV-visible absorbance and luminescence spectroscopy respectively. Various techniques used in the study are schematically represented in figure 2.2.
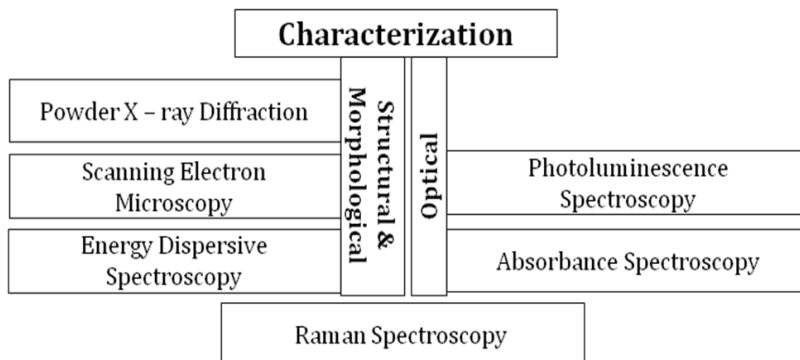
Figure 2.2 Schematic illustration of various characterization techniques used.

2.3.1 Powder X-ray diffraction and Rietveld analysis

2.3.1.1 Basic understanding

X-ray diffraction techniques reveal information about the crystal structure, chemical composition, and other physical properties of materials. These techniques are based on observing the scattered intensity of an X-ray beam hitting a sample as a function of incident and scattered angle. X-ray diffraction is based on constructive interference of monochromatic X-rays and a crystalline sample. The positions of the diffraction peaks are determined by the spacing of the crystallographic planes and follow Bragg's law;

$$(n\lambda = 2d \sin \theta) \qquad\qquad 2.1$$

where n is an integer, λ wavelength of the X-ray source, d spacing of the crystal planes and θ the glancing angle. The XRD pattern of each crystalline material is unique. Typically, the identification of the compounds is achieved by comparison of d - spacings with standard reference patterns [158]. X-ray diffractometers consist of three basic elements: an X-ray tube, a sample holder, and an X-ray detector which is illustrated in figure 2.3.
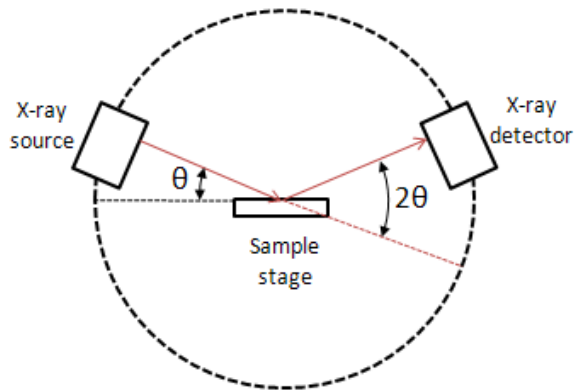
Figure 2.3 Schematic representation of a X-ray diffractometer.

X-rays are generated in a cathode ray tube by heating a filament to produce electrons, accelerating the electrons towards a target by applying a voltage, and bombarding the target material with electrons. When electrons have sufficient energy to dislodge inner shell electrons of the target material, characteristic X-ray spectra are produced. These spectra consist of several components, the most common being K_α and K_β. The specific wavelengths are characteristic of the target material (Cu, Fe, Mo, Cr). Filtering by foils or crystal monochromators, is required to produce monochromatic X-rays needed for diffraction. These X-rays are collimated and directed onto the sample. As the sample and detector are rotated, the intensity of the reflected X-rays is recorded. When the geometry of the incident X-rays impinging the sample satisfies the Bragg Equation, constructive interference occurs and a peak in intensity occurs. A detector records and processes this X-ray signal and converts the signal to a count rate which is then output to a device such as a printer or a computer monitor. Peak positions occur where the X-ray beam has been diffracted by the crystal lattice.

The unique set of d - spacings derived from this pattern can be used to fingerprint the material [158].

Refinement of the crystal structure can be carried out from the data obtained from spectra using Rietveld analysis. This method devised by Hugo Rietveld uses least squares approach to refine a theoretical line profile until it matches the measured profile [159]. A number of parameters like background, peak shape, lattice parameters can be refined using a Rietveld refinement software.

2.3.1.2 Experimental details

The X-ray powder diffraction patterns presented in this thesis were measured using a theta-theta diffractometer of X'Pert Pro PANalytical make with the goniometer radius of 240 mm. The diffractometer was equipped with a Ni filtered Cu - Kα source (λ = 1.5406 Å) and was operated at 40 kV and 30 mA. The diffraction peaks were recorded in the 2θ range from 10° to 90° at room temperature. Rietveld refinement of the samples was carried out using X'pert Plus software. Rietveld refinement process will adjust the refinable parameters until the residual is minimized and a best fit is obtained. Various factors like background, lattice parameters, caglioti parameters etc were refined.

2.3.2 Scanning electron microscopy, Energy dispersion spectroscopy and X-ray dot mapping

2.3.2.1 Basic understanding

The scanning electron microscope (SEM) is a type of electron microscope that images the sample surface by scanning it with a high energy beam of electrons in a raster scan pattern. A typical SEM

consists of an electron optical column, vacuum system, signal detectors and display system. A schematic representation is given in figure 2.4.
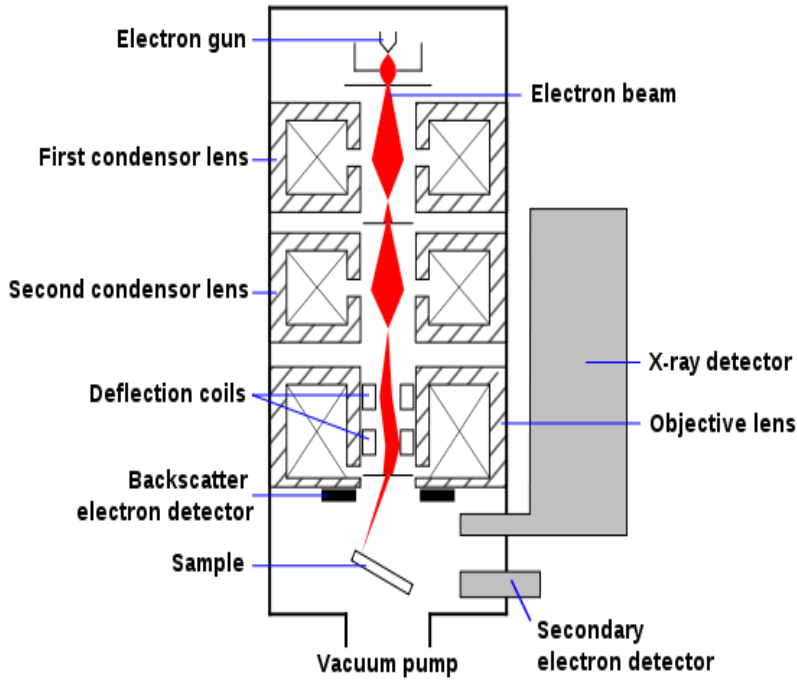
Figure 2.4 Schematic representation of a scanning electron microscope.

An electron beam is thermionically emitted from an electron gun fitted with a tungsten filament cathode. The electron beam is focused by one or two condenser lenses. The beam passes through pairs of scanning coils or pairs of deflector plates in the electron column which deflect the beam in the x and y - axes so that it scans in a raster fashion over a rectangular area of the sample surface. The energy exchange between the electron beam and the sample results in the reflection of high energy electrons by elastic scattering, emission of secondary electrons by inelastic scattering and the emission of

electromagnetic radiation, each of which can be detected by specialized detectors. The beam current absorbed by the specimen can also be detected and used to create images of the distribution of specimen current [160 - 162].

Energy dispersive X-ray spectroscopy (EDS) is an analytical technique used for the elemental analysis or chemical characterization of a sample. EDS system is primarily comprised of three components namely X-ray detector which detects and converts X-ray into electronic signals, a pulse processor which measures the electronic signals to determine the energy of each X-rays detected and a multiple channel analyzer which displays and interprets the X-ray data. EDS analysis quantifies the elements it detects by a standard or standardless analysis. A standardless analysis quantifies the elements by calculating the area under the peak of each identified element and after taking account for the accelerating voltage of the beam to produce the spectrum, performs calculations to create sensitivity factors that will convert the area under the peak into weight or atomic percent. The software then performs a Gaussian fit of the elemental peaks selected and calculates the area under the peaks. One of the most popular algorithms is ZAF where Z stands for the atomic number of the element, A and F are the absorbance and fluorescence values to compensate for the X-ray peak interaction. From this, the atomic and weight percent are calculated. Standards quantifications are performed in a similar fashion except that instead of performing ZAF calculations on the areas under the elemental peaks, the areas are compared to standards files which are spectra of the elements to be quantified acquired under the exact conditions of the unknown spectrum. Since it requires these additional spectra, this form of analysis is more time consuming and generally is not more accurate than a standardless quantification

unless the X-ray peaks of the elements to be quantified overlap or the elements are in trace quantities.

It is also possible to map the elements found in an SEM image by X-ray analysis. By setting windows around the peaks of specific elements, the software can scan the sample and create digital images or maps of each element. By placing dots on the screen when an X-ray count of the particular element is received, an image is formed that mimics the SEM image, except the contrast is formed by the elemental X-ray emission. X-ray mapping is the most convenient and popular method for producing compositional images.

2.3.2.2 Experimental details

Scanning electron micrographs of the prepared samples were recorded by JEOL, JSM - 5600LV SEM operated at 15kV. SEM images of some of the samples were recorded by Carl Zeiss EVO 18 instrument. In both cases, samples were prepared by sticking the powders on a carbon tape pasted on a specimen holder of about 10mm diameter. The samples were given a thin layer of gold or palladium coating so as to give them a conductive nature. EDS analysis and X-ray dot mapping of the samples was recorded using the instrumental set up attached to Carl Zeiss (EVO - 18 Edition) SEM.

2.3.3 Raman spectroscopy
2.3.3.1 Basic understanding

Raman spectroscopy is a spectroscopic technique used to study vibrational, rotational, and other low frequency modes in a system. It relies on inelastic scattering or Raman scattering of monochromatic light, usually from a laser in the visible, near infrared, or near ultraviolet range. The laser light interacts with molecular vibrations,

phonons or other excitations in the system, resulting in the energy of the laser photons being shifted up or down. The shift in energy gives information about the vibrational modes in the system.

Schematic representation of a typical Raman spectrometer is given in figure 2.5. The sample is illuminated with a laser beam. Light from the illuminated spot is collected with a lens and sent through a monochromator. Wavelengths close to the laser line due to elastic Rayleigh scattering are filtered out while the rest of the collected light is dispersed onto a detector. The Raman effect occurs when light impinges upon a molecule and interacts with the electron cloud and the bonds of that molecule. For the spontaneous Raman effect, which is a form of light scattering, a photon excites the molecule from the ground state to a virtual energy state. When the molecule relaxes it emits a photon and it returns to a different rotational or vibrational state. The difference in energy between the original state and this new state leads to a shift in the emitted photon's frequency away from the excitation wavelength. If the final vibrational state of the molecule is more energetic than the initial state, then the emitted photon will be shifted to a lower frequency in order to balance the total energy of the system. This shift in frequency is designated as a Stokes shift. If the final vibrational state is less energetic than the initial state, then the emitted photon will be shifted to a higher frequency, and this is designated as an Anti - Stokes shift. A change in the molecular polarization potential or amount of deformation of the electron cloud with respect to the vibrational coordinate is required for a molecule to exhibit a Raman effect. The amount of the polarizability change will determine the Raman scattering intensity. The pattern of shifted frequencies is determined by the rotational and vibrational states of the sample. This dependence on the polarizability differs from Infrared (IR)

spectroscopy where the interaction between the molecule and light is determined by the dipole moment. This contrasting feature allows to analyze transitions that might not be IR active *via* Raman spectroscopy, as exemplified by the rule of mutual exclusion in centrosymmetric molecules.
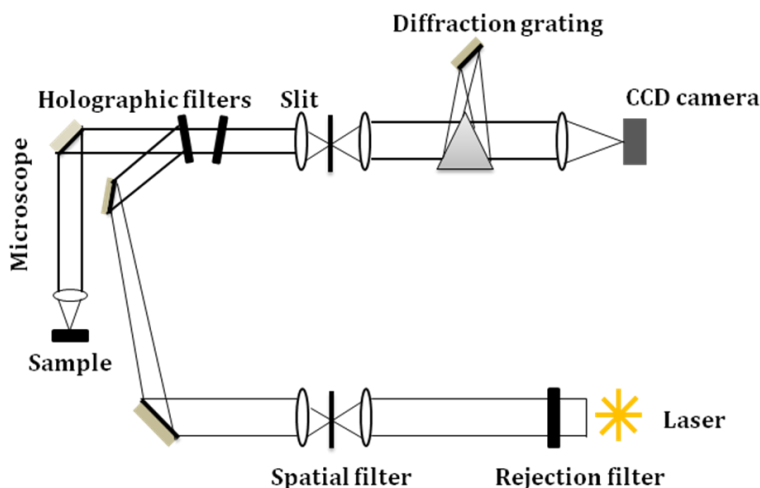
Figure 2.5 Schematic representation of a typical Raman spectrometer.

2.3.3.2 Experimental details

The FT-Raman spectra of powdered samples were recorded on a Labram HR 800 (Horiba Scientific, Instrument no L/4/794) spectrometer. An argon laser (784 nm) was used as the excitation source. Data was collected from 100 - 1000 cm^{-1} wavenumber range.

2.3.4 UV-visible absorption spectroscopy
2.3.4.1 Basic understanding

UV-visible absorption spectroscopy is a powerful analytical tool to understand the optical properties of materials which involves

absorption of UV/Visible light by a molecule causing the excitation of an electron from ground electronic state to excited electronic state. UV-visible absorption spectrum is a plot of degree of absorption of a sample against the wavelength of the incident radiation. It may include both broad and sharp lines of absorption. A typical spectrophotometer set up for UV-visible absorption is shown in figure 2.6.
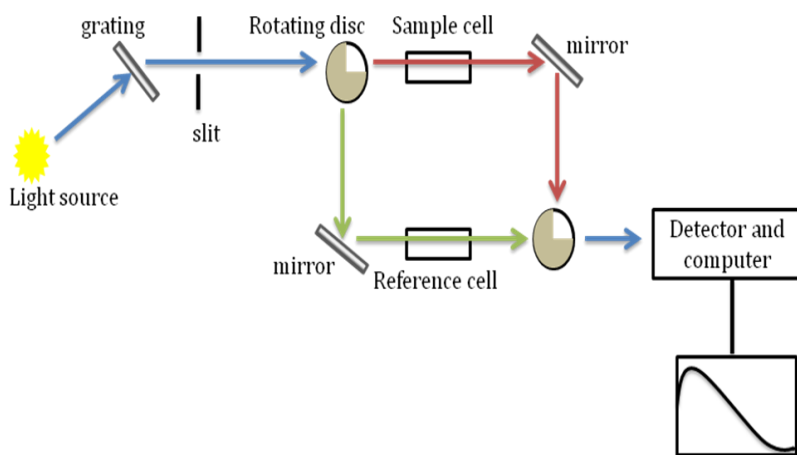
Figure 2.6 Schematic illustration of a UV-visible absorption spectrophotometer.

In absorption spectroscopy, the photon energy of the radiation incident on the sample is selected by a scanning monochromator. The radiation selected by the monochromator is passed through a rotating disc that alternately directs the radiation along a reference beam path (going through reference cell) and through a path containing the sample (sample cell). One detector alternately records the signals from both beam paths. The transmittance $T(\lambda)$ is defined as the ratio of the intensity of the light passed through the sample $I(\lambda)$ to the intensity of the reference signal $I(\lambda)_0$. In a transmission spectrum, T is plotted as a

function of wavelength (or an equivalent parameter). Instead of transmittance, the absorbance or optical density A, is often the quantity plotted on the y - axis. Absorbance of the sample is related to the transmittance by the equation,

$$A = - \log_{10} (T) \qquad\qquad 2.2$$

Absorption spectroscopy is used to measure the transmitted signal for transparent (non-scattering) samples such as single crystals or solutions. An alternative technique for strongly scattering materials, such as polycrystalline powders, is diffuse reflection spectroscopy. The difference in set - ups for absorption and reflection spectroscopy is in the detection compartment. When diffuse reflection spectroscopy is used, the backscattered signal is detected and compared to the backscattered signal from a reference material. Polycrystalline powders of MgO or $BaSO_4$ can be used as a reference. The reflectance (R) is plotted on the y - axis and is defined as

$$R = I/I_0(\lambda) \qquad\qquad 2.3$$

where I is the intensity of reflected light and I_0 is the intensity of incident light [21].

2.3.4.2 Experimental details

Absorbance study of the samples was carried out using a Shimadzu, UV - 2450 UV-vis spectrophotometer equipped with an integrating sphere. The instrument has a Tungsten and a Deuterium lamp for excitation. A high performance holographic grating was used as the monochromator in the optical system and a wavelength precision was about 0.3 nm. Detector part is a photomultiplier tube (PMT). For measurements with powders, the samples were positioned at the rear face of an integrating sphere and illuminated with a beam of light. The light reflected from the sample surface was collected by the

integrating sphere, and by means of multiple diffuse reflections, a portion of this light was transferred to the detection system. Barium sulfate was used as a reference. In the present studies, spectra were recorded in the 400 – 700 nm wavelength range.

2.3.5 Luminescence spectroscopy

2.3.5.1 Basic understanding

Studying the luminescence properties of the samples is the most vital part of the phosphor research. Photoluminescence spectra are measured using compact commercial equipment called spectrofluorimeter. Both the emission and excitation characteristics can be recorded using the same instrument. After excitation of the sample to an higher energy state, the transition to the ground state results in the emission of light. This phenomenon is the basis in both emission and excitation spectroscopy [164, 165]. The main components of the instrument are represented in figure 2.7. It contains a broadband excitation source, a light dispersing element for the excitation radiation, a sample compartment, a light dispersing element for the radiation emitted, and a sensitive detector for measuring the intensity of the radiation emitted. Usually, emission and excitation spectra are recorded in the same setup. In emission spectroscopy, the emitted light is spectrally resolved by scanning the emission dispersing element. The dispersing element for the excitation source remains fixed during scanning of the emitted light. An emission spectrum yields information on the energetic positions of the optical transitions that are involved in the emission of light. In excitation spectroscopy, the emission monochromator is set at a wavelength corresponding to a (strong) emission line and the excitation light is scanned.
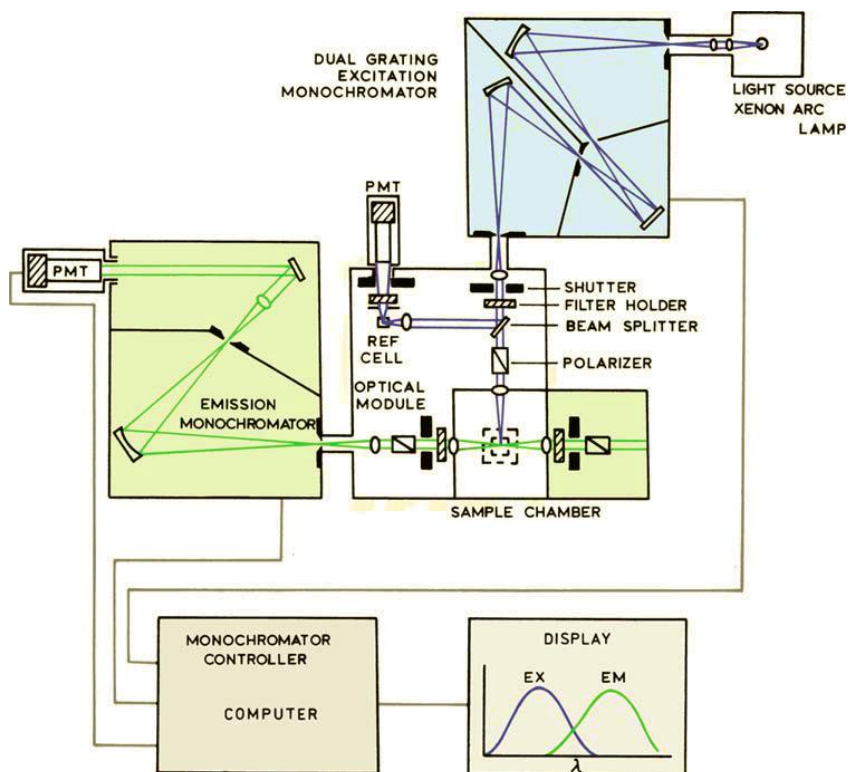
Figure 2.7 Schematic illustration of a spectroflurimeter [163].

In contrast to an absorption spectrum, an excitation spectrum yields information on the energetic position of absorption bands that lead to the emission of the chosen wavelength. Thus the technique is very valuable in studying specific absorption transitions, particularly when more than one optical absorbing species is present in the material.

From the emission spectra, no information about the absolute value of the transition strengths can be obtained, but a comparison of relative intensities (after correction for instrumental response) is straightforward for transitions originating from the same level. In this

case, the observed intensities I_{em} (λ) for transitions to various levels are proportional to the corresponding radiative transition rates.

Lifetimes of the powder samples can be measured by pulsed luminescence experiment using a Phosphorimeter attached to spectrofluorimeter. Luminescence lifetime is the time required for the luminescence intensity to decay from some initial value to 1/e of that value (e = 2.718). There are three general methods for measuring fluorescence lifetimes. Two of them are time domain (Pulse method and Time correlated single photon counting), while the third is a frequency domain technique (Phase modulation). Here the pulse method which uses a pulsed light source in concert with a detector, to measure the decay of a sample directly as it occurs is discussed. The detectors must possess an appropriate response time. The system sweeps through the decay in fluorescence intensity by varying a time delay after the incident light pulse. The observed variation in intensity is used to construct the complete decay curve. After measurement, the pulse width, and a number of instrumental parameters (Incident pulse width, Incident pulse shape, Instrumental response function) must be deconvoluted from the data in order to fit the data properly. Deconvolution is unnecessary if the pulse width and instrument response function are much shorter than the lifetime of the sample. For the lifetime measurement, the sample is excited with pulsed light. The emitted phosphorescence is measured by a photon counting detector with variable delay and open window between pulse and detection. Four important parameters like delay after flash, sample window, time per flash and the number of flashes govern the sequence in phosphorimeter experiment. A typical sequence of data acquisition starts with a flash from the pulsed lamp, sensed by the control module at time t = 0. The light enters excitation spectrometer, where it is

dispersed. Monochromatic light from the spectrometer excites the sample. Luminescence emission from the sample then passes through emission spectrometer to photomultiplier tube detector. The control module includes a gate and delay generator, allowing the signal at detector to be integrated only during a specific period after flash (delay after flash) for a predetermined length of time (sample window). Any signal arriving before or after the gating is ignored. This sequence of excitation, delay and collection is repeated for each lamp pulse. The total signal is accumulated for a predetermined number of exciting pulses (flashes) and saved to the disk. This sequence of excitation, delay, and sampling is repeated for each lamp flash. After collecting the total signal, the software displays the intensity of the luminescence as a function of time or wavelength. The data can be manipulated to calculate lifetime of the sample and other associated parameters [166].

2.3.5.2 Experimental details

The samples were prepared by filling the powder in the groove of a quartz sample holder and leveling the top surface smoothly. The excitation and emission spectra were recorded on a Fluorolog 3 HORIBA fluorescence spectrophotometer with a continuous Xenon lamp (450 W) as the excitation source. Luminescence lifetime of the phosphors was recorded by the FL - 1040 phosphorimeter attached to Fluorolog®3 spectrofluorimeter. The phosphorimeter includes a pulsed xenon lamp, gating electronics to control the size and temporal displacement of the detection window. During lifetime measurements, a pulsed Xenon flash lamp the instrument attached to the dual lamp house was used. The continuous and pulsed light sources could be switched between each other by FluorEssence software control. The detector was a PMT - R928P photon counting detector.

3

PHOTOLUMINESCENT PROPERTIES OF Gd_3MO_7 : Eu^{3+} (M = Nb, Sb, Ta) RED PHOSPHORS

_____

New phosphor materials of general formula $Gd_{3-x}MO_7$: xEu^{3+} (M = Nb, Sb, Ta) were prepared using a high temperature solid state route. Detailed structural studies using powder XRD and Raman spectroscopic techniques showed that niobate and tantalate samples crystallized in weberite type structures whereas the antimonate sample in a fluorite structure. Photoluminescence properties of the three compositions are correlated with their crystal structures. It was observed that more ordering occurs in the lattice when M site is doped from Sb to Nb to Ta. Although niobate and tantalate samples possess similar structure, more distortions were noticed in tantalate sample increasing the radiative transition probabilities. Due to the more ordered structure of Gd_3TaO_7 host lattice resulting in more uniform distribution of Eu^{3+} ions, tantalate system showed better luminescence properties. The variation in luminescence intensity with various Eu^{3+} concentrations in Gd_3TaO_7 host lattice was also studied to calculate the optimum doping concentration.
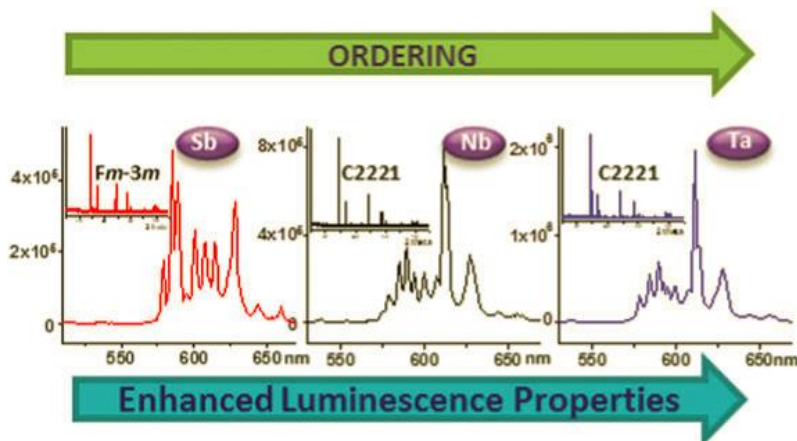
3.1 Introduction

Luminescence properties of the various phosphor materials highly depend on the crystallographic structures of the host lattice and the nature of the activator ion [67, 26]. Thus choosing the host lattice and the activator ions as well as understanding the chemistry and the structure plays a crucial role in the phosphor synthesis. The fluorite structure (AO_2) is considered to be one of the most flexible due to its ability to construct superstructures or derivatives. Pyrochlores and weberites which are anion deficient fluorite related structures ($A_2B_2O_7$), also maintain the closed packed cation layers as in the fluorite structure [134]. If the four tetravalent metal ions in the A and B sites are replaced by three trivalent ions (Ln) and one pentavalent ion (M), one oxide vacancy is formed per fluorite cell. Due to the significant differences in radii between the Ln^{3+} and M^{5+} ions, cation ordering occurs on the metal sites and the oxide - vacancy orders on the anion sites [132]. Depending on the Ln^{3+} and M^{5+} ions there is a wide possibility of almost similar structures with different ordering and defect formation.

The most widely used activator for red luminescence in the phosphor materials are europium ions (Eu^{3+}) due to its high lumen equivalent, quantum efficiency, and photostability at the same time [21, 99]. It is known that the probability of electronic transitions from the lowest $^5D_0$ excited state to the $^7F_{0-6}$ ground states differs depending on site symmetries [167]. Despite extensive studies on various phosphor systems, there is a limited understanding on the dependence of luminescence properties on the local structures and distributions of activator ions in the host lattice. However the photoluminescence spectra provides invaluable information about the nature of the doping sites and dopant locations in the host lattice [168]. Asymmetric ratio

which is the ratio of the integrated intensities of electric dipole and the magnetic dipole transitions provides an estimate to the degree of local distortion and the nature of the doping sites [100]. Another informative spectral feature for assessing the local environment of Eu^{3+} ions is the $^5D_0 \rightarrow {}^7F_0$ transition which occurs between these non-degenerate levels in 577 - 584 nm range. Splitting in this transition points out the dual or more non-equivalent site occupancy of Eu^{3+} ions [169]. The distribution of Eu^{3+} ions in bulk compounds has been a subject of experimental and theoretical interest. Reports clearly reveal the fact that the luminescence emission intensity is higher for more ordered structures due to the more uniform distribution of the activator ions and due to the reduced non-radiative decay pathways.

Crystallographic investigations on Ln_3MO_7 structures can be found dating back as far as 1964 [20, 170]. Since then, there have been considerable discrepancies between various studies on the crystal structure of Ln_3MO_7 reported in literature. There have been numerous studies focusing mainly on the crystallographic aspects and the dielectric properties of the compounds like Ln_3IrO_7, Ln_3MoO_7, Ln_3RuO_7, Ln_3NbO_7, Ln_3TaO_7, Ln_3SbO_7 etc [129, 171, 172]. However most of them are reported as defect – fluorite superstructures. Ordering and the oxygen vacancies depend on the Ln^{3+} and M^{5+} ions. The spectroscopic properties of the doped rare earth ions usually have great influence on the local structures, coordination numbers, ordering and degree of distortion due to defects in the host. The luminescence properties of the compounds with Ln_3MO_7 host lattices are less reported. Recently *Yanyan et al.* studied the luminescence properties of hydrothermally synthesized Lu_3TaO_7, Lu_3NbO_7 and Y_3TaO_7 nanophosphors and reported them as red phosphor candidates for WLEDs upon further improvements [153]. However the compounds of general composition

Ln$_3$MO$_7$ are gaining attraction and form interesting candidates as the host materials for phosphors.

In light of the great importance of the host structure in the red luminescence of Eu^{3+}, the aim of the present work is to explore the structure of Ln$_3$MO$_7$ compounds and to study the distribution and the photoluminescence properties of Eu^{3+} ions in relationship with their structural properties. In this chapter, the photoluminescence properties of Eu^{3+} activated Gd$_3$MO$_7$ (M = Nb, Sb, Ta) red phosphors are presented. The variation in the luminescence intensity with various Eu^{3+} doping concentrations in Gd$_3$TaO$_7$ host lattice was also studied to obtain the optimum doping concentration.

3.2 Experimental section

3.2.1 Synthesis

The phosphors Gd$_{3-x}$MO$_7$: xEu^{3+} (M = Nb, Sb, Ta; x = 0.05, 0.10, 0.15, 0.20) were prepared by a high temperature solid state reaction route. Gd$_2$O$_3$, Nb$_2$O$_5$, Sb$_2$O$_5$, Ta$_2$O$_5$ and Eu$_2$O$_3$ (Sigma Aldrich, 99.99%) were used as the starting materials. Chemicals were weighed in the stoichiometric ratio and then finely ground and mixed in an agate mortar in acetone medium with intermittent drying. The homogeneous mixture was calcined on an alumina plate at 1400°C for 6 h twice powdering and pelletizing after the first calcination.

3.2.2 Characterization

The crystalline structure of the samples was examined with an X-ray powder diffractometer (X'Pert Pro PANalytical, operated at 40 kV and 30 mA, Cu - Kα = 1.5406 Å, 2θ range = 10° - 90°). The FT-Raman spectra of the powdered samples were recorded on a Labram HR 800 (Horiba Scientific, Instrument no L/4/794) spectrometer using argon

laser excitation (784 nm). Fourier transform infrared spectroscopy data were collected on a (Perkin - Elmer Spectrum One FT-IR Spectrometer) over the range of wavenumber 4000 – 400 cm^{-1}, and the standard KBr pellet technique was employed. Morphological studies of powder particles were done by a scanning electron microscope (JEOL, JSM - 5600LV) operated at 15 kV. EDS spectra was also recorded to identify the elements present. Absorbance study of the samples were carried out using a Shimadzu, UV - 2450 UV-vis spectrophotometer in the 400 – 700 nm wavelength range using barium sulfate as a reference. The excitation and emission spectra were recorded on a Fluorolog HORIBA fluorescence spectrophotometer with a Xenon lamp (450 W) as the excitation source. Luminescence lifetime of the phosphors was recorded by the phosphorimeter attached to Fluorolog®3 spectrofluorimeter. All the measurements were carried out at room temperature.

3.3 Results and discussion

3.3.1 Structural studies

Powder X-ray diffraction patterns of $Gd_{2.85}MO_7$: *0.15*Eu^{3+} (M = Nb, Sb, Ta) are shown in figure 3.1. All the samples seemed to match well with a cubic fluorite profile at the first glance. After detailed observation it was found that both $Gd_{2.85}NbO_7$: *0.15*Eu^{3+} and $Gd_{2.85}TaO_7$: *0.15*Eu^{3+} powder diffraction patterns contains more minor peaks with intensities below 5% of the relative intensity which cannot be attributed to the cubic fluorite or pyrochlore structure and can be correctly indexed on the basis of the Gd_3TaO_7 compound (ICDD ref no: 00-038-1409). *Yokogawa et al.* has earlier described the structure as a weberite type with a space group C222$_1$ [173]. The characteristic of this family of weberite is that MO_6 are corner linked to each other and form

chains of MO_6 octahedra with parallel chains of LnO_8 distorted cubes. Thus in a weberite structure there are equal numbers of VI and VIII coordinated cations in an ordered BO_6 - AO_8 layer arrangement [128]. In the case of orthorhombic structures the possibility that the LnI and LnII cations may be of different types, the VIII coordinated and VII coordinated can also be realized. The cation ordering in this specimen may not be complete. In the present study, the degree of ordering in tantalate and niobate samples may be different [174]. It is noticed that the powder XRD pattern of $Gd_{2.85}SbO_7$: $0.15Eu^{3+}$ matched well with cubic fluorite structure (ICDD ref no: 01-074-6419, Space group: *Fm-3m*). Rietveld refinements of the above three samples were carried out for the detailed structural studies. Starting models used for the refinement are given in the tables 3.1 and 3.2 [127]. In all the three cases Eu^{3+} is expected to occupy the Gd^{3+} site considering the matching ionic radius and the coordination number of the ions [175]. The profile was fitted using a Pseudo Voigt profile function. The observed, calculated and the difference powder diffraction profiles of the samples (M = Nb, Sb, Ta) are given in figures 3.2, 3.3, and 3.4 respectively. Table 3.3 gives the refined values of all the samples. The refined R values suggest that the refinement is in good agreement with the space group in all respects. Selected bond distances of the atoms obtained from the Rietveld analysis are given in table 3.4. A small increase in the bond distances and a corresponding lattice expansion is observed in the tantalate system in comparison with the niobate system. This is attributed to the slight difference in the electronegativity of the two cations. Electronegativities of tantalum and niobium are 1.5 and 1.6 respectively. Schematic representation of the crystal structures and the coordination polyhedra of the niobate and the tantalate sample generated using the diamond software is given in figure 3.5 and 3.6.
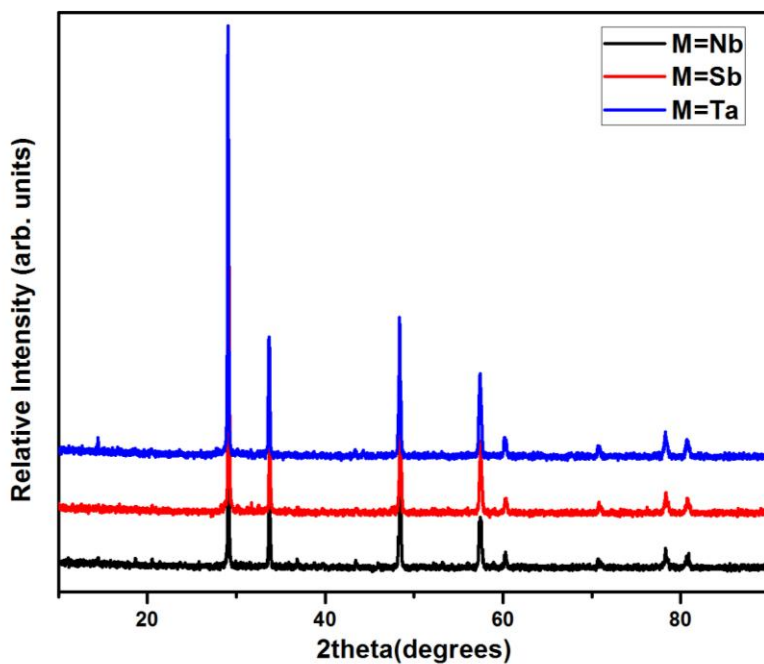
Figure 3.1 Powder X-ray diffraction patterns of $Gd_{2.85}MO_7 : 0.15Eu^{3+}$ (M = Nb, Sb, Ta).

Table 3.1 Starting model of $Gd_{2.85}MO_7 : 0.15Eu^{3+}$ (M = Nb, Ta).

Element	Wyckoff	x	y	z	SOF
Gd	4b	0	0.4954	0.25	0.85
Eu	4b	0	0.4954	0.25	0.15
Gd	8c	0.2338	0.2349	0.002	1
Nb / Ta	4b	0	-0.0005	0.25	1
O	8c	0.129	0.177	0.273	1
O	8c	0.116	0.794	0.281	1
O	4a	0.629	0	0	1
O	4a	0.365	0	0	1
O	4a	0.057	0	0	1

Table 3.2 Starting model of Gd$_{2.85}$SbO$_7$: *0.15*Eu^{3+}.

Element	Wyckoff	x	y	z	SOF
Gd	4a	0	0	0	0.7125
Eu	4a	0	0	0	0.0375
Sb	4a	0	0	0	0.25
O	8c	0.25	0.25	0.25	1
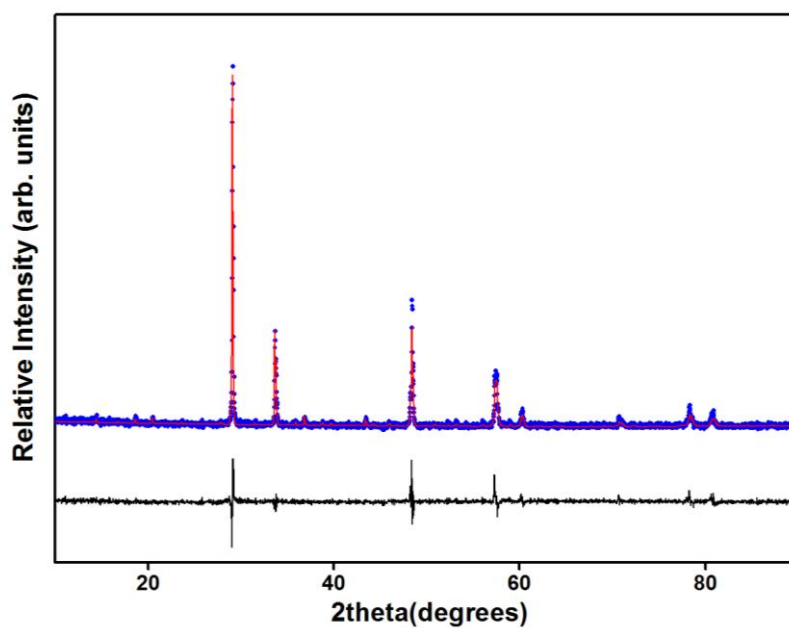
Figure 3.2 Observed (points), calculated (continuous line) and the difference I$_{obs}$ – I$_{calc}$ (bottom line) XRD profiles of Gd$_{2.85}$NbO$_7$: *0.15*Eu^{3+}.
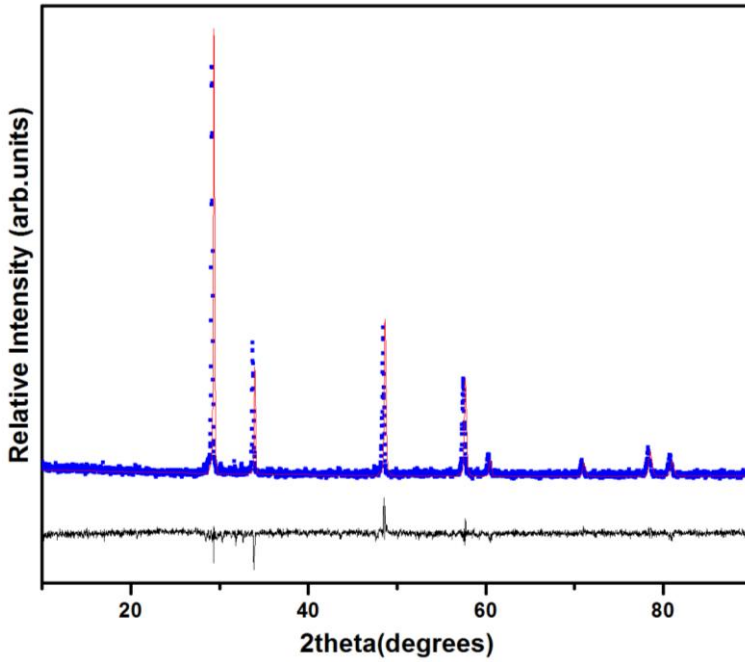
Figure 3.3 Observed (points), calculated (continuous line) and the difference $I_{obs} - I_{calc}$ (bottom line) XRD profiles of $Gd_{2.85}SbO_7 : 0.15Eu^{3+}$.
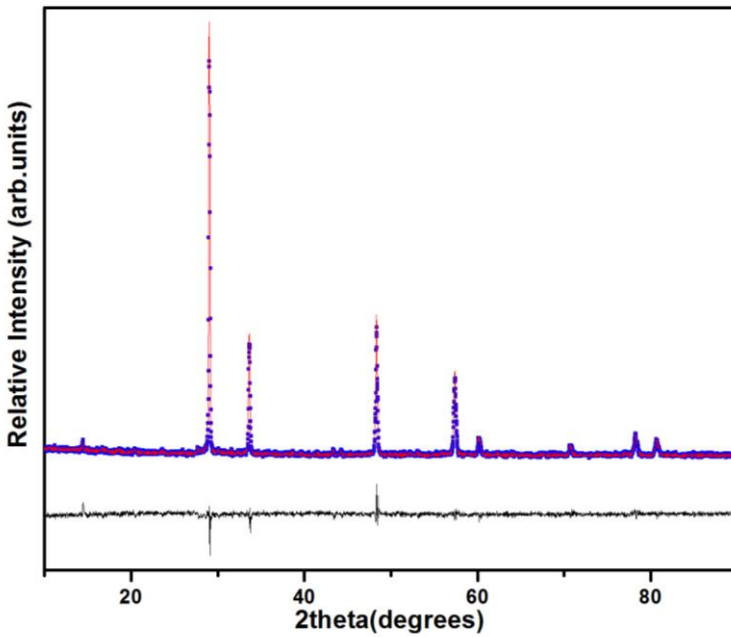
Figure 3.4 Observed (points), calculated (continuous line) and the difference $I_{obs} - I_{calc}$ (bottom line) XRD profiles of $Gd_{2.85}TaO_7 : 0.15Eu^{3+}$.

Table 3.3 Refined parameters of Rietveld analysis of $Gd_{2.85}MO_7$: $0.15Eu^{3+}$ (M = Nb, Sb, Ta).

Sample	M = Nb	M = Sb	M = Ta
Crystal Structure	Orthorhombic	Cubic	Orthorhombic
Space group	$C222_1$	Fm-$3m$	$C222_1$
Flat background	117.4537	116.2166	125.8454
Coefficient 1	-17.6815	-17.3529	-23.4959
Coefficient 2	19.3853	17.9869	22.4623
Scale Factor	0.0000	0.0001	0.0000
Lattice parameters			
a [Å]	10.6035(4)	5.3251(2)	10.6308(5)
b [Å]	7.5175(3)	5.3251(2)	7.5249(3)
c [Å]	7.5348(2)	5.3251(2)	7.5430(4)
Cagliotic parameters			
U	0.2688	0.1350	0.1975
V	-0.1531	-0.0165	-0.0938
W	0.0265	0.0105	0.0190
Asymmetry parameter	1.2454	0.5004	0.4169
Peak Shape 1	0.6545	0.5463	0.8816
Peak Shape 2	0.0003	0.0000	-0.0082
Residual parameters			
Rexp (%)	8.40	8.45	7.92
Rp (%)	7.55	7.28	6.76
Rwp (%)	10.02	9.37	8.70
GOF	1.42	1.22	1.20

Table 3.4 Selected bond distances (in Å) of $Gd_{2.85}MO_7 : 0.15Eu^{3+}$ (M = Nb, Ta).

M = Nb			M = Ta		
Gd	- O3	2.328	Gd1	- O3	2.332
	- O4	2.366		- O4	2.370
	- O2	2.570		- O2	2.574
	- O1	2.762		- O1	2.766
Gd2	- O4	2.248	Gd2	- O4	2.252
	- O3	2.282		- O3	2.285
	- O2	2.325		- O2	2.327
	- O1	2.352		- O1	2.358
	- O1	2.365		- O1	2.366
	- O2	2.481		- O2	2.487
	- O5	2.575		- O5	2.580
Nb	- O1	1.919	Ta	- O1	1.922
	- O5	1.978		- O5	1.981
	- O2	1.988		- O2	1.991
O1	- Nb	1.919	O1	- Ta	1.922
	- Gd2	2.352		- Gd2	2.358
	- Gd2	2.365		- Gd2	2.366
	- O5	2.566		- O5	2.569
	- O1	2.758		- O1	2.764
	- Gd	2.762		- Gd1	2.766
	- O2	2.872		- O2	2.879
	- O2	2.883		- O2	2.886
	- O5	2.930		- O5	2.935
	- O4	2.971		- O4	2.974
	- O3	3.182		- O3	3.185
	- O3	3.359		- O3	3.365
	- O2	3.370		- O2	3.374
O2	- Nb	1.988	O2	- Ta	1.991
	- Gd2	2.325		- Gd2	2.327
	- Gd2	2.481		- Gd2	2.487
	- O2	2.504		- O2	2.510
	- Gd	2.570		- Gd1	2.574
	- O5	2.697		- O5	2.700
	- O4	2.766		- O4	2.768
	- O1	2.872		- O1	2.879
	- O1	2.883		- O1	2.886
	- O5	2.913		- O5	2.918
O3	- Gd2	2.282	O3	- Gd2	2.285
	- Gd	2.328		- Gd1	2.332
	- O4	2.799		- O4	2.806
	- O2	3.064		- O2	3.067
	- O1	3.182		- O1	3.185
	- O1	3.359		- O1	3.365
O4	- Gd2	2.248	O4	- Gd2	2.252
	- Gd	2.366		- Gd1	2.370
	- O2	2.766		- O2	2.768
	- O3	2.799		- O3	2.806
	- O1	2.971		- O1	2.974
	- O5	3.266		- O5	3.274
O5	- Nb	1.978	O5	- Ta	1.981
	- O1	2.566		- O1	2.569
	- Gd2	2.575		- Gd2	2.580
	- O2	2.697		- O2	2.700
	- O2	2.913		- O2	2.918
	- O1	2.930		- O1	2.935
	- O4	3.266		- O4	3.274

Figure 3.5 Schematic representation of crystal structure and the coordination polyhedra of Gd$_{2.85}$NbO$_7$: 0.15Eu^{3+}.
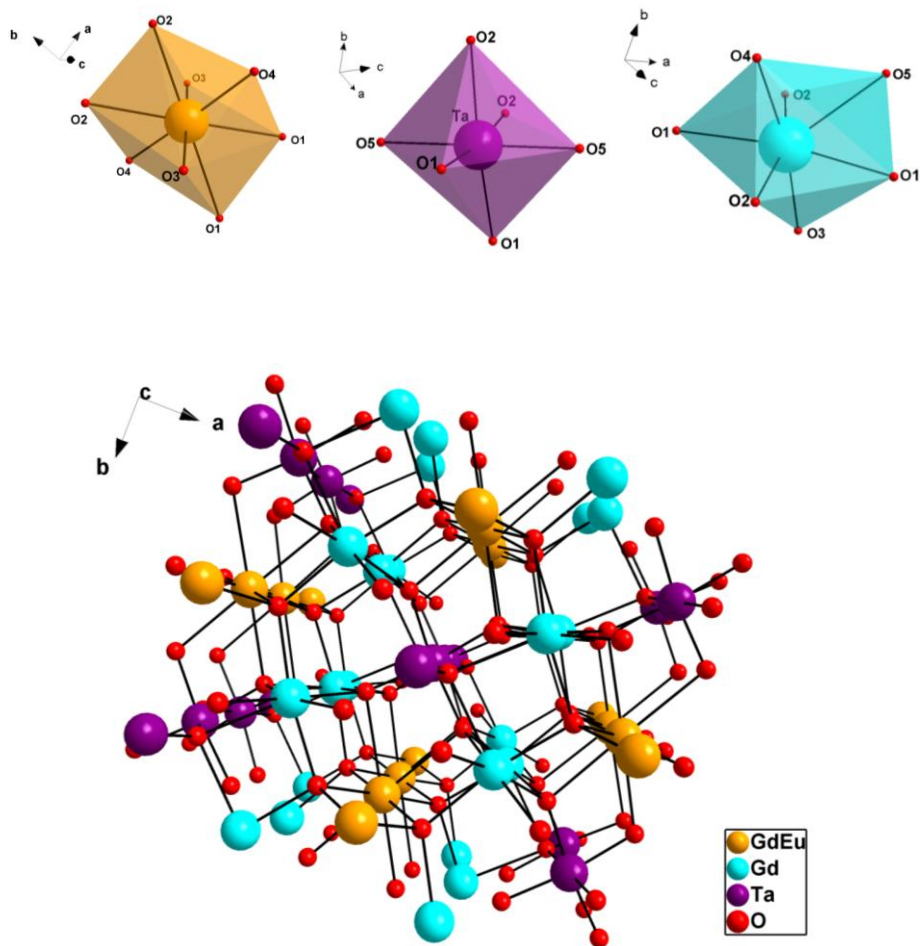
Figure 3.6 Schematic representation of the crystal structure and the coordination polyhedras of $Gd_{2.85}TaO_7 : 0.15Eu^{3+}$.

FT-IR spectra of the three samples are given in figure 3.7. As expected from the XRD analysis niobate and tantalate samples showed similar modes of vibrations whereas the antimonate sample possessed totally different type spectra. It is predicted that the higher the ratio of formula volume to Ln^{3+} ionic radius, higher the probability of polar

distortions [148]. The presence of more IR vibrational peaks in the tantalate sample is thus attributed to the higher distortions in the structure owing to "looseness" of the system which can also be related to the increased bond lengths. It is known that for a vibration to be IR active there must be a change in the dipole moment vector. Thus from the FT-IR spectra it can be understood that the tantalate system possess more bonds associated with a net dipole moment change.
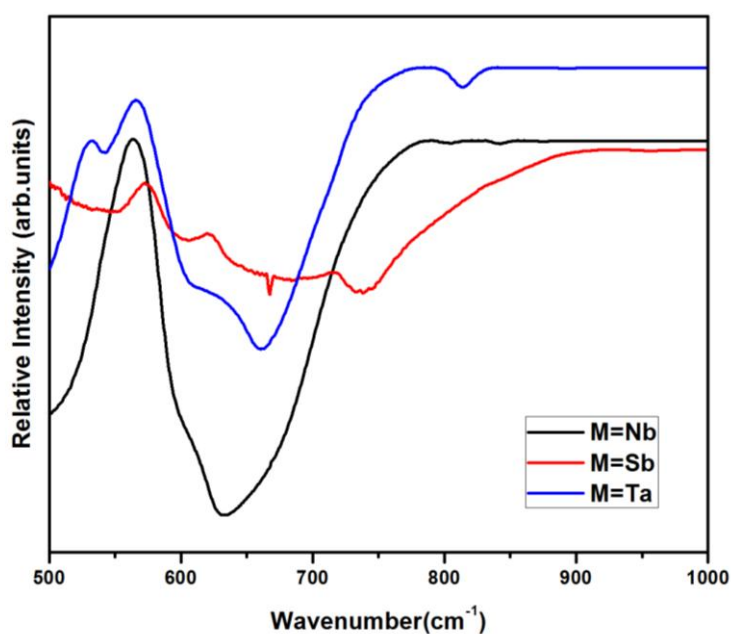
Figure 3.7 FT-IR spectra of $Gd_{2.85}MO_7 : 0.15Eu^{3+}$ (M = Nb, Sb, Ta) samples.

According to *Cai et al.* larger unit cell volume probably contributes a greater BO_6 distortion [149]. Thus the FT-IR results indirectly points to the possibility that the Eu^{3+} ions may be located in a more distorted site in the case of tantalate system than in the case of the niobate system. Further confirmation of the structures of the three

samples was done by recording the FT-Raman spectra of the samples. Figure 3.8 gives the FT-Raman spectra of the samples.
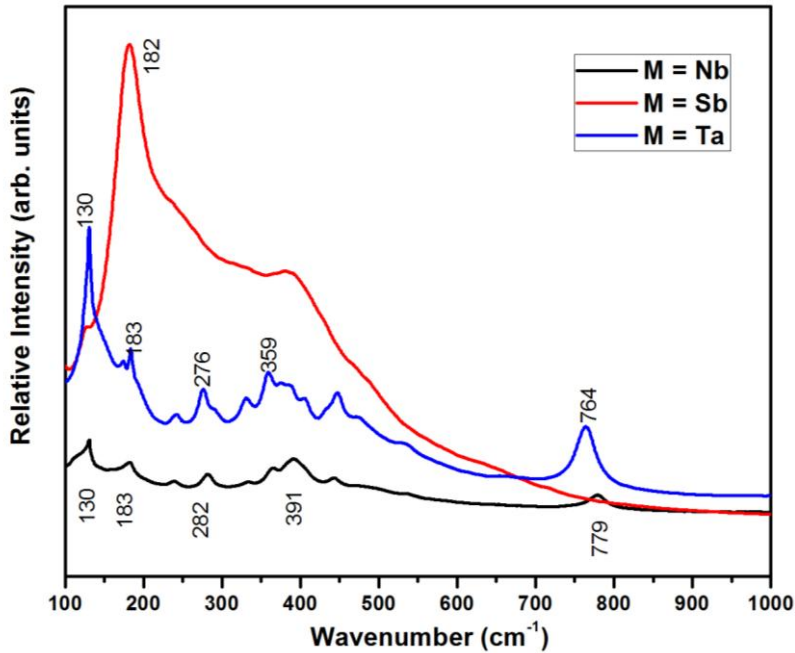
Figure 3.8 FT-Raman spectra of Gd$_{2.85}$MO$_7$: 0.15Eu^{3+} (M = Nb, Sb, Ta) samples.

The Raman spectra of Gd$_{2.85}$SbO$_7$: 0.15Eu^{3+} clearly revealed the fluorite structure of the compound [176]. In Raman studies also, niobate and tantalate samples showed similar modes of vibrations which correspond to the weberite structure with some variation in the intensity [141]. But the observation was that some minor modes which were not present in the niobate sample were observed in the tantalate sample. According to *Siqueria et al.*, in the weberite C222$_1$ structure, almost 63 modes ($14A_{1g}$ + $18B_{1g}$ + $16B_{2g}$ + $15B_{3g}$) are Raman active [138]. Oxygen redistribution in the lattice leading to the formation of different polyhedra of different coordination can lead to presence or

absence of some modes in the Raman spectra. The sharper and intense lines in the Raman spectra of the tantalate sample indicate the redistribution of oxygen in the sample due to some distortions resulting in the presence of more Raman vibrational modes. The high frequency line ν_1 (A_{1g}) at 764 cm^{-1} (tantalate) and 779 cm^{-1} (niobate) sample corresponds to the stretching vibrations of Nb/Ta - O bonds in the $(Nb/Ta)O_6$ octahedra. The shift in the lines towards the higher frequencies may be caused by the shorter Nb - O bonds in the NbO_6 octahedra in comparison with that of TaO_6 octahedra which is again in agreement with the smaller lattice parameter values of niobate samples obtained from the Rietveld results. Again the ν_1 (A_{1g}) line is very sensitive to the structural ordering. The lines are weaker for the disordered structures [151]. This points out to the more ordered nature of the tantalate system. Thus some distortions and the more ordered nature of tantalate system that could not be well detected from the XRD studies could be identified from both FT-IR and FT-Raman studies.

3.3.2 Morphological studies

Typical scanning electron micrographs of $Gd_{2.85}MO_7 : 0.15Eu^{3+}$ (M = Nb, Sb, Ta) are given in figure 3.9. All three samples were slightly agglomerated and the particle sizes are in between 0.5 - 1 μ. EDS spectra of samples were recorded and the atomic mass percentages were found to be in well agreement with the theoretical stoichiometry. X-ray dot mapping of samples were also carried out to study the distribution of elements and are given in figures 3.10, 3.11 and 3.12. The results show the more uniform distribution of Eu^{3+} in tantalate system.
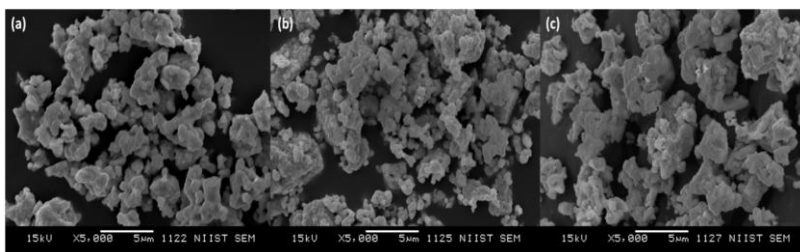
Figure 3.9 Scanning electron micrographs of $Gd_{2.85}MO_7 : 0.15Eu^{3+}$ M = Nb (a), Sb (b), Ta (c).

Element	Weight%	Atomic%
O K	28.02	77.57
Nb L	10.87	5.18
Eu L	2.87	0.84
Gd L	58.24	16.41
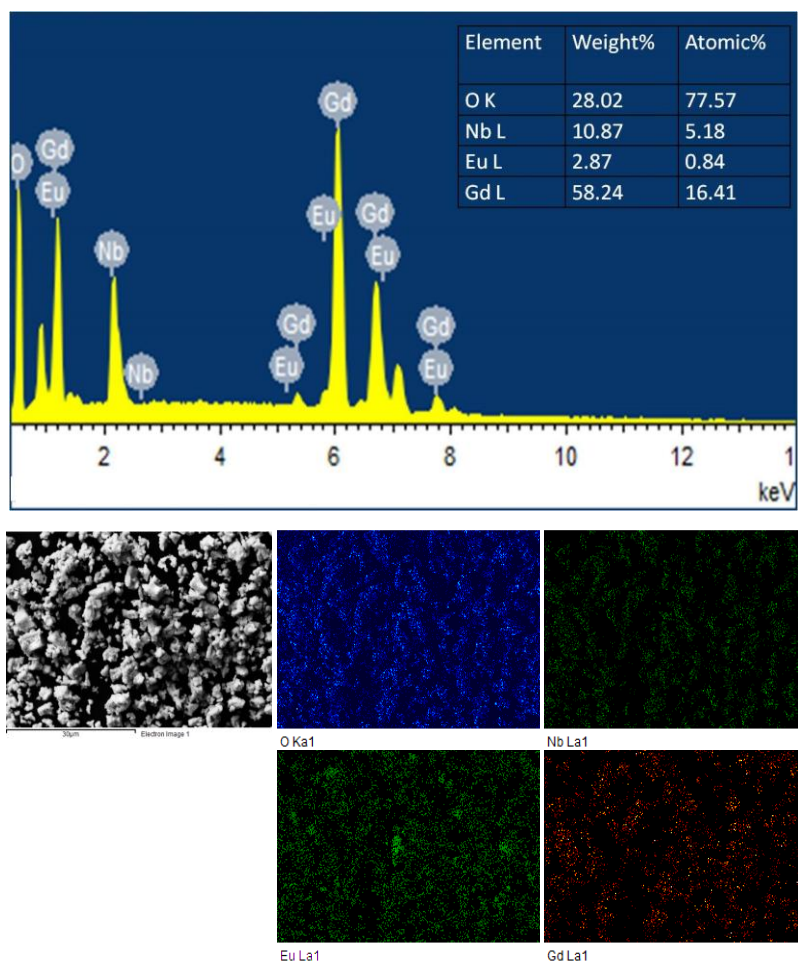
Figure 3.10 EDS spectra and the X-ray dot mapping of $Gd_{2.85}NbO_7 : 0.15Eu^{3+}$ sample.
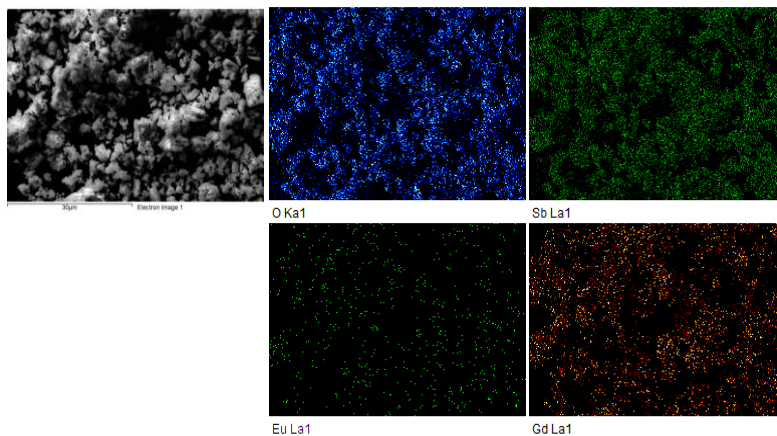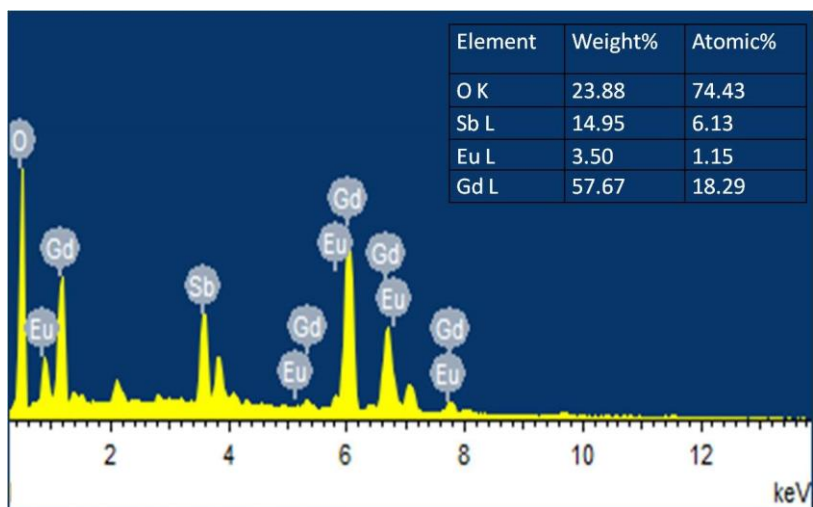
Figure 3.11 EDS spectra and the X-ray dot mapping of $Gd_{2.85}SbO_7 : 0.15Eu^{3+}$ sample.

Element	Weight%	Atomic%
O K	21.01	72.99
Eu L	3.15	1.15
Gd L	55.44	19.59
Ta M	20.40	6.27
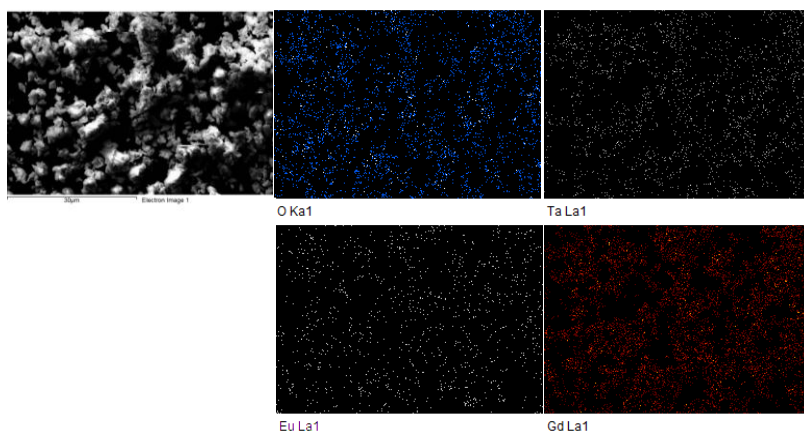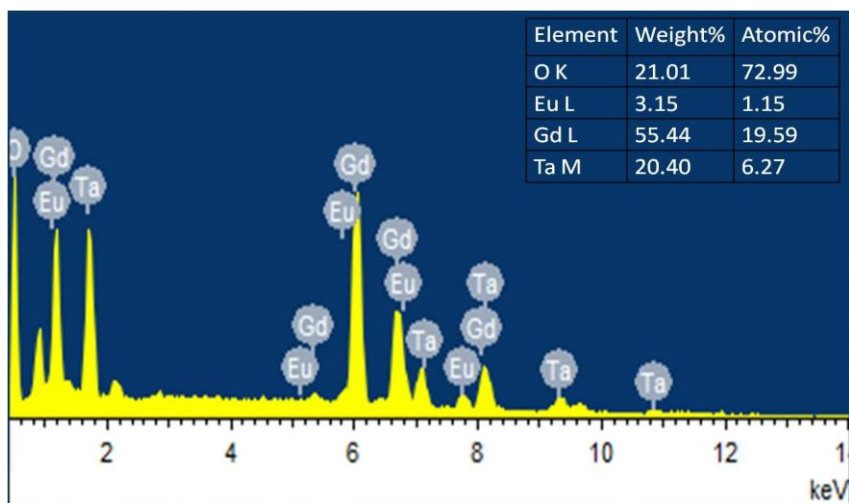
Figure 3.12 EDS spectra and the X-ray dot mapping of $Gd_{2.85}TaO_7 : 0.15Eu^{3+}$ sample.

3.3.3 Photoluminescence properties

Photoluminescence properties of all the samples were studied and the excitation and emission spectra of three samples are given in figures 3.13 and 3.14 respectively. Broad band in the excitation spectra ranging from 240 – 325 nm corresponds to the overall combination of charge transfer transition in metal - oxygen polyhedron of the compound [177]. The narrow peaks beyond CTB correspond to the intra configurational 4f – 4f transitions of Eu^{3+} ions in the host lattice. The most intense peaks at 394 and 464 nm is assigned to $^7F_0 \rightarrow {}^5L_6$ and $^7F_0 \rightarrow {}^5D_2$ transitions respectively [24].
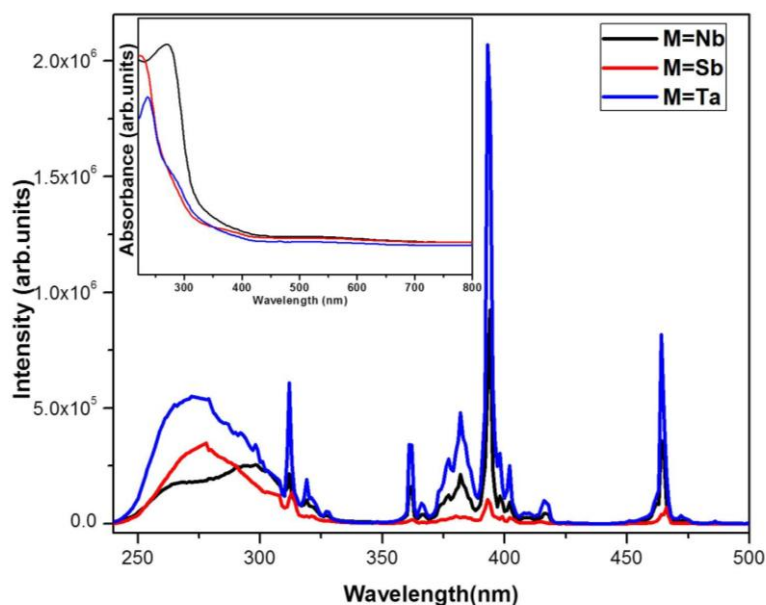
Figure 3.13 Photoluminescence excitation spectrum of $Gd_{2.85}MO_7 : 0.15Eu^{3+}$ (M = Nb, Sb, Ta) for an emission at 612 nm (Inset: UV-visible absorption spectrum of samples).

Niobate sample has a broader and less intense CTB with a maximum at 294 nm in the near UV region in comparison with antimonate (278 nm) and tantalate (272 nm) system. The red-shift of the CTB in the case of niobate sample is related to the lower ionization potential of niobium (6.88 V) in comparison with tantalum (7.89 V). Higher absorption of the niobate sample in the UV region is understood from the absorption spectrum (inset of figure 3.13). Absorption spectra of all the three samples show good absorption in the UV region pointing to the applicability of these phosphor materials with UV led chip. In the niobate sample the intensity of the f - f transitions are more intense than the charge transfer band. Similarly in the case of tantalate system the f - f transitions are more intense than CTB. However, $Gd_{2.85}SbO_7$: $0.15Eu^{3+}$ shows very weak excitation spectra than the other two samples. This can be related to the fluorite structure of antimonate sample which is more disordered structure than the weberite leading to the non uniform distribution of Eu^{3+} ions. Also it is inferred that SbO_8 is less effective in transferring energy to the activators when compared to NbO_6 and TaO_6 groups. Unlike the tantalum and niobium systems CTB is much higher than the f - f transition peaks.

The emission profiles of the three samples are different. The emission intensities under an excitation wavelength of 394 nm were in accordance with the intensities of the $^7F_0 \rightarrow {}^5L_6$ transition peaks in the excitation spectrum. The asymmetric ratio (ratio of electric dipole and magnetic dipole transitions) provides information about the site occupancy of Eu^{3+} ions in the gadolinium sites. Better asymmetric ratio of the tantalate (2.8) sample shows the slightly more occupancy of Eu^{3+} ions in more non-centro symmetric sites in comparison with the niobate sample (2.4). To examine the details of the site distribution of Eu^{3+} ions $^5D_0 \rightarrow {}^7F_0$ transition under 394 nm excitation was investigated

in detail and no evident spliting was observed indicating the occupancy of Eu^{3+} ions in a single site, mostly an 8 coordinated site. The probability of electric dipole transitions ($^5D_0 \rightarrow {}^7F_2$) is rapidly promoted when the doped Eu^{3+} ions is occupied at a highly distorted 8 coordinated sites. Thus in the tantalate system, Eu^{3+} being located at a more distorted site than the niobate sample and the probability of ED transitions is higher.
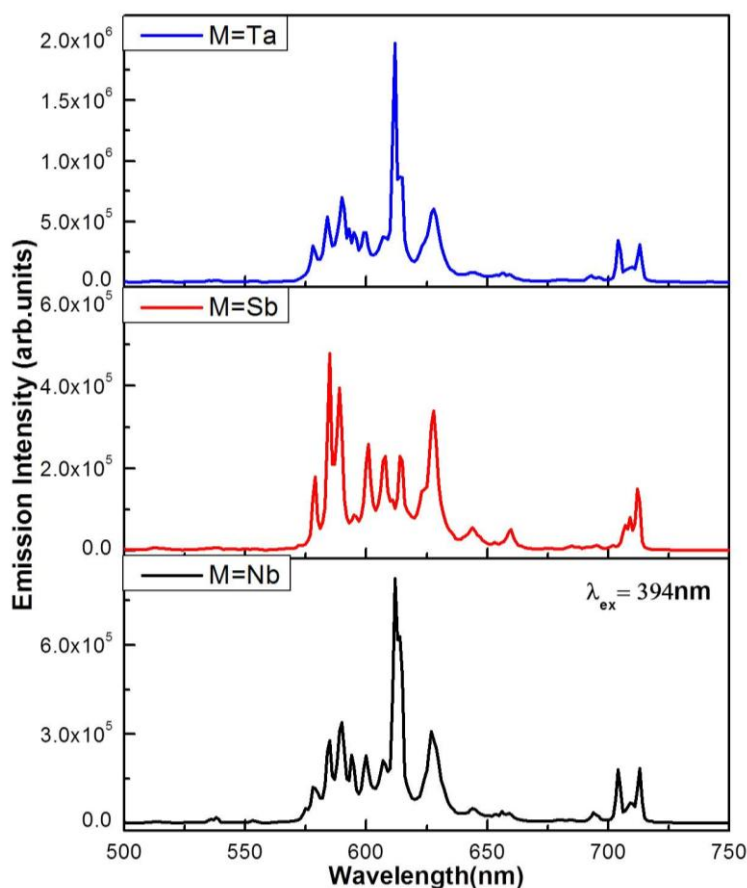
Figure 3.14 Photoluminescence emission spectra of $Gd_{2.85}MO_7$: $0.15Eu^{3+}$ (M = Nb, Sb, Ta) under 394 nm excitation.

It is clear from the spectra that the tantalate samples show maximum emission intensity which is more than twice (2.4 times) the niobate system. Bond distances also play a crucial role in the luminescence intensity of the phosphor materials. This phenomenon is attributed to the crystal field effect. When the Ln - O bond is short (strong crystal field effect), it could favour the energy transfer which harms the luminescence from Eu^{3+} - Eu^{3+} f - f transitions [28]. It could be suggested that the detailed understanding of the site distribution and the host structure is needed for the deeper analysis of the luminescence mechanisms.

The decay curves for $^5D_0 \rightarrow {}^7F_2$ transition (612 nm) of $Gd_{2.85}MO_7$: *0.15*Eu^{3+} (M = Nb, Ta) under near UV excitation are shown in figure 3.15. Decay curve of antimonate sample was not recorded since the sample had very weak orange - red emission. Both the decay curves can be fitted well with a single exponential function given as;

$$I = A \exp (-x/\tau) \hspace{3cm} 3.1$$

where, I, τ and A are intensity, decay time and fitting parameter respectively.

The lifetime was obtained as 0.6429 ms for niobate sample and 0.7937 ms for tantalate system. The decay lifetimes (τ) is proportional to the transition probability. Larger distortion of the crystallographic sites usually denotes the higher transition probability of Eu^{3+} ions. Thus the higher lifetime of the tantalate sample further confirms the more uniform distribution of Eu^{3+} ions in the Gd_3TaO_7 lattice. The defects in the weberite structure of the niobate samples also produces more non-radiative decay pathways reducing the lifetime [55]. From the excitation, emission and lifetime spectra tantalate sample was

showing better luminescence properties and thus further studies were confined to that system.
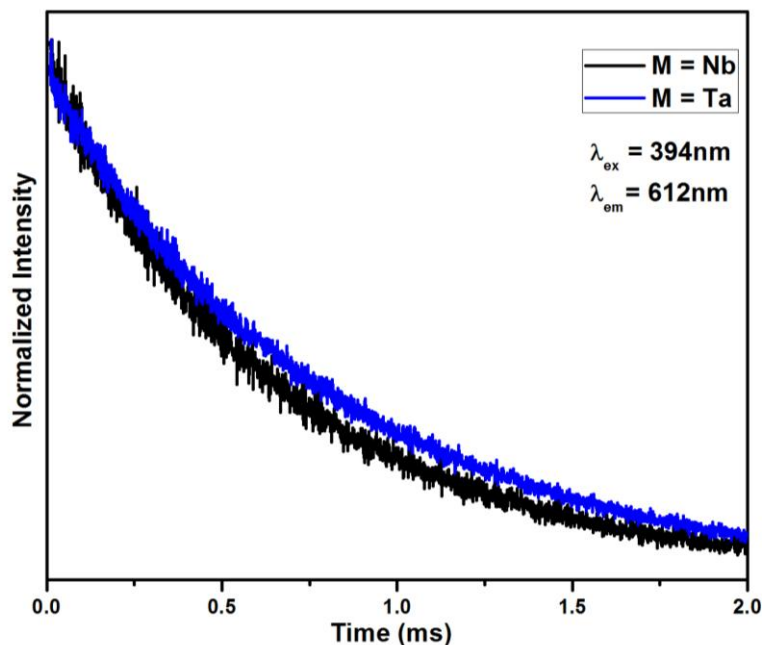
Figure 3.15 Decay curves of Eu^{3+} emission at 612 nm in Gd$_{2.85}$MO$_7$: 0.15Eu^{3+} (M = Nb, Ta) under 394 nm excitation.

3.3.4 Effect of Eu^{3+} doping in Gd$_3$TaO$_7$ host lattice

Powder X-ray diffraction patterns of Gd$_{3-x}$TaO$_7$: xEu^{3+} (x = 0.05, 0.1, 0.15, 0.2) given in figure 3.16 reveal the crystallinity and phase purity of all the samples and they are in good agreement with the powder diffraction pattern of weberite Gd$_3$TaO$_7$ compound (Space group: C222$_1$; ICDD ref no: 00-038-1409). The substitution of the Gd^{3+} ion (1.05 Å, coordination number, CN = 8) by slightly larger Eu^{3+} ion (1.066 Å, CN = 8) results in the lattice expansion, which is confirmed by the shift of XRD peaks of Gd$_{3-x}$TaO$_7$: xEu^{3+} towards the lower 2θ angle side with increasing Eu^{3+} content [178]. The shift of the XRD peak

towards left is shown in the inset of figure 3.16. No impurity peaks were seen with increasing doping concentration Eu^{3+} in the Gd_3TaO_7 lattice.
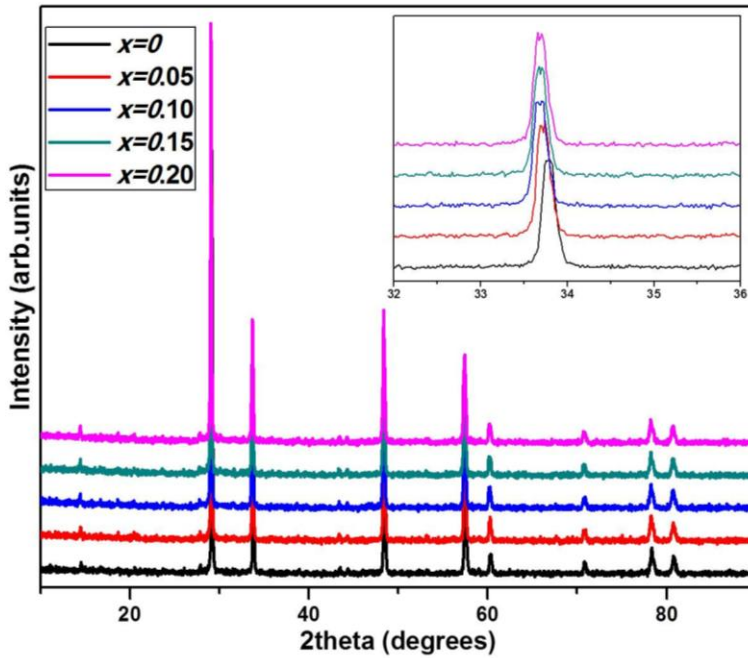
Figure 3.16 Powder X-ray diffraction patterns of $Gd_{3-x}TaO_7 : xEu^{3+}$ (x = 0.05, 0.1, 0.15, 0.2).

Critical influence of activator concentration in the luminescence intensity was studied and the recorded excitation and emission spectra of $Gd_{3-x}TaO_7 : xEu^{3+}$ (x = 0.05, 0.1, 0.15, 0.2) are shown in figure 3.17. Increase in the Eu^{3+} content doesn't change the shape and peak positions of the excitation and emission spectra although the intensity changes. The variation of emission intensity with Eu^{3+} doping concentration under 394 nm is shown in figure 3.18.
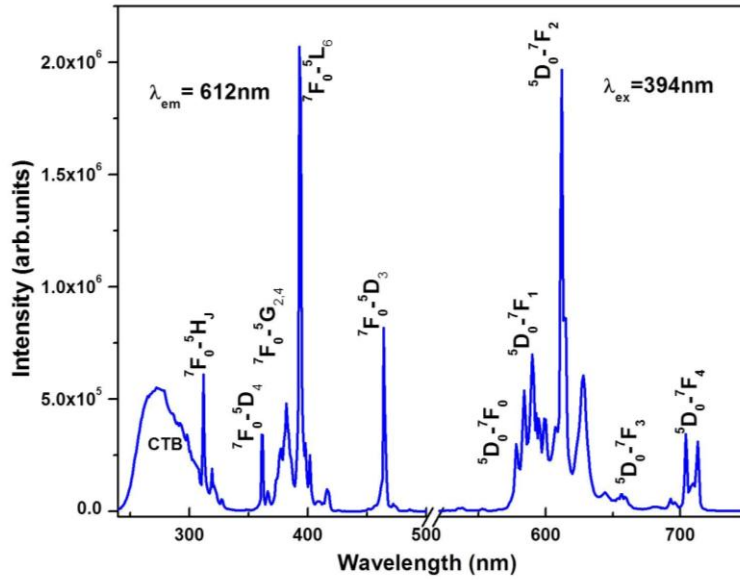
Figure 3.17 Photoluminescence emission spectra under 394 nm excitation and excitation spectrum for an emission at 612 nm of $Gd_{2.85}TaO_7 : 0.15Eu^{3+}$.
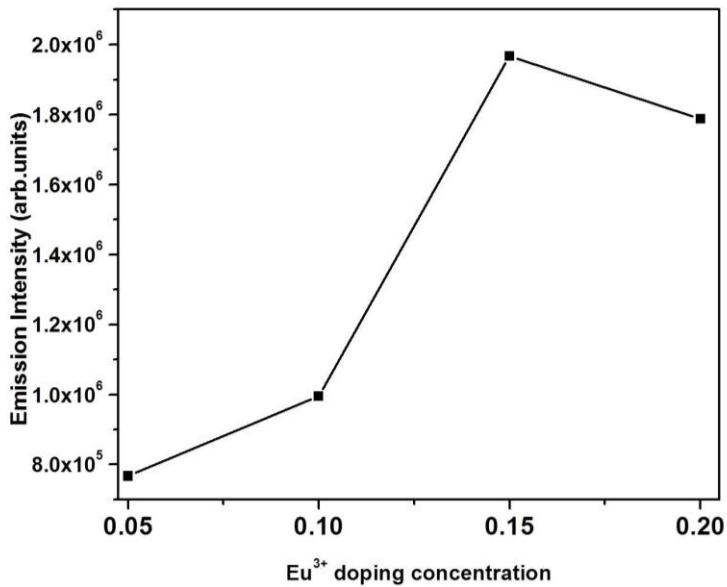
Figure 3.18 Variation of luminescent intensities with Eu^{3+} doping concentrations in $Gd_{3-x}TaO_7 : xEu^{3+}$ (x = 0.05, 0.1, 0.15, 0.2).

At low concentration ranges (up to $x = 0.15$) the luminescence intensity gradually increases with doping content as multiphonon and cross relaxation processes are the major reasons for the electrons in the excited states to enter the $^5D_0$ level. When the distance between the Eu^{3+} ions satisfies the Dexter and Forster resonant energy transfer condition, concentration quenching happens. By further increase in the doping concentration, energy transfer processes known as second order interactions and spin relaxation occur easily between the coupled excited Eu^{3+} ions resulting in the decline of luminescence intensity [178 - 180]. Thus the emission intensity decreases with further increase in doping concentration. Similar emission profiles with slightly lesser intensities were obtained under 464 nm excitation. The decay curves of all the samples are given in figure 3.19 and lifetime values with increasing concentrations from $x = 0.05$ to 0.2 are 0.95, 0.82, 0.79 and 0.75 ms respectively.
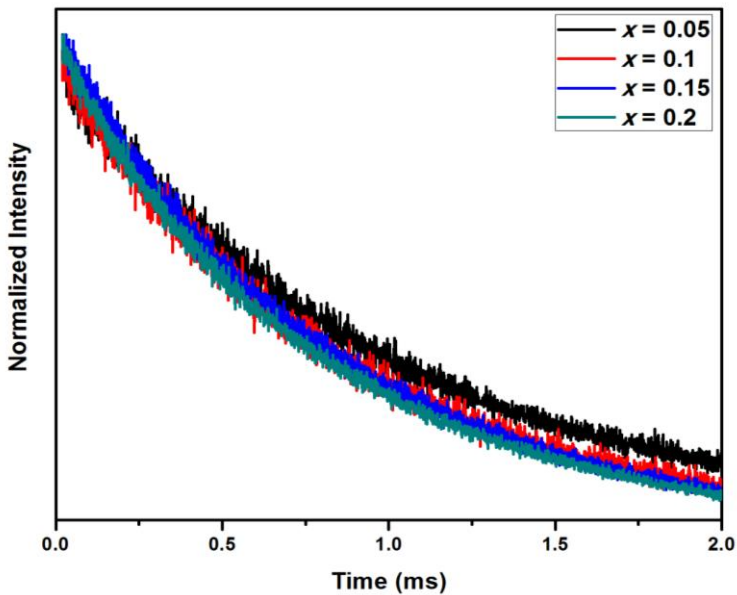
Figure 3.19 Decay curves of Eu^{3+} emission at 612 nm in $Gd_{3-x}TaO_7 : xEu^{3+}$ (x = 0.05, 0.1, 0.15 and 0.2) under 394 nm excitation.

3.4 Conclusions

In summary, the detailed structural and optical studies of three systems with general formula Gd_3MO_7 were carried out. Studies revealed that the tantalate sample showed better luminescence properties in terms of emission intensity, asymmetric ratio and lifetimes. It was noticed that degree of ordering in the crystal structure as well as the local distortions in the luminescent sites plays crucial roles in the luminescence properties. The variation in the luminescence intensity with different Eu^{3+} concentration was studied in Gd_3TaO_7 host system and the doping concentration was optimized. The excitation and emission spectra of the prepared samples indicate that phosphor material can be effectively excited by UV and blue light (394 and 464 nm) and it exhibits intense red emissions, nicely fitting in with the widely applied UV and blue LED chips.

4

PHOTOLUMINESCENT PROPERTIES OF Ln_3TaO_7 :Eu^{3+} (Ln = La, Gd, Y, Lu) RED PHOSPHORS

Eu^{3+} doped Ln_3TaO_7 (Ln = La, Gd, Y, Lu) red phosphors were prepared using a solid state route. The Ln^{3+} substitution induces variation of crystalline structure from a defect fluorite to weberite types with increased ordering of the cations from Lu to La. These phosphors show strong absorptions at near UV wavelength and emit orange - red luminescence. The increased trend in luminescence lifetime further surmises the uniform distribution of Eu^{3+} ions from Lu to La. The luminescence intensity and quantum efficiency are closely related to the degree of ordering of the cations in the lattice. The Eu^{3+} luminescence in La_3TaO_7 embodies the variation of cationic coordination from VII to VIII through intense multiband $^5D_0 \rightarrow {}^7F_{0,1,2,4}$ transitions to only dominant hypersensitive electric dipole $^5D_0 \rightarrow {}^7F_2$ transition. All the Eu^{3+} emission transitions ($^5D_0 \rightarrow {}^7F_{0,1,2,4}$) are more intense and efficient in VII coordination due to increased polarizability and covalent nature of Eu^{3+} bonding environment with the surrounding.
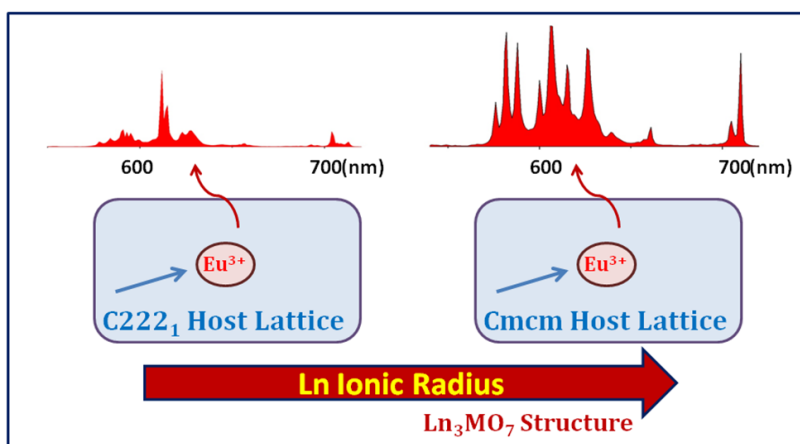
4.1 Introduction

In view of the great importance of red phosphors towards the development of white LEDs in the lighting industry, the study of Eu^{3+} luminescence in various host systems gains attraction [53, 181]. It is well known that the emission characteristics of Eu^{3+} highly depend on the crystal structure of the host lattice, doping site, doping concentration, ordering of the host lattice, uniformity in the activator distribution and various other factors [67, 168]. The probability of electronic transitions from the lowest $^5D_0$ excited state to the $^7F_{0-6}$ ground states differs depending on site symmetries. According to Judd - Ofelt theory, when Eu^{3+} ion occupies a crystallographic site that does not coincide with a centre of symmetry, odd crystal field terms lifts the parity prohibition in the electric dipole (ED) transition. The hypersensitive forced ED $^5D_0 \rightarrow {}^7F_2$ transition results in the emissions in the red wavelength region ($\sim$ 612 nm) along with the allowed magnetic dipole (MD) $^5D_0 \rightarrow {}^7F_1$ transition in the orange wavelength region ($\sim$ 590 nm). On the other hand when the Eu^{3+} ion is located at a site with inversion symmetry, only allowed MD transitions are possible [182, 183]. Spherical symmetry of the Eu^{3+} ions are broken when placed in a crystalline environment and 2J+1 degeneracy of a $^{2s+1}L_j$ multiplet is partially or totally removed. The multiplet is thus split into different crystal field levels. The number of these split levels can be determined from the symmetry of the site [184]. Thus it is a tricky task to find out the suitable host lattice for the Eu^{3+} ions to have better emission characteristics.

Rare earth niobates and tantalates with a general formula, Ln_3MO_7 have great compositional diversity and gained great attraction as functional materials due to their magnetic, conductive and optoelectronic behavior [142, 143, 148, 151, 153]. These kind of

compounds which contain both lanthanides (4f metals) and transition metals (4d or 5d) can adopt diverse structures with different site symmetries; ranging from cubic (space groups: *Fm*-3*m*, *Fd*-3*m*, Ia-3 etc) to its many orthorhombic super structures (space groups: Cmcm, Ccmm, C222$_1$, etc)[127 - 129]. These types of closely related structures offer ample opportunity to understand the factors that influence the Eu^{3+} luminescence. In lanthanides, the 4f atomic orbitals are lying deeply inside the atom, well shielded from its external environment by the valence electrons giving rise to a number of discrete energy levels. Thus the chemistry of the lanthanides are largely determined by their atomic radii. There is considerable amount of literature on the crystal structure of Ln_3MO_7 (Ln = La, Gd, Eu, Dy, Y, Lu; M = Nb, Sb, Ta, Ir etc) type compounds[130, 137, 138, 144, 145, 148, 149, 155]. Most of such compounds with general formula Ln_3MO_7 are derived from the basic fluorite MO_2 (M_4O_8) structure by creating oxygen vacancies in the lattice. Cubic pyrochlore and C-type structures are formed by removing 1/8th and 1/4th of the oxygen atoms respectively in an orderly manner. The reduction in the number of anions leads to a decrease in the coordination number of M cations. Thus there will be VI and VIII coordinated cationic sites in the host lattice so as to keep the compound neutral. In some cases, the compounds form orthorhombic weberite type structures and a different cationic configuration between the layers leads to VII coordinated sites also. Ordering and the oxygen vacancies in these type of structures depend on the Ln^{3+} and M^{5+} cations [185]. Reports show that the change in the crystal structure from fluorite type cubic structure to weberite type orthorhombic structure happens on increasing ionic radius of the Ln^{3+} ion. The study of the photophysics and the radiative transitions of luminescent ions in

such host matrices are less discussed and thus has academic as well as industrial interests.

Our group has been working on the Eu^{3+} luminescence in this family of host lattices. Our recent investigation indicates that better luminescence properties can be achieved in Eu^{3+} doped tantalate based host system [186]. Thus in the present study we focused to the tantalate system and it is observed that the substitution of lanthanide ions in Ln_3TaO_7 (Ln = La, Gd, Y, Lu) system induces variation of crystal structure from a cubic defect fluorite to orthorhombic weberite type with increase of long range ordering of the cations from Lu to La. Furthermore, since the rare earth elements show a linear relationship between ionic radius and polarizability, the proposed system Ln_3TaO_7, provides an opportunity to study the photoluminescence properties in relation with ionic radii and polarizability within these closely related structures. Among these compounds, as described above La_3TaO_7 crystallizes into orthorhombic type structure with a space group Cmcm in which La ions have two different lattice sites with surrounding oxygens in VII and VIII coordination respectively. The increased substitution of Eu^{3+} in this system infers that Eu^{3+} prefers to occupy the VII coordinated site of La for lower substitutions and then changes to VIII coordination with variation in the space group from Cmcm to $C222_1$ through emission wavelength due to hyper sensitive electric dipole transition, $^5D_0 \rightarrow {^7F_2}$ shifting to red. Thus in this work, the study of photoluminescence properties of Eu^{3+} activated tantalate system of general formula $Ln_{3-x}TaO_7 : xEu^{3+}$ (Ln = La, Gd, Y, Lu) in connection with their crystal structures is carried out. The activator doping concentration was fixed at x = 0.15 (5 mol%) in all the prepared samples to study the influence of long range order and coordination of cations associated with the structural variation on the

photoluminescence properties in this system. The effect of Eu^{3+} doping concentration on the emission characteristics was also discussed in relation to the phase evolution.

4.2 Experimental section

4.2.1 Synthesis

The phosphors $Ln_{3-x}TaO_7 : x Eu^{3+}$ (Ln = La, Gd, Y, Lu) were prepared using solid state reaction route. Starting materials La_2O_3, Gd_2O_3, Y_2O_3, Lu_2O_3, Ta_2O_5 and Eu_2O_3 (Sigma Aldrich, 99.99%) were weighed in the stoichiometric ratio and finely ground and mixed in an agate mortar in acetone medium with intermittent drying. The homogeneous mixture was calcined twice on an alumina plate at 1400°C for 6 h.

4.2.2 Characterization

The crystalline structure of the samples was examined using a powder X-ray diffractometer of X'Pert Pro PANalytical make, operated at 40 kV and 30 mA using a Cu-Kα (λ = 1.5406 Å) radiation in the 2θ range, 10 - 90°. Rietveld refinement of the obtained XRD data was carried out using X' Pert Highscore Plus software. FT-Raman spectra of the powdered samples were recorded on a Labram HR 800 (Horiba Scientific, Instrument no L/4/794) spectrometer using 784nm Ar laser excitation. Morphological studies of powder particles were done by a scanning electron microscope (Carl Zeiss - EVO18) operated at 15 kV. Elemental analysis and X-ray dot mapping of the samples were carried out using energy dispersive spectrometer (EDS) attached to SEM. Absorbance study of the samples were carried out using a Shimadzu UV - 2450, UV-vis spectrophotometer in the 400 – 700 nm wavelength range using barium sulfate as a reference. The excitation and emission spectra were recorded on a Fluorolog HORIBA fluorescence®3

spectrophotometer with a Xenon lamp (450 W) as the excitation source. Luminescence lifetime of the phosphors was recorded by the phosphorimeter attached to the spectrofluorimeter.

4.3 Results and discussion

4.3.1 Structural studies

The purity and the crystallinity of the as prepared samples were checked by powder X-ray diffraction analysis. XRD patterns of $Ln_{2.85}TaO_7$: 0.15Eu^{3+} (Ln = La, Gd, Y, Lu) are given in figure 4.1 and all the diffraction lines can be indexed to the ICDD ref. files 01-073-8085, 00-038-1409, 00-048-0265 and 00-024-0697 respectively for La, Gd, Y and Lu substituted compounds. The change in the crystal structure with different substitutions is in accordance with the ionic radius of the lanthanides and is in agreement with the reported literature [187, 188]. It can be seen that as the ionic radius increases, more superstructure peaks are formed in the XRD pattern and the crystal structure changes from cubic to orthorhombic. Thus Lu_3TaO_7 is indexed to a cubic defect fluorite (space group Fm-$3m$) structure; Y_3TaO_7 and Gd_3TaO_7 to an orthorhombic weberite type structure with space group C222$_1$, whereas La_3TaO_7 is matched to orthorhombic weberite structure belonging to centro - symmetric space group Cmcm. In order to establish the crystal structures correctly, Rietveld analysis of all the four XRD patterns were carried out and a detailed exploration of the lattice parameters, bond distances and other structural parameters were done. In all the cases, the Eu^{3+} ions are expected to occupy the Ln^{3+} sites considering the matching ionic radius and the valency. The ionic radius of different lanthanides is given in table 4.1. The starting models used for the refinement of the samples are given in tables 4.2, 4.3 and 4.4. Table 4.5 gives the refined parameters obtained from the Rietveld analysis. The

observed, calculated and the difference powder diffraction profiles of the samples $Ln_{2.85}TaO_7 : 0.15Eu^{3+}$ (Ln = La, Y, Gd, Lu) are given in figures 4.2 - 4.5. Selected bond distances of prepared samples are listed in table 4.6.
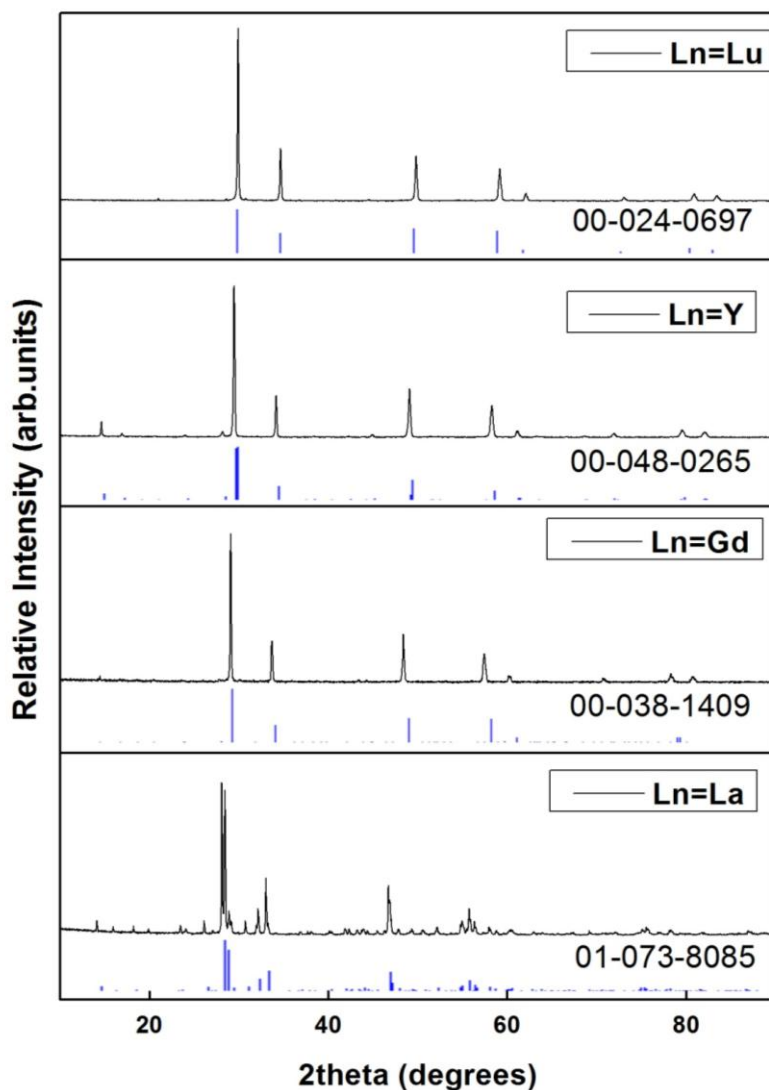
Figure 4.1 Powder X-ray diffraction patterns of $Ln_{2.85}TaO_7 : 0.15Eu^{3+}$ (Ln = La, Gd, Y, Lu) samples.

Table 4.1 Ionic radius and electronegativity of various ions.

Cation	Ionic radius (Å) (VII, VIII coordination)	Pauling's Electronegativity
La	1.1, 1.16	1.1
Gd	1, 1.05	1.2
Y	0.96, 1.01	1.22
Lu	-, 0.977	1.27
Eu	1.01, 1.06	1.2

Table 4. 2 Starting model of $Lu_{2.85}TaO_7 : 0.15Eu^{3+}$.

Element	Wyckoff	x	y	z	SOF
Lu	4a	0	0	0	0.7125
Eu	4a	0	0	0	0.0375
Ta	4a	0	0	0	0.25
O	8c	0.25	0.25	0.25	1

Table 4. 3 Starting model of $Gd/Y_{2.85}TaO_7 : 0.15Eu^{3+}$.

Element	Wyckoff	x	y	z	SOF
Gd/Y	4b	0	0.4954	0.25	0.85
Eu	4b	0	0.4954	0.25	0.15
Gd	8c	0.2338	0.2349	0.002	1
Ta	4b	0	-0.0005	0.25	1
O	8c	0.129	0.177	0.273	1
O	8c	0.116	0.794	0.281	1
O	4a	0.629	0	0	1
O	4a	0.365	0	0	1
O	4a	0.057	0	0	1

Table 4. 4 Starting model of $La_{2.85}TaO_7 : 0.15Eu^{3+}$.

Element	Wyckoff	x	y	z	SOF
La	8g	0.23	0.293	0.25	0.85
Eu	8g	0.23	0.293	0.25	0.15
La	4a	0	0	0	1
Ta	4b	0	0.5	0	1
O	16h	0.37	0.18	0.036	1
O	8g	0.139	0.028	0.25	1
O	4c	0	0.449	0.25	1

Table 4.5 Refined parameters of Rietveld analysis of $Ln_{2.85}TaO_7$:
$0.15Eu^{3+}$ (Ln = La, Gd, Y, Lu) samples.

Sample	Lu_3TaO_7	Y_3TaO_7	Gd_3TaO_7	La_3TaO_7
Crystal Structure	Cubic	Orthorhombic	Orthorhombic	Orthorhombic
Space group	*Fm-3m*	$C222_1$	$C222_1$	Cmcm
Flat background	78.9603	79.7645	125.8454	32.4037
Coefficient 1	-14.7300	-22.9696	-23.4959	-22.3178
Coefficient 2	9.6411	22.0857	22.4623	23.4707
Scale Factor	0.00017	0.00002	0.00001	0.00000
Lattice parameters				
a [Å]	5.1874(7)	10.4909(6)	10.6308(5)	11.1496(5)
b [Å]	5.1874(7)	7.4218(4)	7.5249(3)	7.6104(3)
c [Å]	5.1874(7)	7.4445(4)	7.5430(4)	7.7485(3)
Caglioti parameters				
U	0.0426	0.5512	0.1975	0.0413
V	-0.0044	-0.3126	-0.0939	-0.0038
W	0.0046	0.0572	0.0189	0.0035
Asymmetry parameter	0.8730	0.6352	0.4169	0
Peak Shape 1	0.4553	0.9501	0.8817	0.7805
Peak Shape 2	0.0055	-0.0091	-0.0082	0.0027
Residual parameters				
Rexp [%]	8.78	8.40	7.92	12.50
Rp [%]	9.45	9.29	6.76	14.50
Rwp [%]	11.79	12.83	8.70	19.50
GOF	1.80	2.33	1.20	2.40
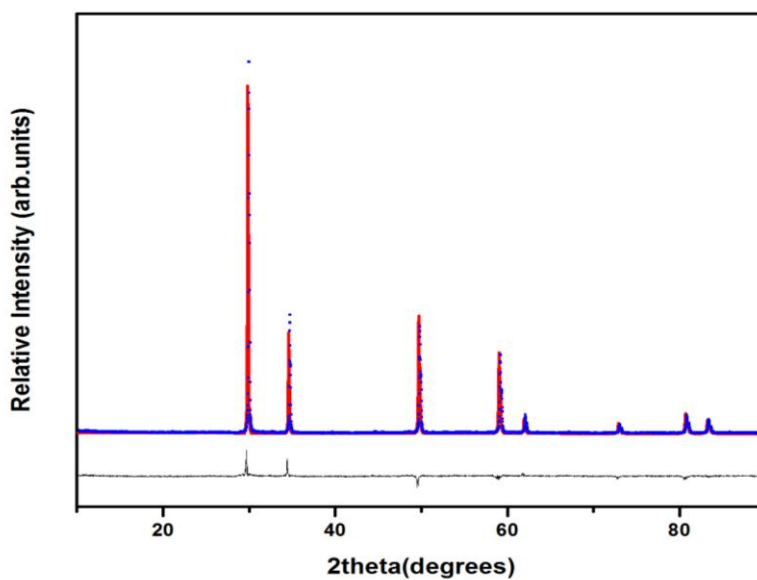
Figure 4.2 Observed (points), calculated (continuous line) and the difference $I_{obs}-I_{calc}$ (bottom line) XRD profiles of $Lu_{2.85}TaO_7$: $0.15Eu^{3+}$.
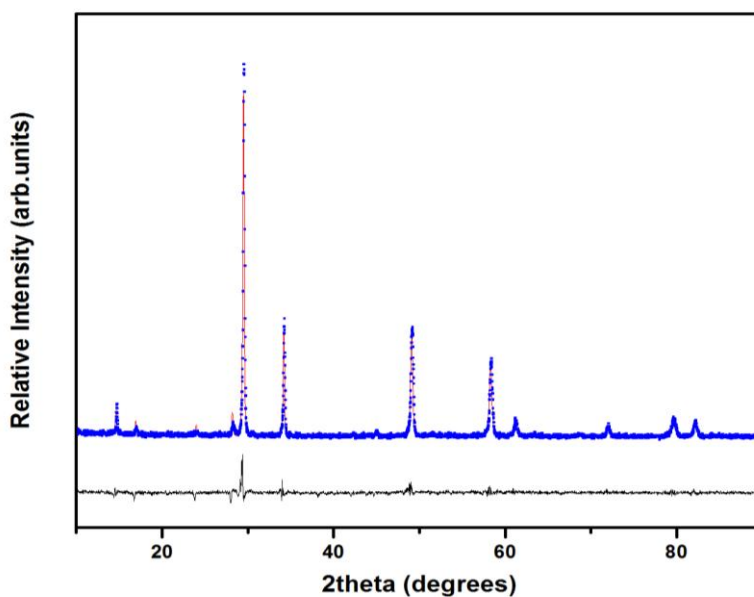
Figure 4.3 Observed (points), calculated (continuous line) and the difference $I_{obs} - I_{calc}$ (bottom line) XRD profiles of $Y_{2.85}TaO_7$: $0.15Eu^{3+}$.
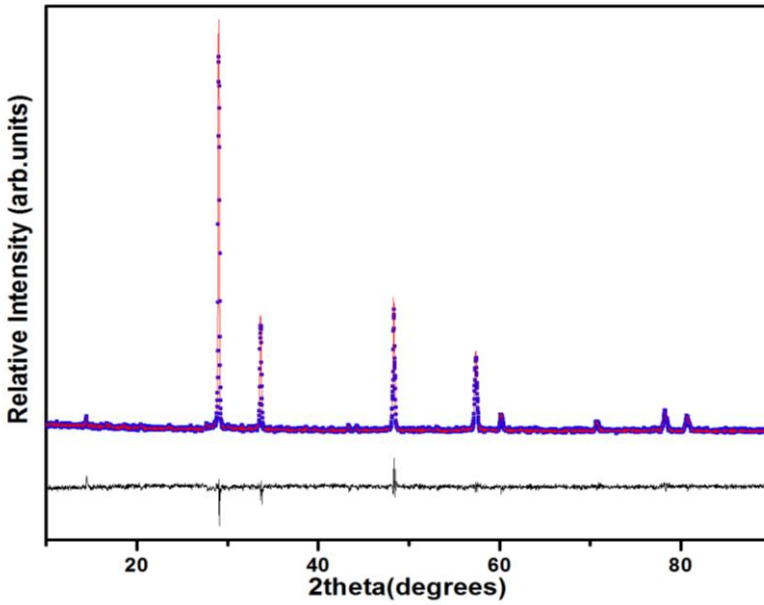
Figure 4.4 Observed (points), calculated (continuous line) and the difference $I_{obs} - I_{calc}$ (bottom line) XRD profiles of $Gd_{2.85}TaO_7 : 0.15Eu^{3+}$.
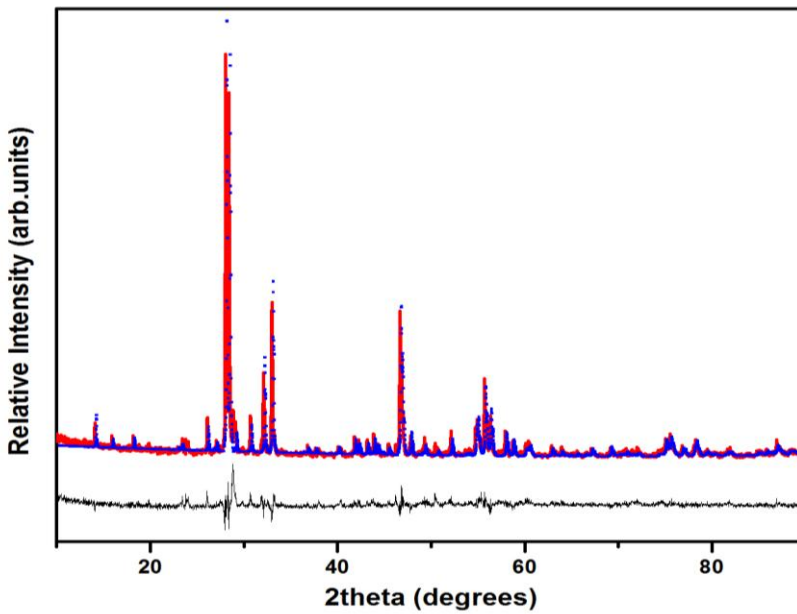
Figure 4.5 Observed (points), calculated (continuous line) and the difference $I_{obs} - I_{calc}$ (bottom line) XRD profiles of $La_{2.85}TaO_7 : 0.15Eu^{3+}$.

Table 4.6 Selected bond distances (in Å) of $Ln_{2.85}TaO_7$: $0.15Eu^{3+}$ (Ln = La, Gd, Y) samples.

	Ln = Y			Ln = Gd			Ln = La	
Y2	- O2	2.299	Gd2	- O2	2.327	La1	- O2	2.526
	- O1	2.325		- O1	2.358		- O2	2.526
	- O4	2.221		- O4	2.252		- O1	2.737
	- O2	2.452		- O2	2.487		- O3	2.167
	- O5	2.546		- O5	2.580		- O3	2.093
	- O1	2.337		- O1	2.366		- O2	2.590
	- O3	2.254		- O3	2.285		- O2	2.590
Y1	- O1	2.728	Gd1	- O1	2.766	La2	- O2	2.798
	- O3	2.301		- O3	2.332		- O2	2.798
	- O1	2.728		- O1	2.766		- O2	2.798
	- O4	2.339		- O4	2.370		- O2	2.798
	- O2	2.538		- O2	2.575		- O3	2.710
	- O3	2.301		- O3	2.332		- O3	2.710
	- O2	2.538		- O2	2.575		- O3	2.710
	- O4	2.339		- O4	2.370		- O3	2.710
Ta1	- O2	1.965	Ta1	- O1	1.922	Ta1	- O2	1.926
	- O5	1.955		- O5	1.981		- O2	1.926
	- O1	1.896		- O1	1.922		- O1	1.992
	- O1	1.896		- O1	1.922		- O1	1.992
	- O5	1.955		- O5	1.981		- O1	1.992
	- O2	1.965		- O2	1.991		- O1	1.992

The XRD analysis indicates that polymorphism exists in this family of compound $Ln_{2.85}TaO_7$: $0.15Eu^{3+}$ (Ln = La, Gd, Y, Lu) in agreement with the reported literature [173]. This type of polymorphism results from the degree of ordering of cations and oxygen

vacancy in the lattice from the fluorite form. As known, a single fluorite unit cell contains only one equivalent cation site and also one anion site, whereas in a weberite structure, there are three non-equivalent cation sites and three anion sites. Among the three cation sites, two (rare earths) are in VII/VIII coordination and the third one in VI coordination in an ordered BO_6 - AO_8 layer arrangement with anions largely shifted from the ideal tetrahedral site. Furthermore, a variation exists in the weberites of La_3TaO_7 in which a different layer of cation coordination (VII) lies between the layers of TaO_6 - LaO_8. These La - O bonds in the VII coordination are the shortest and the strongest La - O bonds of La_3TaO_7 (Table 4.6). The presence of more superstructure peaks and the number of non-equivalent cation sites structurally in La_3TaO_7 points out a long range order which has influenced greatly in the photoluminescence properties when compared to other systems as discussed in the later part of the text. In summary, the XRD analysis indicates a structural variation from a disordered cubic fluorite type structure to highly ordered orthorhombic weberite type structure with Lu to La substitution in this system.

FT-Raman spectra of the samples are given in figure 4.6 and it gives complementary information about structure as well as the vibrations of the atoms. We expect only a single Raman peak in the case of Lu_3TaO_7 system owing to its fluorite cubic crystal system. However an additional peak is observed in our case as observed by *Siqueira et al.* in the case of Lu_3NbO_7 which also identifies to a defect fluorite structure (*Fm-3m*) [139]. The presence of the additional peak was ascribed to the presence of lower symmetry structural domains immersed in the *Fm-3m* structure. In the case of weberite structures, it is known that the oxygen redistribution in the lattice leading to the formation of different polyhedra of different coordination can result in the presence or

absence of some modes. One of the important feature from the comparative study of the Raman spectra is the number of lines present. According to factor group theory predictions, in Cmcm and Ccmm type weberites about 27 Raman modes are expected ($8A_{1g}$ + $8B_{1g}$ + $5B_{2g}$ + $6B_{3g}$) and ($8A_{1g}$ + $8B_{1g}$ + $4B_{2g}$ + $7B_{3g}$) respectively whereas in $C222_1$ there are about 63 bands ($14A_{1g}$ + $18B_{1g}$ + $16B_{2g}$ + $15B_{3g}$) [138].
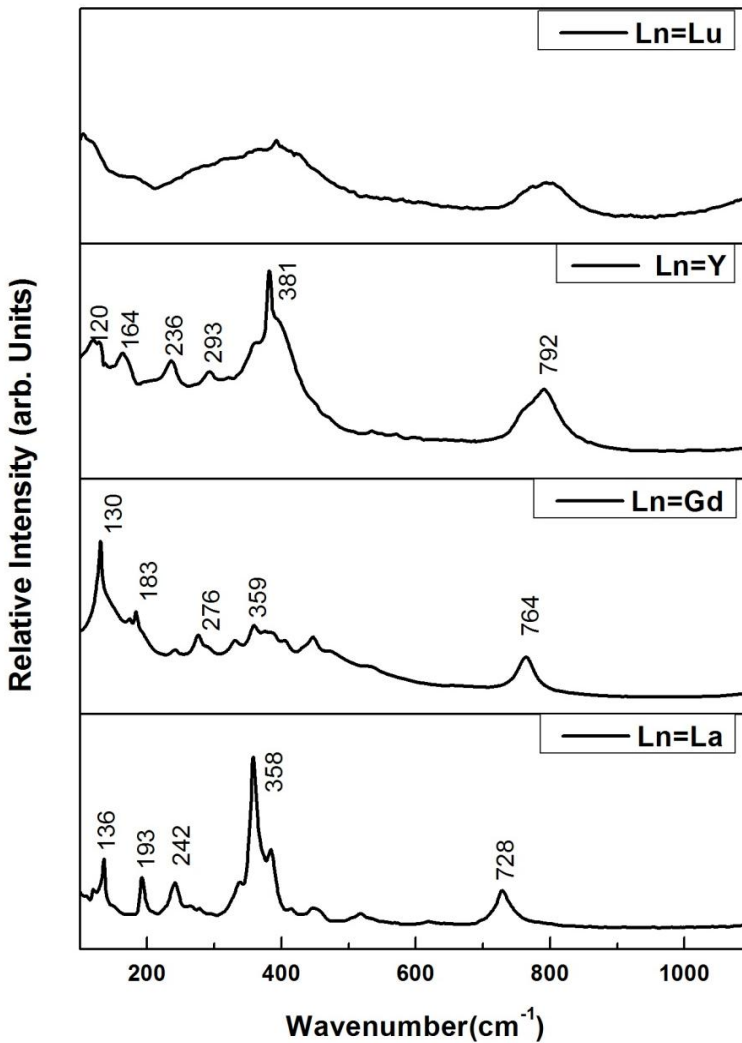
Figure 4.6 FT-Raman spectra of $Ln_{2.85}TaO_7$: $0.15Eu^{3+}$ (Ln = La, Gd, Y, Lu) samples.

Site symmetry is reduced in the non-centrosymmetric structure of Gd/Y_3TaO_7 ($C222_1$ space group), and the triply degenerate vibrations of the bonds are split and thus the spectrum of the compounds contains more lines than the spectrum of lanthanum which have centrosymmetric (Cmcm space group) structure. The presence of the A_{1g} line, mainly belonging to the collinear M - O - M bonds in MO_6 octahedra in the spectrum (728, 764, 792 cm^{-1} for Ln = La, Gd, Y respectively) points to one of the most specific features of a weberite structure [141]. It was also noticed that the wave numbers of the active bands presented a decreasing trend as the ionic radius of the lanthanide ion increases as a consequence of lanthanide induced lattice expansion. These results are consistent with the XRD analysis.

4.3.2 Morphological Studies

Morphology of the powder samples were also studied using scanning electron microscope and micrographs of the powder samples are given in figures 4.7. The SEM images indicates a uniform but slightly agglomerated particle morphology in the size range of about 0.5 - 3 μ. A decreasing trend in particle size could be observed from the lanthanide La to Lu. In order to understand the stoichiometric incorporation of the elements in the sample, energy dispersive spectra (EDS) were taken. The EDS analysis indicated the presence of all the expected elements and the obtained stoichiometric ratio was in close agreement with the theoretical formula. X-ray dot map studies further revealed the uniform distribution of Eu^{3+} ions in the host lattice and the dot mapped images of $La_{2.85}TaO_7 : 0.15Eu^{3+}$ sample are given in figure 4.8. EDS spectra of a representative sample $La_{2.85}TaO_7 : 0.15Eu^{3+}$ is presented in figure 4.9.
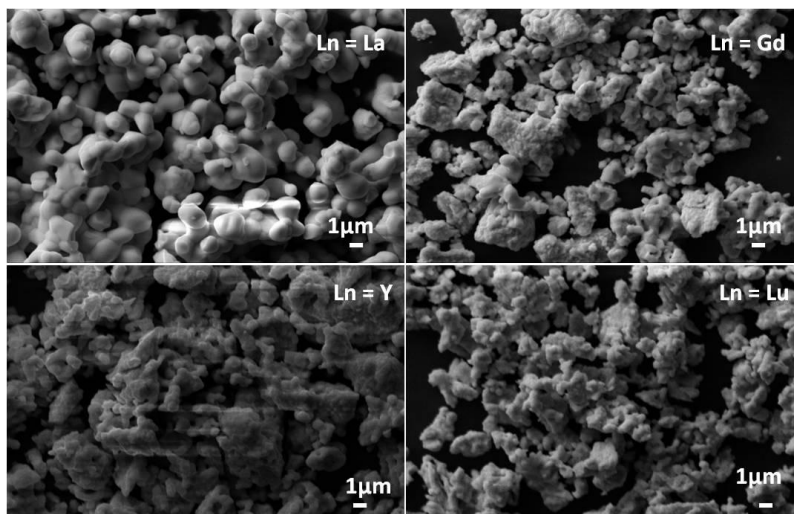
Figure 4.7 Scanning electron micrographs of Ln$_{2.85}$TaO$_7$: *0.15*Eu^{3+}
(Ln = La, Gd, Y, Lu).
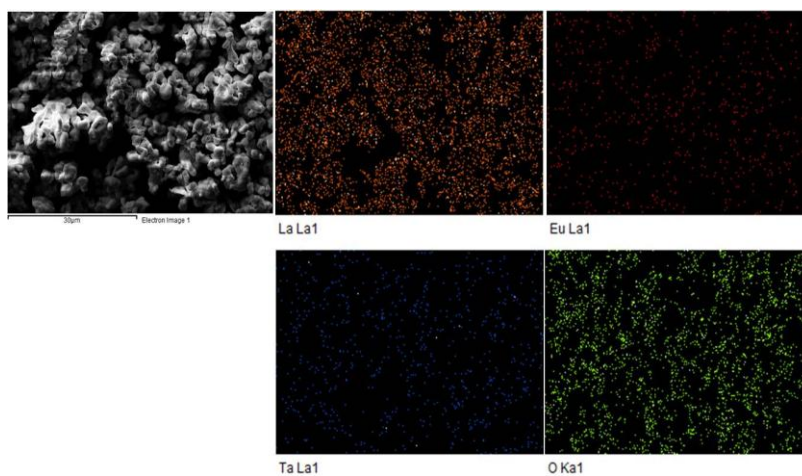
Figure 4.8 X-ray dot mapping of La, Eu, Ta and O in La$_{2.85}$TaO$_7$: *0.15*Eu^{3+}
sample.
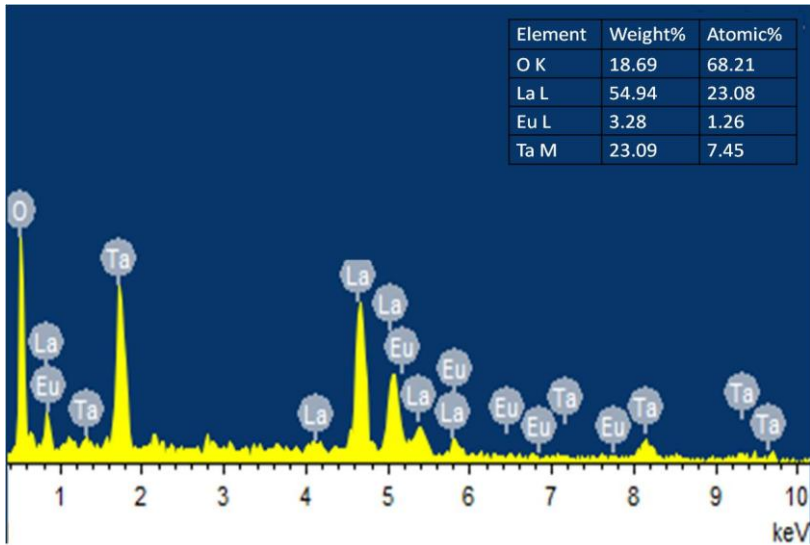
Figure 4.9 EDS spectra of La$_{2.85}$TaO$_7$: 0.15Eu^{3+} sample.

4.3.3 Optical and photoluminescence studies
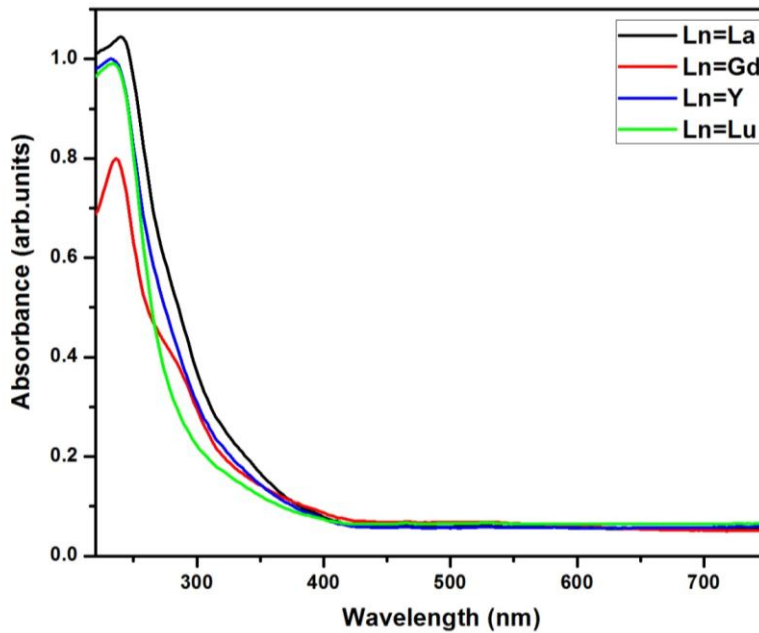
Figure 4.10 UV-visible absorption spectrum of Ln$_{2.85}$TaO$_7$: 0.15Eu^{3+}
(Ln = La, Gd, Y, Lu) samples.

UV-visible absorption spectra of the samples are presented in figure 4.10. All the samples exhibited good absorption in UV region which corresponds to the charge transfer transition from oxygen ligands to Eu^{3+} ions and to the central Ta atoms in the TaO_6 groups. The absorption edge shifted towards the higher wavelength as the lanthanoid switches through Lu to La and these results are consistent with the observation in the excitation spectra explained in the next section.

Figure 4.11 shows the photoluminescence excitation and emission spectra of $Ln_{2.85}TaO_7 : 0.15Eu^{3+}$ (Ln = La, Gd, Y, Lu) phosphors measured under the same experimental conditions. The excitation spectrum by monitoring the $^5D_0$ emission of Eu^{3+} ions consists of a broad band at 240 - 350 nm and some sharp lines from the characteristic intra-configurational 4f – 4f transitions mainly $^7F_0 \rightarrow {}^5L_6$ and $^7F_0 \rightarrow {}^5D_2$ transitions. The former broad absorption band is composed of the overlap between two Gaussians; due to the charge transfer transitions from $O^{2-} \rightarrow Eu^{3+}$ and the tantalate group [147]. The CTB maxima for La, Gd, Y, and Lu substituted compounds is listed in table 4.7. Considering the same charge transfer contribution from tantalate group, the shift of CTB maxima is noticed with the substitution of various lanthanides. Generally the CTB position of $O^{2-} \rightarrow Eu^{3+}$ lies in the wavelength region 230 nm taking into account of the optical electronegativities of O^{2-} and Eu^{3+} [189]. Moreover the CTB position is closely related to the coordination state of Eu^{3+} ions in the host lattice and the bond length of Eu^{3+} and anions. The band position is fixed in VI coordination and varies in VIII and IX coordination as a function of Eu -O bond distance in the lattice [190]. However there is not much literature for VII coordination. The position of CTB provides a clue of the coordination of Eu^{3+} ions in the lattice. The CTB position for Lu and Y hosts moves to

lower energy with increase of bond distances in VIII coordination as in the expected line (Table 4.7).
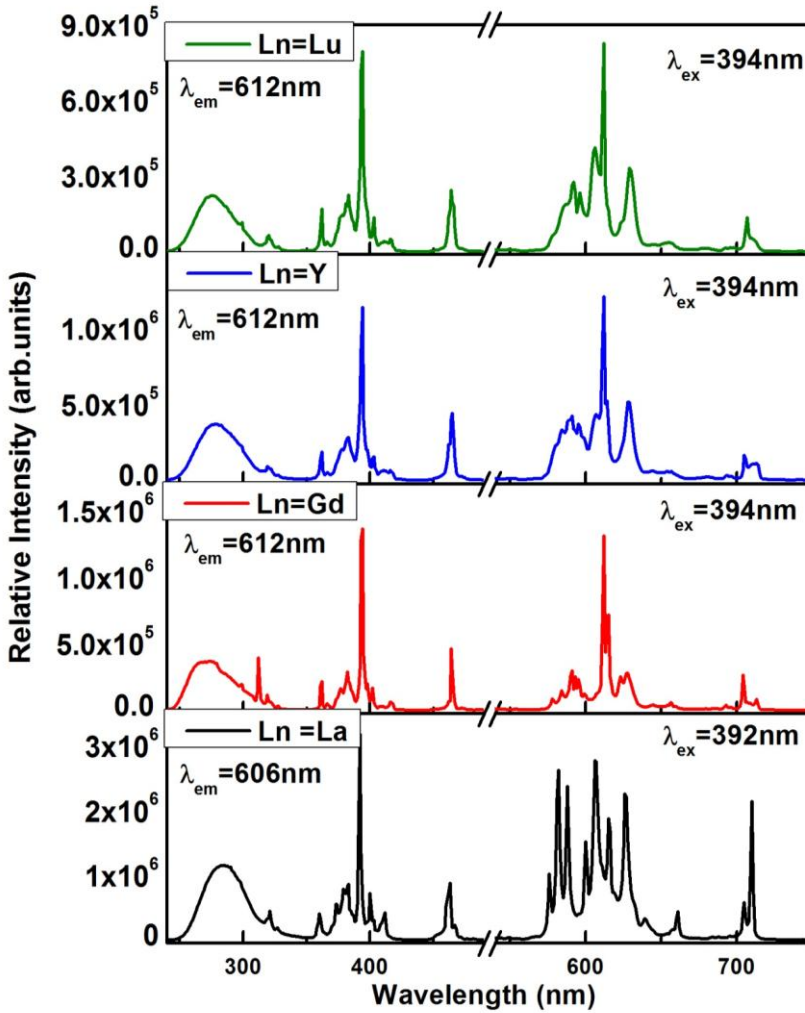
Figure 4.11 Photoluminescence excitation and emission spectrum of $Ln_{2.85}TaO_7 : 0.15Eu^{3+}$ (Ln = La, Gd, Y, Lu) samples.

Table 4.7 Luminescence characteristics and J - O intensity parameters of $Ln_{2.85}TaO_7 : 0.15Eu^{3+}$ (Ln = La, Gd, Y, Lu) samples.

Ln	CTB (nm)	A. R.	Lifetime (ms)	A_{rad} (ms^{-1})	A_{nrad} (ms^{-1})	Ω_2 (10^-20 cm^2)	Ω_4 (10^-20 cm^2)	η (%)
La	285	1.1	1.64	0.196	0.413	3.46	1.43	32.1
Gd	275	4.4	0.79	0.185	1.073	2.50	1.29	14.7
Y	279	3.6	0.99	0.145	0.857	1.75	0.76	14.5
Lu	275	2.9	0.807	0.169	1.069	2.35	0.72	13.7

However, the charge transfer energy in Gd host is relatively at a higher energy and does not follow the trend of CTB variation as a function of bond distance in the same coordination. Except the bond length, some other factors such as the covalency or ionicity, the potential field of the coordinate ions, the standard cation oxidation potential also influences the position of the CT band [191]. Some of these factors might have contributed to the increased charge transfer energy in the Gd host. Conversely, we suspect that the Eu^{3+} prefers to occupy in VII coordination in the La based host as the emission wavelength shift due to hypersensitive $^5D_0 \rightarrow {}^7F_2$ transition to red region on transforming Eu^{3+} ions to higher coordination VIII in the case of Y/Gd based hosts which is discussed in the later part of the text. Even though the CTB of La one is still at a lower energy due to increased contribution from the coordination rather than the bond length. This is further ascertained on comparison with other Eu^{3+} ions in VIII coordination hosts. It is observed that the present CTB is at a higher energy in relation to VIII coordinated hosts. This hints the presence of Eu^{3+} ion at a lower coordination than VIII and points out to be at VII

coordination as available in the host. In addition, Eu^{3+} occupancy based on the ionic size consideration was analyzed in different hosts. In the case of $Lu_{2.85}TaO_7$: *0.15*Eu^{3+} phosphors Eu^{3+} ions (ionic radius = 1.05) are occupying an VIII coordinated Lu^{3+} sites due to the matching ionic radius and valency. In the case of the weberite structures; $C222_1$ and Cmcm; there are VII, and VIII coordinated Ln^{3+} sites. Comparing the ionic radii of the lanthanoids (Table 4.1) Eu^{3+} ions are more likely to be substituted in the VIII coordinated sites in $Gd/Y_{2.85}TaO_7$: *0.15*Eu^{3+} phosphors whereas in a VII coordinated sites in $La_{2.85}TaO_7$: *0.15*Eu^{3+} phosphors. All the samples have efficient excitation intensity in UV and near UV wavelengths ($F_0 \rightarrow {}^5L_6$), which is very stronger than the absorption in the CT region. The intensity of the excitation peak due to ${}^7F_0 \rightarrow {}^5L_6$ transition is in the order La > Gd > Y > Lu. The excitation peak shifts to 392 nm in the case of $La_{2.85}TaO_7$: *0.15*Eu^{3+} phosphor whereas the peak comes at 394 nm in the other three samples. Owing to the intense excitation peaks in the UV region, the phosphor materials can be used with near ultraviolet (InGaN) chip for white LED applications.

It is well known that the selection rule and f - f transition probabilities between states depend strongly on the site occupation and the microstructure around Eu^{3+} ions in various hosts with different structures. The luminescence emission spectra details the variation in the emission intensities due to the transitions from the excited states ${}^5D_0$ to the ground states ${}^7F_J$ (J = 0, 1, 2, 3, 4) in different samples. As discussed above, change in CTB position and variation in the crystalline structure, the emission profile of these samples follows the same trend. The emission profile of La_3TaO_7 is quite distinct from the others. The ${}^5D_0 \rightarrow {}^7F_J$ (J = 0, 1, 2, 4) transitions are predominantly intense. The presence of single ${}^5D_0 \rightarrow {}^7F_0$ transition peak indicates single site occupancy of Eu^{3+} in the lattice and the peak is also located at a lower

wavelength (576 nm) [169]. This is generally observed around 580 nm. As known, the $^5D_0 \rightarrow{} ^7F_0$ transition of the Eu^{3+} ion is known to move to shorter wavelength with increasing ionic radius of the host cation, which is ascribed to the nephelauxetic effect [192]. This position shifts to higher wavelength (578 nm for Gd and 580 nm for Y) and also hints out the substitution of Eu^{3+} for the lanthanides. This particular transition is absent in the Lu substituted compound. The large blue-shift for La compound suggests a reduction in the coordination to VII. In addition, the $^5D_0 \rightarrow{} ^7F_0$ transition provides information on the bonding environment and coordination of Eu^{3+} ions as there is no crystal field splitting of the $^5D_0$ and $^7F_0$ levels. The line broadening of $^5D_0 \rightarrow{} ^7F_0$ transition is influenced by electron - phonon coupling and ion - ion interaction. As observed, a smaller bandwidth of this transition for La compound indicates a stiff bonding environment and uniform distribution of Eu^{3+} ions. Coming to other transitions, the $^5D_0 \rightarrow{} ^7F_J$ ($J =$ 1, 2, 4), for La host, three peaks were observed for the $^5D_0 \rightarrow{} ^7F_1$. The $^5D_0 \rightarrow{} ^7F_2$ transition presents four peaks. Unusual strong $^5D_0 \rightarrow{} ^7F_4$ transition is also observed. Similar emission spectra is observed in lanthanoid methanesulfonate $\{Ln(MS)_3\}$ [193]. Each lanthanoid is coordinated to seven methanesulfonate anions and the polyhedron around the lanthanoid is a distorted monocapped trigonal prism. The distortion is due to the repulsion between the anions due to steric requirements, thus producing small differences in the Ln - O bond distances. The suggested point group symmetry for the metal ion is C_{2v} which is in agreement with the point group selection rules [194]. The same emission profile and the small differences in the bond distances for La - O (Table 4.6) in VII coordination holds good in the present system. Therefore we could assume that the Eu^{3+} ion in the La_3TaO_7 may be in VII coordinated environment. It can be seen from the

spectrum that Eu^{3+} could obtain highly efficient luminescence in La_3TaO_7 Cmcm phase than that in Gd/Y_3TaO_7 $C222_1$ phase and in the Lu_3TaO_7 *Fm-3m* type structure. It can be seen that the orange emission due to the MD $^5D_0 \rightarrow {}^7F_1$ dominates in the La samples whereas the red emission due to the ED $^5D_0 \rightarrow {}^7F_2$ in other samples. This is clearly attributed to the centrosymmetric site occupancy of Eu^{3+} ions in the Cmcm space group structure. The transition from $^5D_0 \rightarrow {}^7F_4$ which is not so often seen was also observed in the case of $La_{2.85}TaO_7$: *0.15*Eu^{3+} phosphor. This transition is intense and different from the emission profiles of other lanthanide samples. The similar abnormal intense $^5D_0 \rightarrow {}^7F_4$ transition has been reported in Eu^{3+} doped $Na_9[EuW_{10}O_{36}]$, $LaBWO_6$, and $Y_3Al_{4-x}Ga_{1-x}O_{12}$ [195-197]. This abnormal intensity of $^5D_0 \rightarrow {}^7F_4$ transition in $LaBWO_6$ is mainly ascribed to a highly polarizable chemical environment with local symmetry corresponding to a distorted coordination polyhedron. The dependence of $^5D_0 \rightarrow {}^7F_4$ transition intensity in the garnet structure is mainly due to increased average EN values of M^{3+} ions which has counter ion effect on the Eu^{3+} environment. In the present system, the observed intense $^5D_0 \rightarrow {}^7F_4$ transition can be explained on account of both the reasons that are interrelated: polyhedron around the lanthanoid is a distorted monocapped trigonal prism due to the repulsion between the anions due to steric requirements in VII coordination and the lower electronegative value of La among the other lanthanides, Gd, Y, Lu (Table 4.1). In order to further assess the polarizability and Eu^{3+} environment, the Judd - Ofelt intensity parameters Ω_t (t = 2, 4) were calculated. In the theory of 4f - 4f transitions, the so called intensity parameters can be calculated using the equation

$$A_{0-\lambda} = (4e^2\omega^3/3\hbar c^3)\,(1/(2J+1))\,\chi \sum_\lambda \Omega_\lambda\,(\langle 5D0|U^{(\lambda)}|7FJ\rangle)^2 \qquad 4.1$$

where, $A_{0-\lambda}$ is the coefficient of spontaneous emission, e the electronic charge, ω the angular frequency of the transition, $\hbar$ Planck's constant over 2π, c the velocity of light, χ the Lorentz local field correction that is given by $n(n^2+2)^2/9$ with the refraction index n = 1.5 and $(\langle 5D0|U^{(\lambda)}|7FJ\rangle)^2$ values are the squared reduced matrix elements whose values are 0.0032 and 0.0023 for J = 2 and 4 respectively. From the individual transitions between the stark levels $^5D_0 \rightarrow \,^7F_2$ and $^5D_0 \rightarrow \,^7F_4$, Judd - Ofelt intensity parameters Ω_2 and Ω_4 can be calculated and are given in table 4.7. Ω_6 values were not determined as $^5D_0 \rightarrow \,^7F_6$ transition could not be experimentally determined. These intensity parameters provide the radiative probabilities of the activator ions in different hosts. Ω_2 provides the information on the Eu - O covalency and asymmetry behavior of the activator and the ligand, whereas the other parameters depend on the long range effects. Comparatively, higher values of Ω_2 for La host suggest the strong covalent nature of the Eu^{3+} bonding with the surroundings [199]. Further, as coordination number decreases, the bonding becomes more directional and covalency increases. It is pointed out that the electron covalency contributes polarizability as strong on-site Coulomb repulsion between electrons is included, the electronic system is found to undergo a transition between the ionic and Mott insulating phases, and the covalency contributions to the polarizability are largely enhanced near the phase boundary [200]. The observed Ω_2 for La host is the highest among the studied. In general, the order of Ω_t parameters is $\Omega_2 < \Omega_4$, but the trends in the present system is $\Omega_2 > \Omega_4$. This trend of intensity parameters is in agreement with those reported in the literature [201]. This trend confirms the covalency existing between the Eu^{3+} ions and ligands as

well as the asymmetry around the metal ion site. The emission intensity could also be characterized by Ω_4 parameters. This value increases from Lu to La and shows maximum for La suggesting increased efficiency for the $^5D_0 \rightarrow {}^7F_2$ transition. The evaluation of J - O intensity parameters suggests the increased polarizability and efficiency from Lu to La and these results are consistent with the observed PL results.

The fluorescence decay curves for $^5D_0$ states in $Ln_{2.85}TaO_7 : 0.15Eu^{3+}$ (Ln = La, Gd, Y, Lu) under near UV excitation are shown in figure 4.12. All the decay curves could be fitted well using the single exponential function;

$$I = A \exp (-x/\tau) \qquad 4.2$$

where I, τ and A are intensity, decay time and fitting parameter respectively. This shows the single site occupancy of luminescent Eu^{3+} ions.
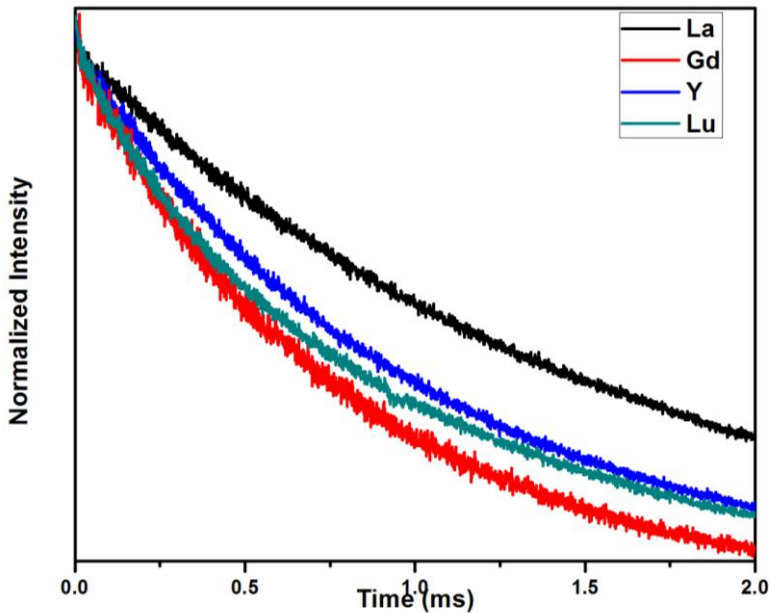
Figure 4.12 Decay curves of Eu^{3+} emission in $Ln_{2.85}TaO_7 : 0.15Eu^{3+}$ (Ln = La, Gd, Y, Lu) samples.

Assuming that only radiative and non-radiative processes are essentially involved in the depopulation of $^5D_0$ states of Eu^{3+} ion, the quantum efficiency (η) can be expressed as;

$$\eta = A_{rad}/(A_{rad} + A_{nrad}) \qquad 4.3$$

where A_{rad} and A_{nrad} are radiative and non-radiative transition probabilities respectively. The emission intensity (I) can be taken as the integrated (S) of $^5D_0 \rightarrow {}^7F_{0-4}$ emission curves as;

$$I_{i-j} = \hbar\, \omega_{i-j}\, A_{i-j}\, N_i \sim S_{i-j} \qquad 4.4$$

where i and j are initial ($^5D_0$) and final ($^7F_{0-4}$) levels respectively; $\hbar\omega_{i-j}$ is the transition energy, A_{i-j} is the Einstein's coefficients of spontaneous emission and N_i the population of $^5D_0$ emitting level. The experimental coefficient of spontaneous emission (A_{0j}) can be calculated based on the relation

$$A_{oj} = A_{o1}\,(I_{oj}/\,I_{o1})\,(\upsilon_{01}/\,\upsilon_{0j} \qquad 4.5$$

υ_{01} and υ_{0j} are the energy baricenters of the $^5D_0 \rightarrow {}^7F_1$ and $^5D_0 \rightarrow {}^7F_j$ energy levels determined from the emission peaks of Eu^{3+} ion. A_{01} is the Einstein's coefficients of spontaneous emission between $^5D_0$ and $^7F_1$ energy levels given as.

$$A_{0-1} = n^3(A_{0-1})vac \sim 50s^{-1} \qquad 4.6$$

where n, average refractive index 1.506 and (A_{0-1}) vac = 14.65 s^{-1}

The lifetime (τ) of the $^5D_0$ states, A_{rad}, A_{nrad} are related as ;

$$A_{tot} = 1/\tau = A_{rad} + A_{nrad} \qquad 4.7$$

Quantum efficiency of the samples was calculated using the equations 4.3 - 4.7 [202 - 206]. Lifetime values and efficiencies of the phosphors are given in table 4.7. Variation of the emission intensity and the quantum efficiency with respect to the ionic radius of the lanthanides is presented in figure 4.13.
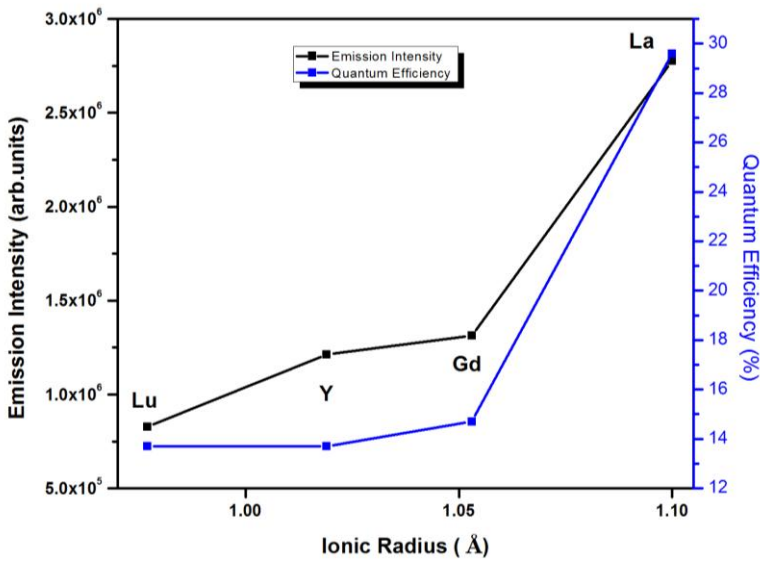
Figure 4.13 Variation of emission intensity and the quantum efficiency with respect to the ionic radius in $Ln_{2.85}TaO_7 : 0.15Eu^{3+}$ (Ln = La, Gd, Y, Lu) samples.

The Eu^{3+} luminescence is very sensitive to the symmetry in the lattice and is used as a structural probe in many systems. The asymmetry ratio ($^5D_0 \rightarrow {}^7F_2 / {}^5D_0 \rightarrow {}^7F_1$) provides a clue on the changes in the inversion symmetry in the lattice. The asymmetry ratio increases abruptly from La (1.1) to Gd (4.4) or Y (3.6) sample (Table 4.7). These results suggest that non-centrosymmetric SG assignment for Gd or Y is in agreement with the structural analysis. It can be seen that the photoluminescence properties among the prepared phosphor materials were better in the system in which Ln cation has the highest ionic radius. This is attributed to the structural variation in the crystal lattices by varying the Ln cations. It can be understood that the orthorhombic Cmcm structure offers better site occupation for Eu^{3+} for f - f transitions leading to red and orange - red emissions than the orthorhombic $C222_1$ and cubic structures. The CIE color coordinates of

the four samples were calculated and was found to be (0.57, 0.39), (0.58, 0.34), (0.58, 0.35) and (0.57, 0.35) for La, Gd, Y and Lu samples respectively.

4.3.4 Phase evolution on Eu^{3+} doping in La$_3$TaO$_7$ host lattice

Powder X-ray diffraction patterns of La$_{3-x}$TaO$_7$: xEu^{3+} (x = 0.15, 0.45, 0.9, 1.05, 1.2 and 1.35) are given in figure 4.14. The number and intensity of super lattice reflections decreases with the increasing substitution of Eu^{3+} ions. This implies a gradual variation in the crystal structure on increasing doping concentration. The XRD patterns can be matched well to ICDD ref no. 00-048-0265 corresponding to C222$_1$ phase for the samples above a doping concentration of x = 1.05. The crystal structure changed from orthorhombic Cmcm phase to C222$_1$ phase.
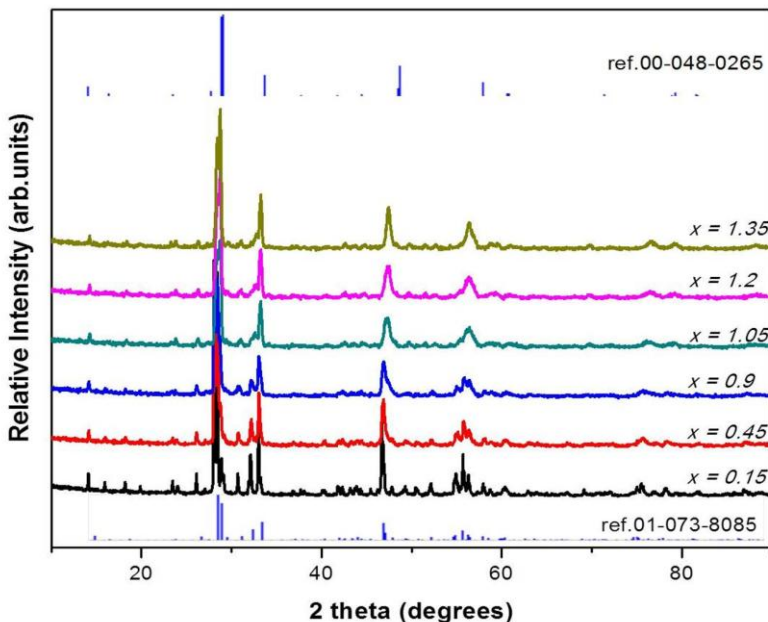
Figure 4.14 Powder X-ray diffraction patterns of La$_{3-x}$TaO$_7$: xEu^{3+} (x = 0.15, 0.45, 0.9, 1.05, 1.2, 1.35) samples.
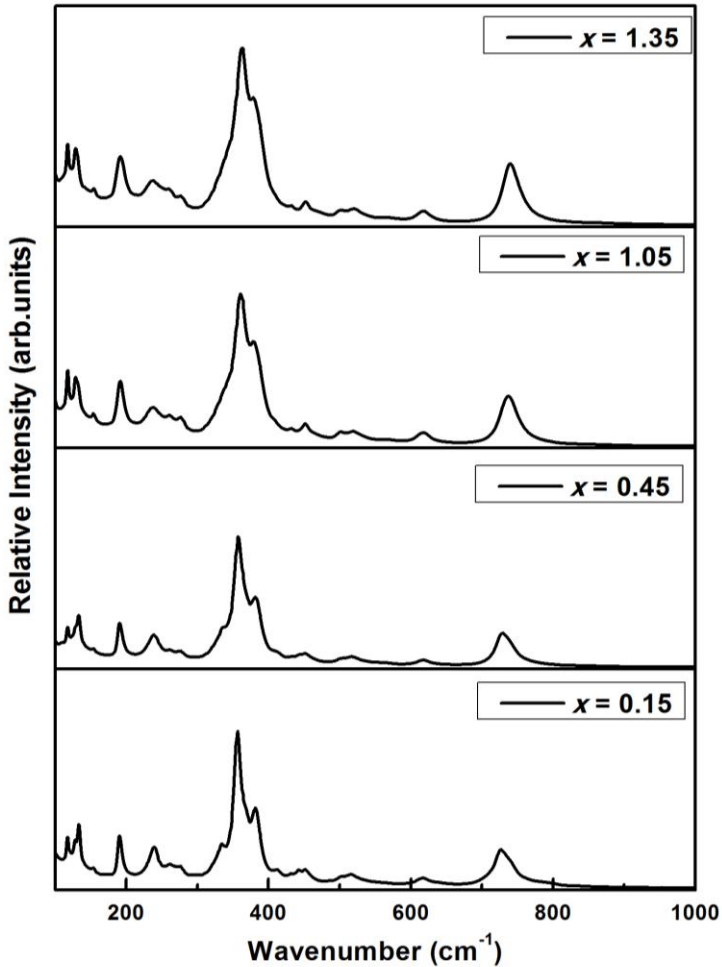
Figure 4.15 FT-Raman spectra of $La_{3-x}TaO_7 : xEu^{3+}$ (x = 0.15, 0.45, 1.05 and 1.35) samples.

To ascertain the phase evolution, Raman spectra of the representative samples were also taken and shown in figure 4.15. The features of the spectra are similar with some variations in the *fwhm* and shifting of the modes. The Raman mode at 380 cm⁻¹ which is a signature of the orthorhombic Cmcm structure gets broader as the Eu^{3+} substitution increases suggesting increasing disorder in the lattice associated with the phase evolution. The other characteristic stretching

motion of Ta - O bond observed at 725 cm^{-1} shifts to higher frequencies with increased intensity. This further characterizes Eu^{3+} substitution in the whole range. It is further noticed that the red-shift of all the modes in the spectra is significant at the phase evolution for $x = 1.05$. The complex group of modes between 100 and 400 cm^{-1} becomes broader which could be probably linked to the structural phase transition from orthorhombic Cmcm phase to C222$_1$ phase. The Raman results are consistent with the XRD results. The phase evolution on Eu^{3+} doping in La$_3$TaO$_7$ host lattice as confirmed from the XRD and Raman spectral analysis was also reflected in the photoluminescence spectra of these compounds. Photoluminescence excitation and emission spectra of the samples are given in figures 4.16 and 4.17 respectively.
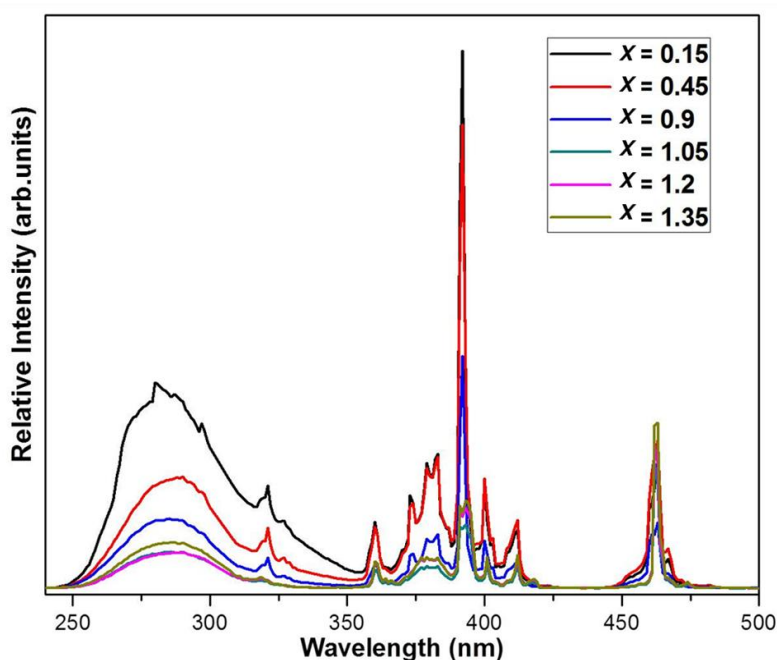
Figure 4.16 Photoluminescence excitation spectra of La$_{3-x}$TaO$_7$: xEu^{3+} ($x =$ 0.15, 0.45, 0.9, 1.05, 1.2, 1.35) samples.
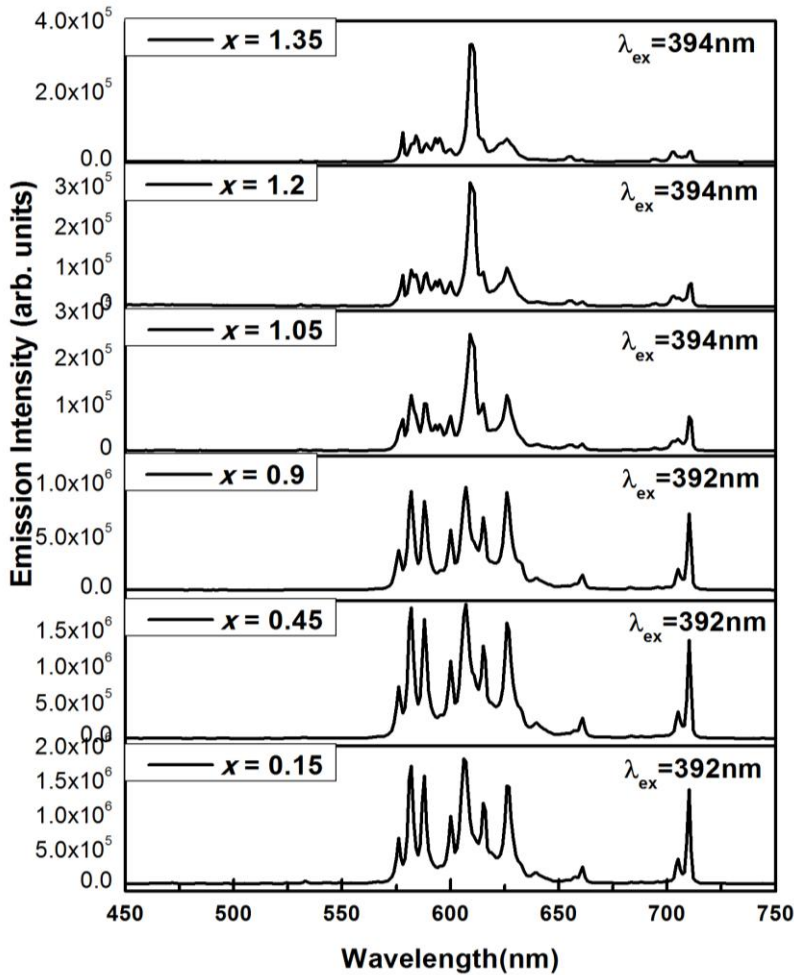
Figure 4.17 Photoluminescence emission spectra of $La_{3-x}TaO_7 : xEu^{3+}$ ($x =$ 0.15, 0.45, 0.9, 1.05, 1.2, 1.35) samples.

It can be noticed that the emission profiles are different for the Cmcm and C222$_1$ phase. As the structure changed from Cmcm to C222$_1$ space group the multiband emission $^5D_0 \rightarrow ^7F_{0,1,2,4}$ changed to dominant red emission due to hypersensitive ED transition $^5D_0 \rightarrow ^7F_2$ improving significantly the asymmetric ratio. It is noticed that this transition maxima is red-shifted from 606 nm to 612 nm on this structural

variation. Also in Eu^{3+} doped La_3TaO_7 the dominated emission transition of $^5D_0 \rightarrow {}^7F_4$ at 710 nm becomes weaker as the Eu^{3+} doping increased. This indicates that the emission transition of $^5D_0 \rightarrow {}^7F_4$ can be observed in the Cmcm orthorhombic crystal phase of La compound only. However it was also observed that the excitation and the emission intensities decreases as the Eu^{3+} doping concentration was increased. Thus the optimum doping concentration of Eu^{3+} ions in the La_3TaO_7 host lattice was found to be at $x = 0.15$.
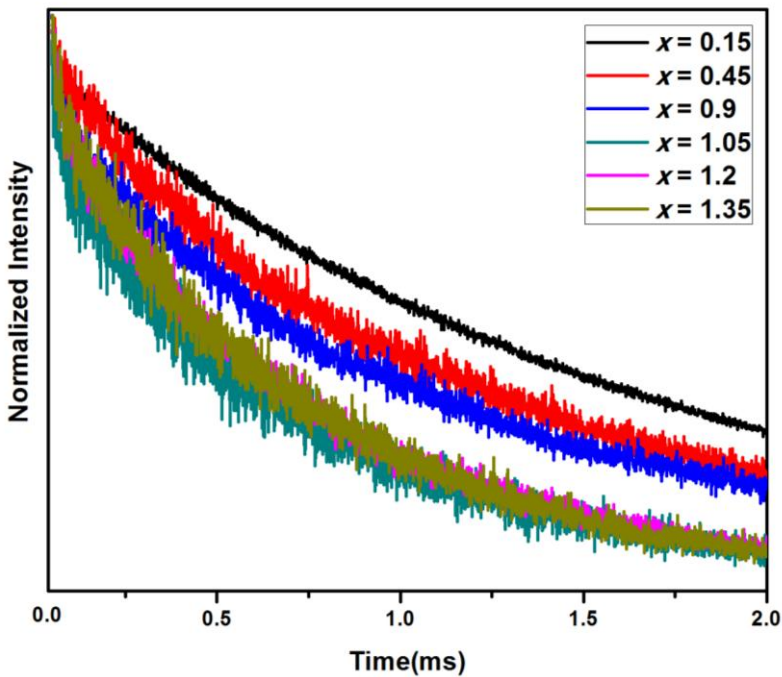
Figure 4.18 Decay curves of Eu^{3+} emission in $La_{3-x}TaO_7 : xEu^{3+}$ ($x = 0.15$, 0.45, 0.9, 1.05, 1.2 and 1.35) samples.

Decay curves of the samples are given in figure 4.18. The lifetime shows a decreasing trend (1.64, 0.94, 0.85, 0.62, 0.65, 0.65 ms) with Eu^{3+} substitution and abrupt change in the lifetime at the phase boundary composition further confirming the phase transition. The

higher lifetime values for the Eu^{3+} substitution below $x = 1.05$ indicates preferential distribution of Eu^{3+} ions in the VII coordination and the decreasing trend is on account of concentration quenching. In general, concentration quenching is mainly observed as a result of reduction in the distance between ions less than the critical value in the host lattices. On higher substitutions, Eu^{3+} - Eu^{3+} distance decreases leading to effective energy transfer between the neighboring ions due to cross relaxation. On the other hand the sudden drop in the lifetime above $x = 1.05$ hints to a structural transition as discussed above. The Eu^{3+} preferential occupancy in VII coordinated site in $C222_1$ SG type structure is absent which leads to formation of Eu^{3+} - Eu^{3+} clusters. As a result the lifetime abruptly decreases in the $C222_1$ lattice.

The Eu^{3+} luminescence in this system affords a sensitive indication of structural variation because its energy levels are highly responsive to crystal symmetry variations. Luminescence is mainly influenced by the crystallographic structure including the coordination of the activator and its surroundings and the ordering of the activator in the lattice. The present system offered ample scope to understand the influence of long range order and coordination of cations on the photoluminescence properties of Eu^{3+} ion activated Ln_3TaO_7 system. The above PL properties greatly signify the minor structural variation of these closely related structures in Ln_3TaO_7 system. The variation in the long range ordering and coordination of cations and anion polarizabilty of cations are some of the main factors for contributing the better luminescence in La_3TaO_7 system. The first two factors are associated with the crystalline structure and the third one is due to nature of the chemical environment constituting the bond formation. The XRD and Raman structural studies points out a structural variation from a highly disordered lattice of defect fluorite for Lu_3TaO_7 to

ordered orthorhombic weberite type structures for other lanthanoides (Y, Gd and La). The degree of ordering of cations is Lu < Y < Gd < La which aids for uniform distribution of Eu^{3+} ions and prevents cluster formation of Eu^{3+} - Eu^{3+} in the lattice. This is further characterized by the $^5D_0$ lifetime and the values follow the same trend of ordering of the lattice. This allows more partition of Eu^{3+} ions in the lattice avoiding the cross relaxation between the Eu^{3+} ions enhancing the luminescence. The phase evolution in higher doping of Eu^{3+} ions in La_3TaO_7 further supplements the influence of the long range ordering and coordination of cations on the luminescence properties. The redshift of hyper sensitive transition due to electric dipole $^5D_0 \rightarrow {}^7F_2$ transition is associated with the variation of Eu^{3+} coordination from VII to VIII coupled with the phase evolution. The increased Eu^{3+} transition probabilities can be connected with the polarization of the electron density around the O^{2-} anions towards or away from the Eu^{3+} ion. In general the crystal dependent anion (O^{2-}) polarizability can be associated with the ionic radii of the host cation and its electronegativity. The anion polarizability decreases when the anion is bonded to cations that are small and highly charged. Also, as can be expected the anion polarizability decreases with increasing electronegativity of the coordinating cations. Considering the Pauling's electronegativity values and ionic radii, we can expect the anion polarizability to be highest in La_3TaO_7 and the least in Lu_3TaO_7. Consequently the anion poloarizability is expected to vary as La > Gd > Y > Lu. Thus the oxygen electron density is more tightly bonded by the Lu^{3+} ions in Lu_3TaO_7 than by the La^{3+} ions in La_3TaO_7. In another way, the larger and least electronegative La^{3+} ions are less able to attract the O^{2-} electron density towards them relative to the smaller and most electronegative Lu^{3+} ion. As a result, when Eu^{3+} ion is incorporated in

these materials, the shift of the center of electron density around O^{2-} ion will be highest in La_3TaO_7 and the least in Lu_3TaO_7 due to the inductive effect. Therefore, the distance between the Eu^{3+} ion and center of electron density on the O^{2-} ion will be least in La_3TaO_7 and the highest in Lu_3TaO_7. As the splitting and probabilities of ^7F_J transitions decreases on going from La_3TaO_7 to Lu_3TaO_7, it is reasonable to associate the observed trend of increased probabilities and splitting of ^7F_J transitions to significant contributions of covalency/ligand polarization to the crystal field, which is the highest in La_3TaO_7 and the least in Lu_3TaO_7. Thus the long range ordering and coordination of cations and ligand polarizability are primarily responsible to influence on the emission probabilities and intensity and quantum efficiency of these phosphor materials.

4.4 Conclusions

Ternary lanthanide - tantalum oxides, Ln_3TaO_7 (Ln = La, Gd, Y, Lu) have been prepared and their structural and photoluminescence properties have been studied. The crystal structures of Ln_3TaO_7 changed from cubic to orthorhombic superstructures with increasing ionic radius. The variation of ionic size induced ordering of cations Lu < Y < Gd < La in the lattice. The increasing trend of luminescence lifetime from Lu to La corroborated the degree of ordering in the lattice. An unusual photoluminescence of almost equally competing intensities from all the 4f transitions of the Eu^{3+} ($^5D_0 \rightarrow {}^7F_{0,1,2,4}$) was noticed for La_3TaO_7 system. This was explained on the basis of the higher polarizability and covalent nature of Eu^{3+} ion bonding environment which prevailed in the VII coordination in the orthorhombic Cmcm structure in comparison with other systems. The higher concentration of Eu^{3+} doping in La_3TaO_7 led phase evolution in the structure from

Cmcm to $C222_1$ space group. The Eu^{3+} luminescence in this system corroborated the variation of VII to VIII coordination environment through intense $^5D_0 \rightarrow {}^7F_{0,1,2,4}$ transitions to only dominant hypersensitive ED $^5D_0 \rightarrow {}^7F_2$ transition shifting to red. These results demonstrate that the long range ordering and coordination of cations and ligand polarizability influenced significantly on the emission probabilities and intensity and quantum efficiency of these phosphor materials.

5

ENHANCEMENT IN THE PHOTOLUMINESCENCE PROPERTIES OF La_3TaO_7 : Eu^{3+} RED PHOSPHORS THROUGH CATIONIC MODIFICATION

_____

The influence of Ba^{2+} substitution in Ln^{3+} site on the photoluminescence properties of La_3TaO_7 : Eu^{3+} red phosphors was studied and a further improvement could be achieved by compositional variation. Ba^{2+} ions were introduced with a view to increase the polarizability around the Eu^{3+} ion and for improving the ordering in the host lattice. The trend in the photoluminescence properties with respect to Ba^{2+} substitution was analyzed and the influencing parameters were well studied.
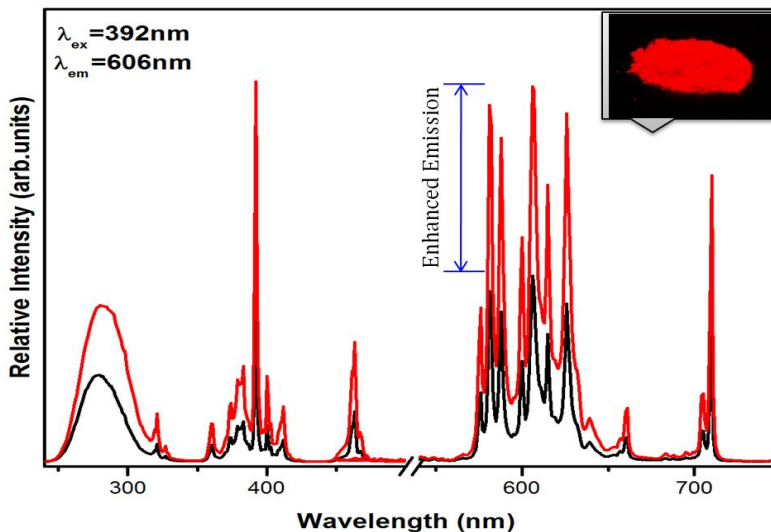
5.1 Introduction

White light emitting diodes are considered to be the next generation lighting device overruling other conventional light sources. Phosphor materials showing high luminescence are indispensible part in this technology. Phosphors have attracted worldwide interest from theoretical, experimental and industrial view points. Eu^{3+} doped ternary lanthanide red phosphors of general formula Ln_3MO_7 (Ln = La, Gd, Y, Lu; M = Nb, Sb, Ta) gains much attraction as it provides ample scope towards the understanding of the various influencing factors on the photoluminescence properties of Eu^{3+} ions. When the Ln and M cations are substituted by La and Ta ions respectively, Eu^{3+} ions exhibits intense orange red emission properties. As already discussed in chapter four, Eu^{3+} activated La_3TaO_7 is a potential candidate to be used as a red phosphor in pc-WLED lighting industry. However further improvement in the emission properties could be achieved by the modification in the host lattice. The substitution of cations in a phosphor with bigger or smaller ions is generally considered to create distortion around Eu^{3+} surrounding which is an effective way to tune various luminescence properties like the color coordinates, emission intensity etc [207].

It was already observed that the ordering in the lattice increases as the ionic radius of the Ln^{3+} cation increases. Thus the incorporation of a larger cation in the Ln^{3+} site may result in the increased ordering in the lattice. Along with the increasing ionic radius, the addition of the cation should not disrupt the crystal phase formation of the lattice. The larger ionic radius and highly polarizable nature of Ba^{2+} may help to improve the emission properties of Eu^{3+} in La_3TaO_7 host. However the substitution of a divalent cation in place of a

trivalent cation may cause oxygen vacancies in the lattice so as to maintain the charge neutrality.

Thus we attempted to introduce Ba^{2+} ions in place of the Ln^{3+} ions in La_3TaO_7 host. In this chapter, the luminescence properties of a series of $La_{2.85-y}TaO_7 : 0.15Eu^{3+}, yBa^{2+}$ phosphors are explained and the variation in the properties when Ba^{2+} was substituted to the La^{3+} site is discussed. Eu^{3+} concentration was fixed to be x = 0.15 (concentration quenching point) in all the compositions.

5.2 Experimental section

5.2.1 Synthesis

The powder samples in the present study were prepared by a high temperature solid state reaction route. Chemicals La_2O_3, Ta_2O_5, $BaCO_3$, Eu_2O_3 from Sigma Aldrich with 99.99% purity were used as the starting materials for preparing $La_{2.85-y}TaO_7 : 0.15Eu^{3+}, yBa^{2+}$ phosphors. Stoichiometrically weighed individual powders were mixed, finely ground and made into a homogeneous mixture using an agate mortar and pestle in an acetone medium with intermittent drying. This powdered mixture was made into a pellet and then calcined on an alumina plate at 1400°C for 6 hours. Calcination was repeated at the same temperature and time, powdering and pelletizing after the first calcination. The properties of the phosphors thus prepared are studied using different characterization tools.

5.2.2 Characterization

The crystalline structure of the samples was examined with an X-ray powder diffractometer (X'Pert Pro PANalytical, operated at 40 kV and 30 mA, Cu - Kα = 1.5406 Å, 2θ range = 10° - 90°). Morphological studies of powder particles were done by a scanning electron

microscope (JEOL, JSM - 5600LV) operated at 15 kV. EDS spectra was recorded to identify the elements present. X-ray dot mapped images were also recorded. Absorbance study of the samples were carried out using a Shimadzu, UV - 2450 UV-vis spectrophotometer in the 400 –700 nm wavelength range using barium sulfate as a reference. The excitation and emission spectra were recorded on a Fluorolog HORIBA fluorescence spectrophotometer with a Xenon lamp (450 W) as the excitation source. Luminescence lifetime of the phosphors was recorded by the phosphorimeter attached to Fluorolog®3 spectrofluorimeter. CIE color coordinates of the samples were calculated using the Calc software.

5.3 Results and discussion

5.3.1 Structural studies
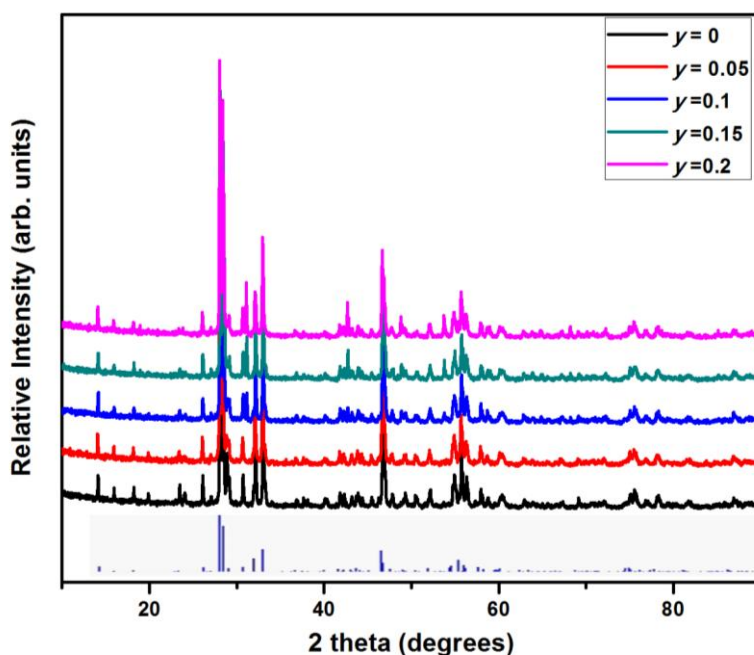
Figure 5.1 Powder X-ray diffraction patterns of La$_{2.85-y}$TaO$_7$: 0.15Eu^{3+}, yBa^{2+} (y = 0.05, 0.1, 0.15, 0.2).

Powder X-ray diffraction pattern of $La_{2.85-y}TaO_7 : 0.15Eu^{3+}, yBa^{2+}$ (y = 0.05, 0.1, 0.15, 0.2) phosphor samples were recorded and are presented in figure 5.1. All peaks could be correctly indexed to the powder diffraction pattern of an orthorhombic structure with a space group Cmcm similar to the powder diffraction pattern of La_3TaO_7 (ICDD ref no. 01-073-8085). Comparing the ionic radii of Ba^{2+} and Eu^{3+} ions with respect to La^{3+} and Ta^{5+} ions, both of them are expected to occupy the La^{3+} sites rather than the smaller Ta^{5+}.
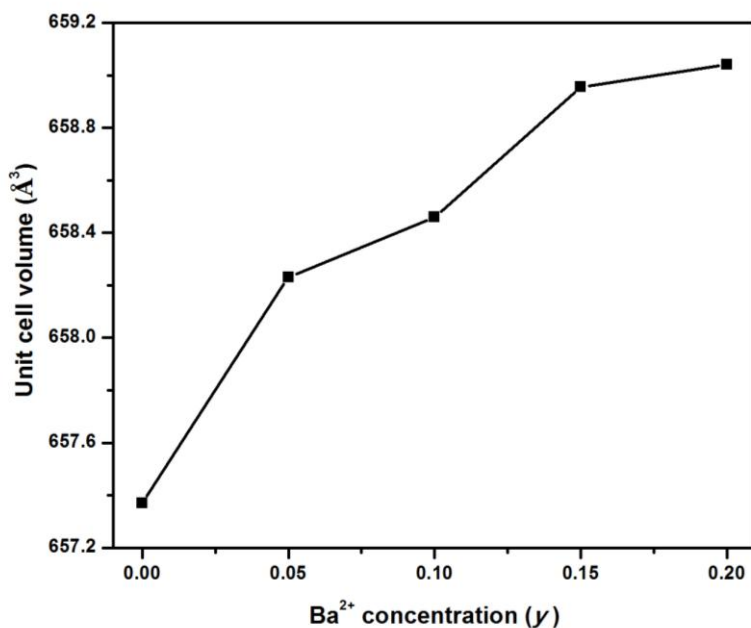
Figure 5.2 Variation of unit cell volume in $La_{2.85-y}TaO_7 : 0.15Eu^{3+}, yBa^{2+}$ with Ba^{2+} substitution.

The variation in the unit cell volume with increasing concentration of Ba^{2+} in the lattice is given in figure 5.2. Lattice cell volume of the prepared samples followed an increasing trend with Ba^{2+}

incorporation accounting its higher ionic size than La^{3+} ions. However a secondary phase was developed and some minor impurity peaks could be indexed beyond a substitution level of $y = 0.15$ concentration. The additional peaks could be indexed to that of barium oxide (BaO) formed in the compound. Thus further substitution was not carried out. The crystal structures of the samples were drawn using diamond software and a representation ($x = 0.1$) is given in figure 5.3. Ba^{2+} ions can go to any of the La^{3+} site forming either BaO_7 or BaO_8 polyhedra. Bond lengths between various atoms in the crystal were calculated. As expected the samples with the presence of larger Ba^{2+} ions exhibited larger bond lengths as compared to the sample without Ba^{2+}. The list of selected bond distances are presented in table 5.1.
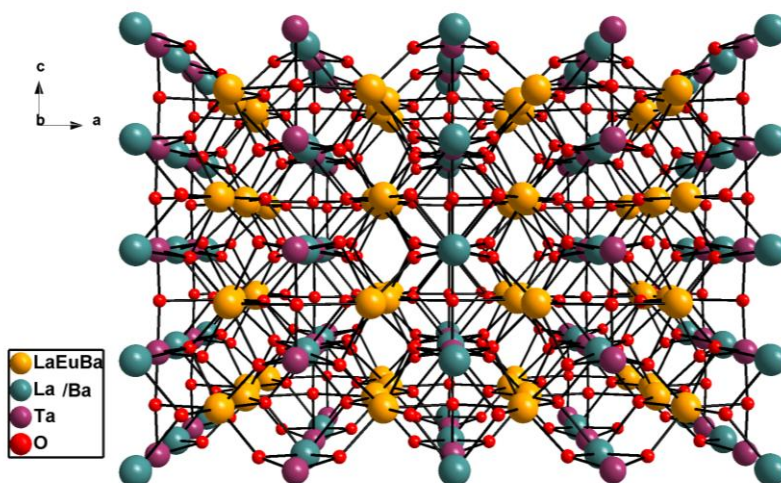
Figure 5.3 Crystal structure of $La_{2.75}TaO_7$: *0.15*Eu^{3+}, *0.1*Ba^{2+}.

Table 5.1 Selected bond distances (in Å) of $La_{2.85-y}TaO_7 : 0.15Eu^{3+}, yBa^{2+}$ samples.

		$y = 0$	$y = 0.05$	$y = 0.1$	$y = 0.15$	$y = 0.2$
La	- O	2.237	2.259	2.260	2.260	2.260
	- O	2.327	2.311	2.311	2.311	2.312
	- O	2.426	2.435	2.435	2.436	2.436
	- O	2.491	2.490	2.490	2.491	2.491
	- O	2.836	2.826	2.827	2.828	2.828
La	- O	2.490	2.490	2.491	2.491	2.491
	- O	2.848	2.850	2.850	2.851	2.851
Ta	- O	1.976	1.976	1.976	1.977	1.977
	- O	2.014	2.015	2.015	2.016	2.016
O	- Ta	2.014	2.015	2.015	2.016	2.016
	- La	2.426	2.435	2.435	2.436	2.436
	- La	2.491	2.490	2.490	2.491	2.491
	- O	2.796	2.799	2.799	2.800	2.800
	- O	2.818	2.819	2.820	2.820	2.821
	- La	2.848	2.825	2.825	2.826	2.826
	- O	2.899	2.850	2.850	2.851	2.851
	- O	2.934	2.899	2.900	2.900	2.900
	- O	3.126	2.934	2.935	2.935	2.935
	- O	3.140	3.129	3.129	3.130	3.130
	- O	3.274	3.142	3.142	3.143	3.143
	- O	3.316	3.275	3.276	3.276	3.276
O	- La	2.237	2.259	2.26	2.260	2.260
	- La	2.327	2.311	2.311	2.311	2.312
	- La	2.490	2.490	2.491	2.491	2.491
	- O	3.100	3.100	3.100	3.101	3.101
	- O	3.126	3.129	3.129	3.130	3.130
	- O	3.140	3.142	3.142	3.143	3.143
	- O	3.274	3.275	3.276	3.276	3.276
O	- Ta	1.976	1.976	1.976	1.977	1.977
	- O	2.818	2.819	2.820	2.820	2.821
	- La	2.836	2.826	2.827	2.828	2.828

5.3.2 Morphological studies
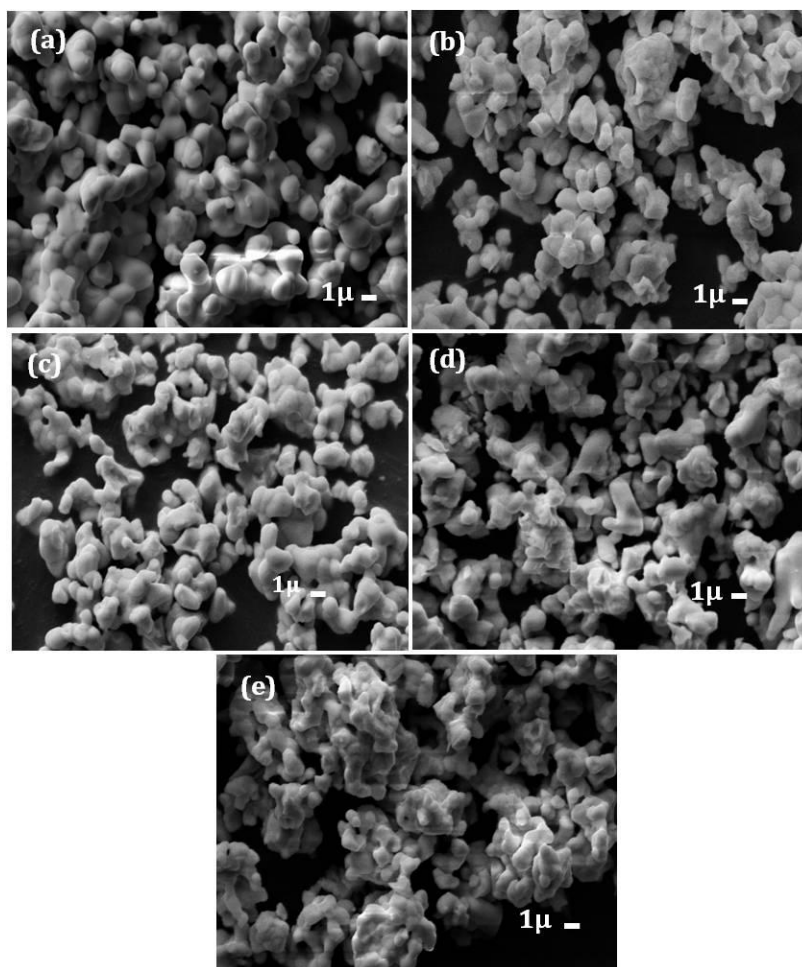
Figure 5.4 Scanning electron micrographs of $La_{2.85-y}TaO_7 : 0.15Eu^{3+}, yBa^{2+}$
(a) $y = 0$, (b) $y = 0.05$, (c) $y = 0.10$, (d) $y = 0.15$, (e) $y = 0.2$.

      The morphology of the prepared samples were observed using scanning electron microscopy and the particle sizes were found to be in 2 - 4 μ range. All the samples were slightly agglomerated and they

exhibited a slightly spherical nature. The SEM images are given in figure 5.4. X-ray dot mapped images of a representative sample showing the uniform distribution of the elements present in the sample is given in figure 5.5. EDS analysis of the samples were carried out and the stoichiometry of the samples thus obtained, matched well to the theoretically calculated values. EDS spectra of $La_{2.75}TaO_7$: *0.15*Eu^{3+}, *0.1*Ba^{2+} sample is shown in figure 5.6.
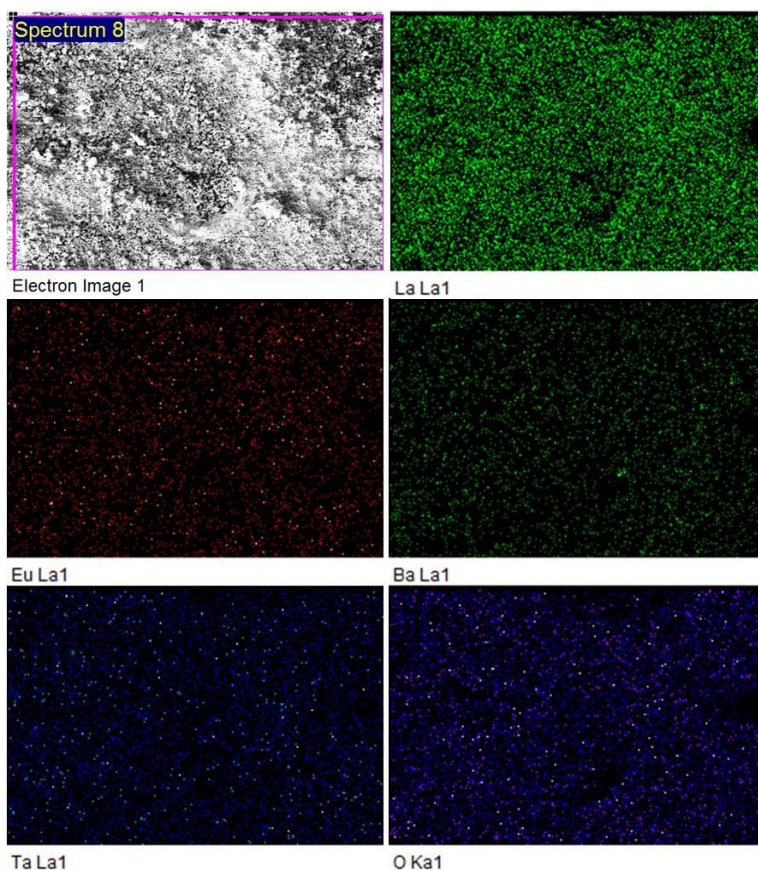
Figure 5.5 X-ray dot mapping of $La_{2.75}TaO_7$: *0.15*Eu^{3+}, *0.1*Ba^{2+}.

Element	Weight%	Atomic%
O K	18.76	68.43
Ba L	1.49	0.63
La L	51.87	21.79
Eu L	2.62	1.00
Ta M	25.26	8.15
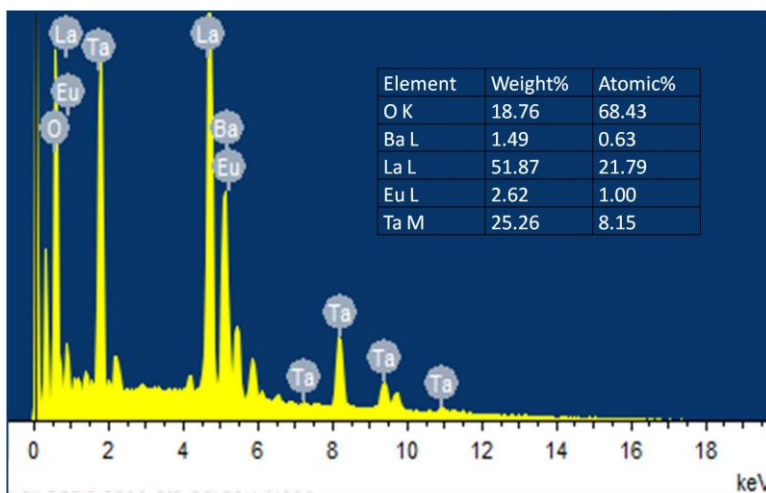
Figure 5.6 EDS spectra of La$_{2.75}$TaO$_7$: 0.15Eu^{3+}, 0.1Ba^{2+}.

5.3.3 Photoluminescence studies
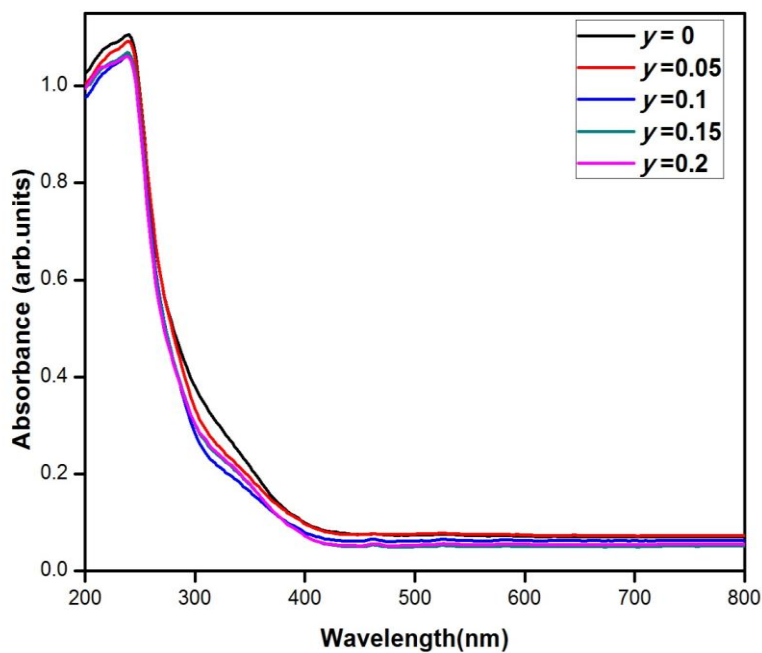
Figure 5.7 UV-visible absorption spectra of La$_{2.85-y}$TaO$_7$: 0.15Eu^{3+}, yBa^{2+}.

UV-visible absorption spectra of the prepared samples are given in figure 5.7 and it clearly shows the absorption of energy in the near UV region which is fundamentally required for a phosphor material to be used with an UV chip.
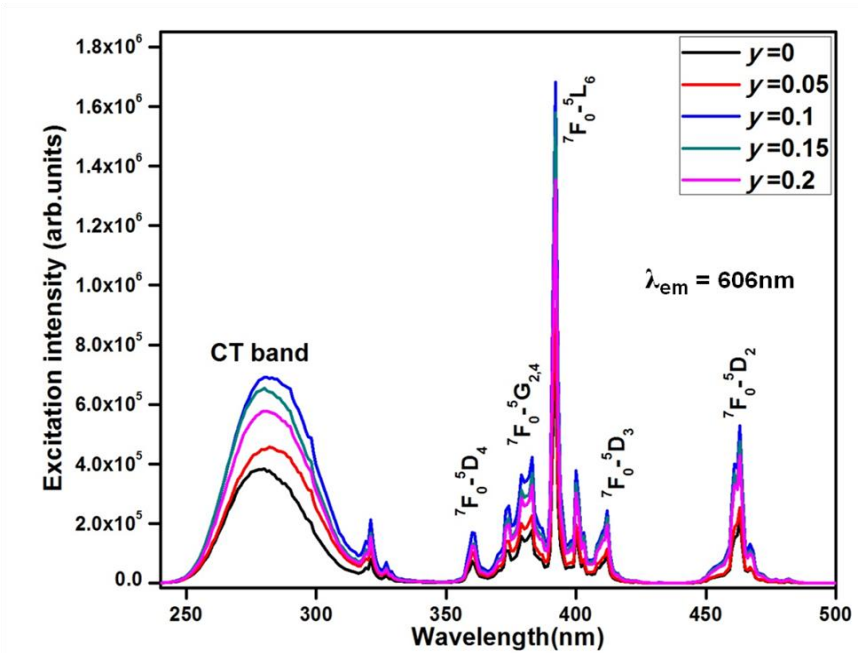
Figure 5.8 Photoluminescence excitation spectra of La$_{2.85-y}$TaO$_7$: *0.15*Eu^{3+}, *y*Ba^{2+} for an emission at 606 nm.

Figure 5.8 presents the excitation spectra of the samples for an emission of 606 nm. Excitation spectra similar to a typical spectra of Eu^{3+} doped phosphors were obtained. It consisted of a broad charge transfer band (CTB) ranging from around 240 nm to 325 nm and some sharp peaks beyond it. The most intense peaks at 392 nm and 463 nm are corresponding to the intra configurational 4f – 4f transitions of Eu^{3+} ions in the host lattice, which can be assigned to $^7F_0 \rightarrow {}^5L_6$ and $^7F_0 \rightarrow {}^5D_2$ transitions respectively. The f – f transitions of Eu^{3+} in excitation

spectra also include sharp lines at 360 nm ($^7F_0 \rightarrow {}^5D_4$), 383 nm ($^7F_0 \rightarrow {}^5G_{2,4}$) and 412 nm ($^7F_0 \rightarrow {}^5D_3$). A red-shift in the CTB band could be noticed with Ba^{2+} substitution. The observed CT band shift to lower energy upon increasing Ba content can be attributed to the resulting longer Ln - O bond length as given in table 5.1. It is well known that CT energy decreases with larger average distance to the surrounding anions.
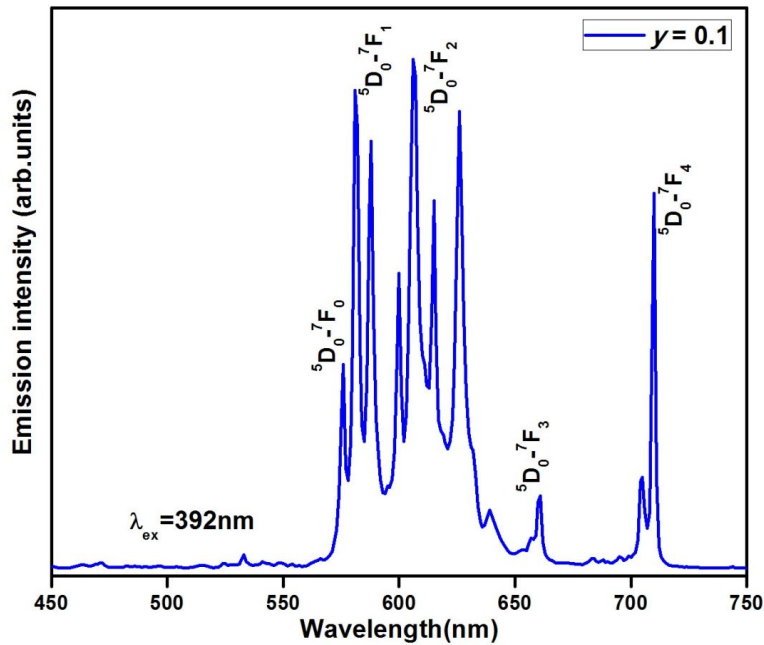
Figure 5.9 Photoluminescence excitation spectra of $La_{2.75}TaO_7$: *0.15*Eu^{3+}, *0.1* Ba^{2+} under 392 nm excitation.

Photoluminescence emission spectrum of $La_{2.75}TaO_7$: *0.15*Eu^{3+}, *0.1* Ba^{2+} under excitation at 392 nm is shown in figure 5.9. The samples exhibited multiband emissions from all the f - f transitions of Eu^{3+}. The number of splits and the wavelengths of emission was found to be

similar to the emission spectra of La$_{2.85}$TaO$_7$: 0.15Eu^{3+} phosphor. The variation of all $^5D_o \rightarrow$ $^7F_1$, $^5D_o \rightarrow$ $^7F_2$, $^5D_o \rightarrow$ $^7F_4$ emission intensities with respect to Ba^{2+} substitution levels are given in figure 5.10. Judd - Ofelt intensity parameters Ω_2 and Ω_4 were calculated and was obtained to be $\sim$ 3.8 x 10^{-20} cm^2 and 1.28 x 10^{-20} cm^2 respectively for all the Ba^{2+} substituted compounds. As seen from chapter four, the values for La$_{2.85}$TaO$_7$: 0.15Eu^{3+} were 3.46 x 10^{-20} cm^2 and 1.43 x 10^{-20} cm^2 respectively. The change in the parameters indicate the change in the local environment around the luminescent Eu^{3+}. The increase in Ω_2 value suggests an increased polarizability and increased emission intensity. The larger Ω_2 parameter is a good indication that the symmetry of the Eu^{3+} sites is distorted.
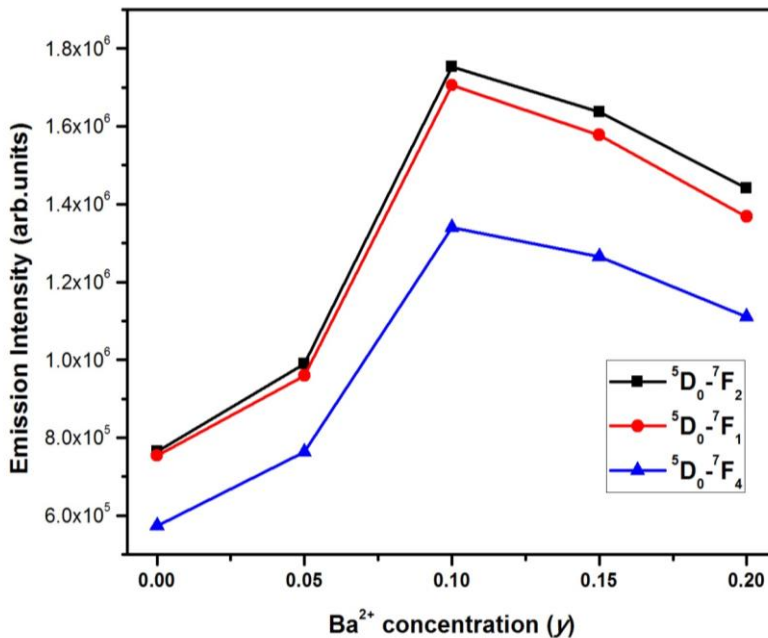
Figure 5.10 Photoluminescence excitation spectra of La$_{2.85-y}$TaO$_7$: 0.15Eu^{3+}, yBa^{2+} under 392 nm excitation.

It can be clearly noticed that the emission intensities are higher for Ba^{2+} substituted compounds. Maximum intensity was found for *y* = 0.1 substitution of Ba^{2+} in place of La^{3+}. The increased intensities could be ascribed to the increased polarizable environment around the luminescent Eu^{3+} ion. As Ln^{3+} is substituted with a larger Ba^{2+} more ordering in the host lattice could be expected. However the crystal structure of the compounds were maintained within the tolerance limit of an orthorhombhic Cmcm type. Improved ordering resulted in a more uniform distribution of Eu^{3+} ions thereby improving the luminescence intensity. However for higher substitutions of Ba^{2+}, the intensity was found to be declining. This may be due to the formation of oxygen vacancies in the lattice by the occupation of a less valence cation. The emission intensities normalized by the minimum value is given in table 5.2. It is appreciable that the emission intensity was increased to 2.3 times with Ba^{2+} substitution.

Decay curves of the samples for an excitation wavelength of 392 nm is presented in figure 5.11. The lifetimes of the samples were calculated by fitting the decay curves to single exponential function with the general formula.

$$I = A \exp(-x/\tau) \hspace{3cm} 5.1$$

where, I, τ and A are intensity, decay time and fitting parameter respectively. The exact fitting of the decay curves with a single exponential function and the non splitting nature of $^5D_0 \rightarrow {}^7F_0$ peak in the emission spectra points to the single site occupancy of Eu^{3+} ions in the host lattice. The obtained lifetime values are listed in table 5.2. However the lifetime of the samples were found to be decreasing with increasing Ba substitution.

Table 5.2 Lifetime and emission intensity ratios of samples.

Sample	Lifetime (ms)	Emission Intensity (Normalized by min)
$y = 0$	1.64	1
$y = 0.05$	1.36	1.3
$y = 0.1$	1.34	2.3
$y = 0.15$	1.26	2.1
$y = 0.2$	1.24	1.9
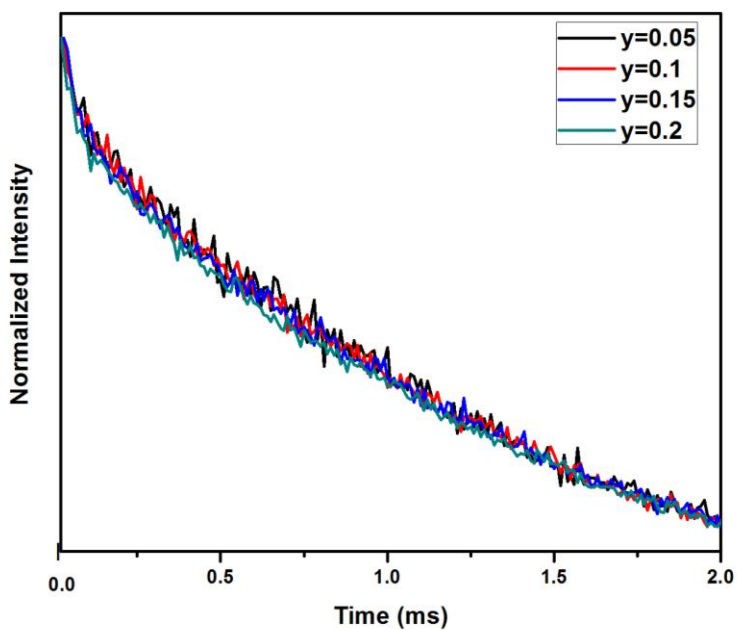
Figure 5.11 Decay curves of Eu^{3+} emission at 606 nm in $La_{2.85-y}TaO_7 : 0.15Eu^{3+}$, $y$$Ba^{2+}$ phosphors under 392 nm excitation.

The color coordinates of the samples were also calculated and they corresponded to orange - red regions of the spectrum. The values are represented in the CIE coordinate diagram as given in figure 5.12.

Figure 5.12 CIE color coordinates of emission in La$_{2.85-y}$TaO$_7$: *0.15*Eu^{3+}, *y*Ba^{2+} phosphors under 392 nm.

5.4 Conclusions

A series of La$_{2.85-y}$TaO$_7$: *0.15* Eu^{3+}, *y* Ba^{2+} (*y* = 0.05, 0.1, 0.15, 0.2*)* red phosphors were synthesized by a conventional high temperature solid state reaction route. The crystalline nature of the samples was studied by powder X-ray diffraction and it was found that the samples

processed an orthorhombic Cmcm structure. In the photoluminescence analysis, the excitation spectrum showed that the samples are well excitable in the near UV region suiting to the application point of view. The samples exhibited intense orange red emissions under 392 nm excitation. The emission intensities were highly enhanced under Ba^{2+} substitution due to the increased ordering in the host lattice. The trend in the photoluminescence properties with respect to Ba^{2+} substitution was analyzed and the influencing parameters were studied. Optimum doping concentration of Ba^{2+} was found to be $y = 0.1$.

PHOTOLUMINESCENCE PROPERTIES OF MONOCLINIC Gd_2GaTaO_7 : Eu^{3+}, Bi^{3+}

_____

Novel red phosphor materials $Gd_{2-x-y}GaTaO_7$: xEu^{3+}, yBi^{3+} were prepared using a high temperature solid state reaction route. Crystalline structure, morphology, absorbance and photoluminescence properties were studied using powder X-ray diffractometer, scanning electron microscope, UV-Vis absorption spectrophotometer and fluorescence spectrophotometer respectively. Red-shift in the charge transfer band coupled with an increased emission intensity in the red region ~ 612 nm was observed with Bi^{3+} co-doping. Energy transfer from Bi^{3+} to Eu^{3+} was found to be the major mechanism towards the enhancement of the emission intensity. Optimal doping level of Eu^{3+} and Bi^{3+} in Gd_2GaTaO_7 host was determined from the photoluminescence studies. The prepared samples exhibited higher emission intensities than the standard Y_2O_3 : Eu^{3+} red phosphors.

6.1 Introduction

The need for new phosphor technology and the rapid growth of phosphor based LED market segment has led to an extensive research into new phosphor materials. In comparison with blue and green phosphors, the existing red phosphors have some serious limitations in terms of red color purity, efficiency, and stability, which directly result in poor luminous efficiency and color rendering index of the WLED lighting system [20]. Therefore, the quest for new red phosphors with better properties is an important need. Europium ions are widely used as luminescence activator for a considerable number of phosphors owing to the strong $^5D_0 \rightarrow {}^7F_2$ transition in the red region (~612 nm) and it belongs to the main red emissive components for trichromatic fluorescence materials [21, 99]. Choosing a suitable host is very important since the red luminescence from the Eu^{3+} activator has great influence on the structure, morphology and many other factors of the host matrix [182]. Complex oxides of general compositions; $Ln_2M'MO_7$ (Ln = rare earths, M' and M = different metal ions) have been studied because of their interesting physical and chemical behavior. Although the optical properties of these type of compounds are not well explored, electrical and magnetic properties of these type of complex oxides were much reported [136, 208 - 210]. However, it is difficult to obtain phase pure compounds with this general composition without forming $LnMO_4$ secondary phase particularly in tantalate system [211]. The monoclinic superstructures are likely to arise in compounds with this general formula, and this monoclinic phase appears from the oxygen atom shifts and site vacancies with respect to the MO_2 ideal fluorite stoichiometry. The monoclinic phase compounds are closely related to the weberite structures in terms of atomic occupancy as discussed in the earlier chapters. *Wang et al.* reported the better ordering in the

crystal structure when the compounds crystallize into a monoclinic phase than the cubic phase [212]. In ordered host crystal lattice, the activator ions could be more uniformly distributed which in turn improves the photoluminescence emission intensity. Thus the host compounds with general compositions $Ln_2M'MO_7$ occupying monoclinic structure could be better host matrix for red luminescence. Hence our research interest were drawn towards such compositions whose photoluminescence behavior are not much studied. As already mentioned, attaining phase purity with the compositional diversities need to be taken special concern. In the present study, a new compound Gd_2GaTaO_7 was prepared through a solid state reaction route so as to understand the possibilities of a phase pure formation with a monoclinic space group, thereby developing a potential host matrix for Eu^{3+} red luminescence. A further attempt to improve the emission properties by co-doping the samples with Bi^{3+} was also carried out.

The influence of Bi^{3+} co-doping in enhancing the luminescence intensity either by acting as a flux or as sensitizer or by altering the crystal field surrounding the activator is already made use in many phosphor systems [121 - 123, 213 - 219]. Bi^{3+} ions are considered to be very good sensitizers for luminescence in many hosts [220 - 224]. It can efficiently absorb the UV light and transfer the energy to the luminescence center, and then the emission intensity of the luminescence center is strengthened. *Liu et al.* [216] reported an enhancement in the luminescence intensity and quantum efficiency of $ZnB_2O_4 : Bi^{3+}, Eu^{3+}$ phosphors by co-doping Bi^{3+} into the host via an energy transfer process. Quadrupole–quadrupole interaction was explained as the major energy transfer mechanism in the studies by *Liang et al.* [219] on the photoluminescence properties of $LiMgBO_3 :$ Eu^{3+}, Bi^{3+} red emitting phosphors. *Li et al.* [221] in their reports on

$LuVO_4$: Eu^{3+}, Bi^{3+} red phosphors explains the shift of excitation peaks from 350 nm to 400 nm due to the Bi(3+) - V(5+) metal - metal charge transfer. The position of the CT band and the intensity of excitation peaks of Eu^{3+} ions were significantly affected by the doping of Bi^{3+} ions in most literature. Therefore, Bi^{3+} was introduced in $Gd_{2-x}GaTaO_7$: xEu^{3+} red phosphors based on the above consideration that it is probably the eligible co-activator, strengthening and broadening the absorption in the UV region and thereby improving the photoluminescence emission properties of the samples. In this chapter, the photoluminescence properties of a new series of red phosphor materials; $Gd_{2-x}GaTaO_7$: xEu^{3+} crystallizing in a monoclinic phase are discussed. Eu^{3+} doping concentration in this host system was optimized and further improvement in the luminescence intensity was achieved by Bi^{3+} co-doping.

6.2 Experimental section

6.2.1 Synthesis

The powder phosphor samples $Gd_{2-x-y}GaTaO_7$: xEu^{3+}, yBi^{3+} (x = 0.05, 0.10, 0.15, 0.20; y = 0.05, 0.10, 0.15, 0.2, 0.25) were prepared by a high temperature solid state reaction. Individual oxides Gd_2O_3, Ga_2O_3, Ta_2O_5, Eu_2O_3 and Bi_2O_3 (Sigma Aldrich, 99.99% purity) were used as the starting materials. These oxides were weighed in the stoichiometric ratio and then finely ground and mixed in an agate mortar in an acetone medium. The samples were dried in air oven ~ 100°C for half an hour after mixing. The procedure of mixing and subsequent drying was repeated three times so as to obtain a homogeneous mixture. This mixed product was made into a pellet and then calcined on an alumina plate two times powdering and pelletizing after the first calcination at

1400°C for 6 h and 1500°C for 6 h. The calcined pellet was ground into fine powder for further characterization.

6.2.2 Characterization

The crystalline structure of the prepared powder samples was examined using an X-ray powder diffractometer (X'Pert Pro PANalytical, operated at 40 kV and 30 mA, Cu - Kα = 0.15406 nm, 2θ range = 10° - 90°). Morphological studies of phosphor particles were done by a scanning electron microscope (JEOL, JSM - 5600LV) operated at 15kV. Absorbance study of the samples were carried out using a Shimadzu, UV - 2450 UV-Vis spectrophotometer in 400 – 700 nm wavelength range using barium sulfate as a reference. The excitation and emission spectra were recorded on a Fluorolog HORIBA fluorescence spectrophotometer with a Xe lamp (450 W) as the excitation source. Luminescence lifetime of the phosphors was recorded by a phosphorimeter attached to Fluorolog®3 spectrofluorimeter. CIE color coordinates of the prepared samples were also calculated.

6.3 Results and discussion

6.3.1 Structural studies

Powder X-ray diffraction patterns of the $Gd_{2-x-y}GaTaO_7 : x Eu^{3+}$ samples are given in figure 6.1. XRD patterns of all the samples revealed the monoclinic structure with space group C2/c matching well to the powder diffraction pattern of ICDD reference code 00-056-0876. These compounds belong to the monoclinic zirconolite type structures that are layered anion deficient superstructure of a fluorite with alternating Gd - O and Ga/Ta - O layers. Ga/Ta - O layer is formed of irregular metal octahedrons whereas Gd - oxide layer is made up of Gd(1) and Gd(2)

ions which are coordinated to eight and seven oxygen atoms respectively [225]. Eu^{3+} ions are expected to occupy the Gd^{3+} sites considering the matching ionic radius and the coordination. It is inferred that the crystalline structure does not show much variation with Eu^{3+} substitution into the lattice.

Figure 6.1 Powder X-ray diffraction patterns of $Gd_{2-x}GaTaO_7 : x$$Eu^{3+}$ ($x = 0.05$, 0.10, 0.15, 0.20).
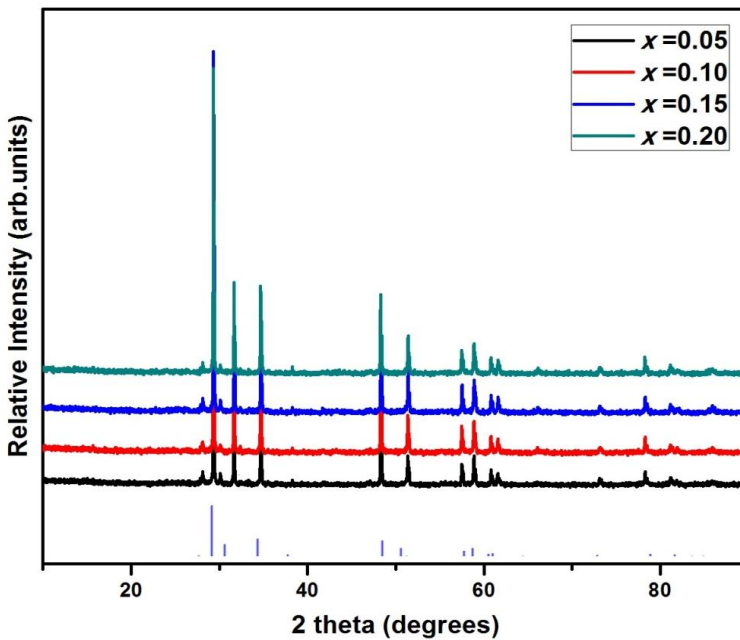
Further Bi^{3+} was co-doped to the Gd^{3+} site keeping the Eu^{3+} concentration as $x = 0.15$. The obtained powder diffraction patterns of the $Gd_{1.85-y}GaTaO_7 : 0.15$$Eu^{3+}$, $y$$Bi^{3+}$ are shown in figure 6.2. Phase pure compositions were obtained. However minor impurity peaks with relative intensities less than 5% were observed when the doping concentration of Bi^{3+} was $y = 0.25$.
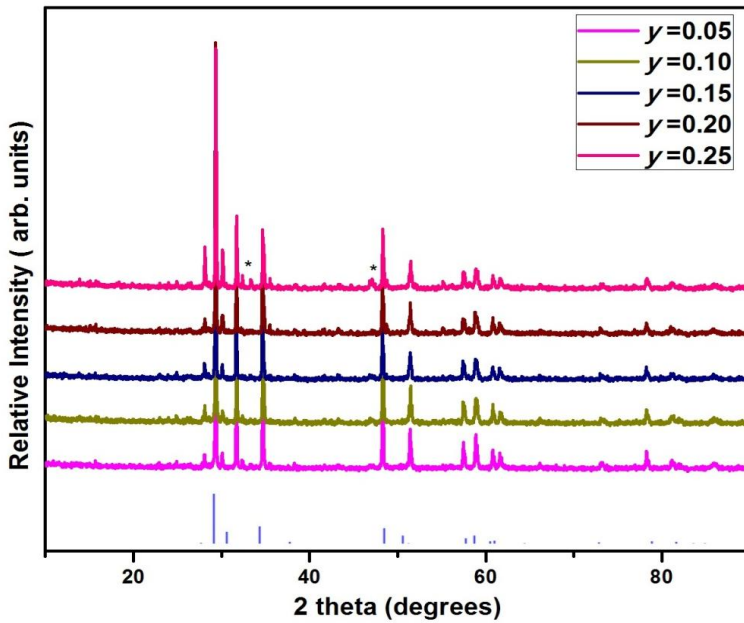
Figure 6.2 Powder X-ray diffraction patterns of $Gd_{1.85-y}GaTaO_7 : 0.15Eu^{3+}, yBi^{3+}$ ($x = 0.15; y = 0.05, 0.10, 0.15, 0.20, 0.25$).

6.3.2 Morphological studies

Morphology of the prepared samples were studied using a scanning electron microscope. The SEM images of $Gd_{2-x}GaTaO_7 : xEu^{3+}$ phosphor powder samples are given in figure 6.3. Particles were slightly agglomerated. Figure 6.4 shows the micrographs of Bi^{3+} co-doped samples. Increase in the particle size with increasing homogeneity and uniformity was observed with Bi^{3+} co-doping. Particle size is in 3 - 5 μ size range which is appropriate size for phosphor materials in the practical point of view.
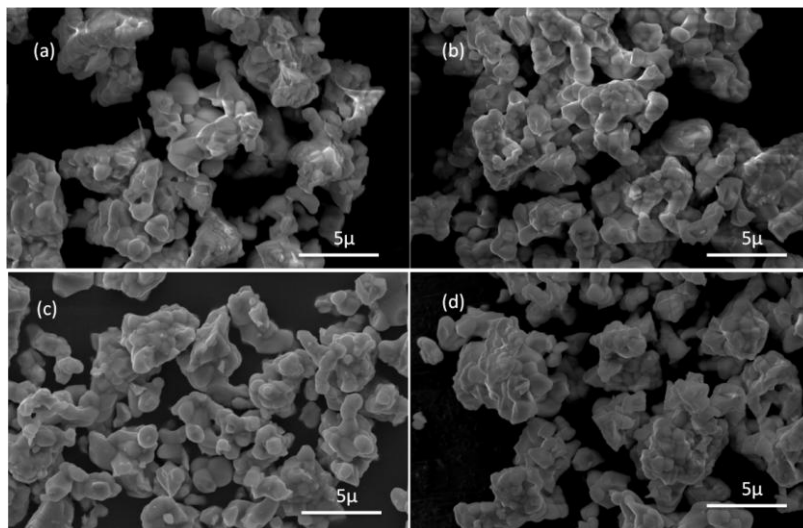
Figure 6.3 Scanning electron micrographs of $Gd_{2-x}GaTaO_7 : xEu^{3+}$
(a) x = 0.05, (b) x = 0.1, (c) x = 0.15, (d) x = 0.2.
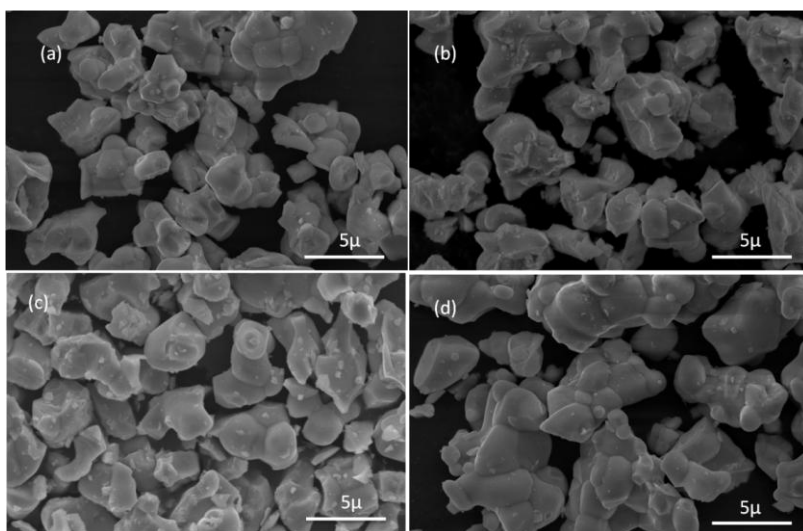
Figure 6.4 Scanning electron micrographs of $Gd_{1.85-y}GaTaO_7 : 0.15Eu^{3+}, yBi^{3+}$
(a) y =0.05, (b) y =0.1, (c) y =0.15 (d) y = 0.2.

6.3.3 Optical studies

Figure 6.5 shows the excitation spectra of Gd$_{1.85}$GaTaO$_7$: *0.15*Eu^{3+} phosphors by monitoring an emission at 612 nm. The excitation spectra consist of an intense broad band (240 - 320 nm) peaking ~274 nm and have sharp peaks beyond 350 nm. Of these sharp peaks, those at 394 and 465 nm are more intense. The broad band is corresponding to the Eu^{3+} - O^{2-} and tantalate group charge transfer band (CTB). The intense peaks at 394 and 465 nm are corresponding to $^7F_0 \rightarrow$ $^5L_6$ and $^7F_0 \rightarrow$ $^5D_2$ intraconfigurational 4f – 4f transitions of Eu^{3+} ions in the host lattice [226]. Intense excitation peak at 394 nm makes the phosphor material a potential candidate to be used with UV - LEDs.
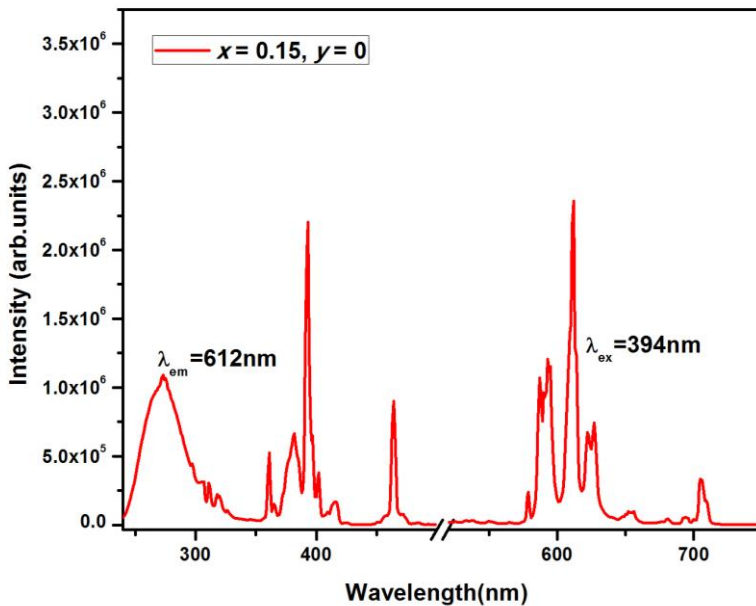
Figure 6.5 Photoluminescence excitation spectrum for an emission at 612 nm and emission spectra under 394 nm excitation of Gd$_{1.85}$GaTaO$_7$: *0.15*Eu^{3+} phosphors.

Figure 6.5 also demonstrates the emission spectra of $Gd_{1.85}GaTaO_7$: $0.15Eu^{3+}$ phosphor under 394 nm excitation. The spectrum includes characteristic $^5D_0 \rightarrow {}^7F_1$ (magnetic dipole transition) and $^5D_0 \rightarrow {}^7F_2$ (electric dipole transition) emissions at $\sim$ 593 nm and 612 nm respectively. The change in emission intensity with respect to Eu^{3+} doping is given in figure 6.6. Variation in the Eu^{3+} content doesn't change the shape and peak positions of the emission spectra although the intensity changes. It is clearly understood from the figure that a concentration quenching is observed for a doping level of x = 0.15. As the concentration of Eu^{3+} ions increases, the distance between the Eu^{3+} ions becomes smaller which favors the non-radiative pathway by energy transfer among Eu^{3+} ions that leads to luminescence quenching.
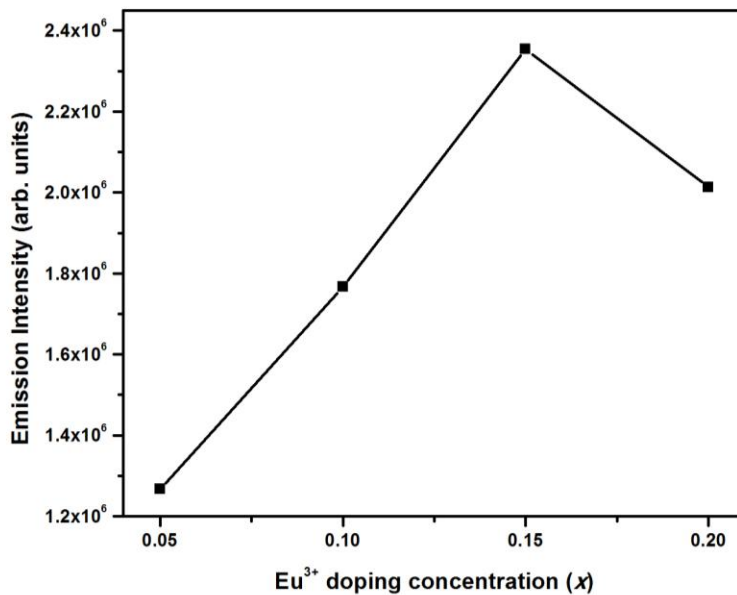
Figure 6.6 Variation in luminescent emission intensities with Eu^{3+} doping concentrations in $Gd_{2-x}GaTaO_7$: xEu^{3+} phosphors.

Figure 6.7 shows the photoluminescence excitation and emission spectra of singly doped $Gd_{1.8}GaTaO_7 : 0.2Bi^{3+}$ sample. The sample exhibited broad emission from 350 - 550 nm range which is not observable in Eu^{3+} and Bi^{3+} co-doped samples. The significant spectral overlap between the $^3P_1 \rightarrow {}^1S_0$ emission of Bi^{3+} and the f – f absorptions of Eu^{3+} indicates an energy transfer from Bi^{3+} to activator Eu^{3+}. Thus in the present system Bi^{3+} is acting as an sensitizer transferring energy to the luminescent Eu^{3+} in the host lattice.
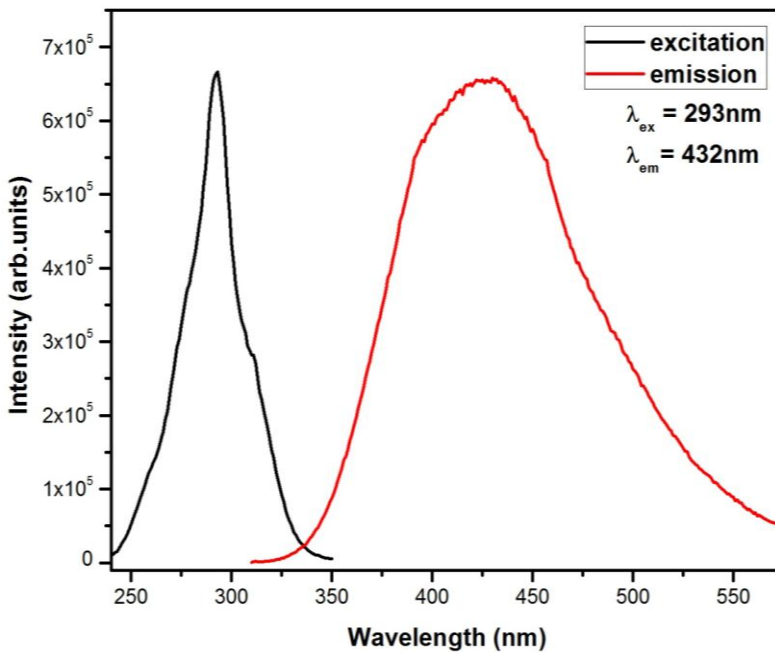
Figure 6.7 Photoluminescence excitation and emission spectra of $Gd_{1.8}GaTaO_7 : 0.2Bi$.

Photoluminescence excitation spectra of $Gd_{1.85-y}GaTaO_7$: $0.15Eu^{3+}$, yBi^{3+} (y = 0, 0.05, 0.10, 0.15, 0.2, 0.25) phosphors by

monitoring an emission at 612 nm is given in figure 6.8. When Bi^{3+} ions are co-doped into the host lattice, a significant red-shift of the charge transfer band (peak $\sim$ 286 nm) and increasing intensity of both CTB and f – f transition peaks in the excitation spectra is observed. Bi^{3+} ions absorb UV light and transfer energy to $Eu^{3+} \rightarrow O^{2-}$ improving CTB.
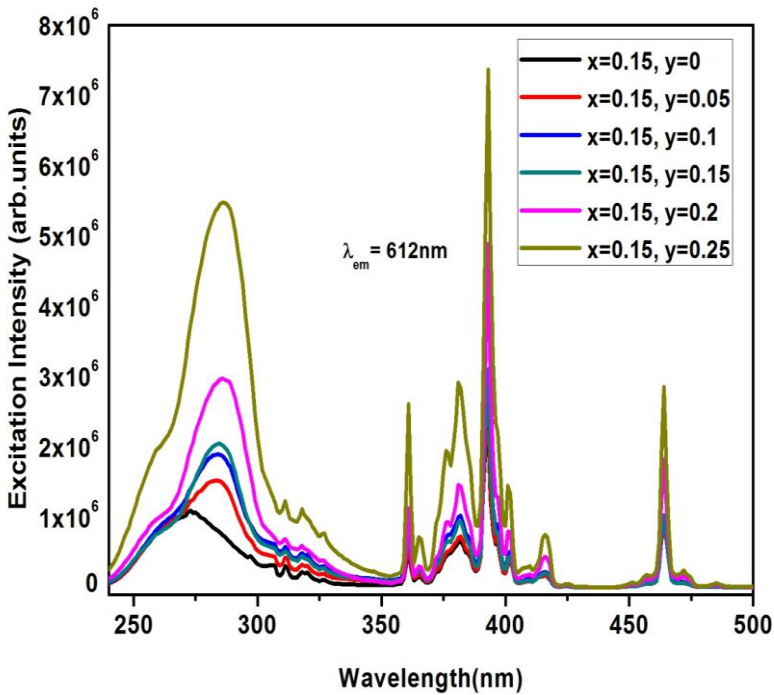
Figure 6.8 Photoluminescence excitation spectra of $Gd_{2-x-y}GaTaO_7 : xEu^{3+}, yBi^{3+}$ (x = 0.15; y = 0.05, 0.10, 0.15, 0.20, 0.25).

Figure 6.9 shows the absorption spectra of the prepared samples. Absorption spectra of the sample without Bi^{3+} consist a single absorption peak whereas an additional absorption peak with broadening is observed with Bi^{3+} co-doping which corresponds to the overlapped transition from Bi^{3+} ground state to its excited states

ascribed to $^1S_0 \rightarrow {^3P_1}$ and $^1S_0 \rightarrow {^1P_1}$ transitions [227]. It can be seen that the Bi^{3+} absorption increases progressively with increasing Bi^{3+} doping reducing $Eu^{3+} \rightarrow O^{2-}$ absorption. In the present case, Bi^{3+} is thus acting as a sensitizer. This broadening and the red-shift of the CTB with increasing intensities might have contributed highly for the luminescence properties of the samples. The parity forbidden intra configurational f-f transitions of Eu^{3+} is also strengthened by borrowing intensity from the lowest strong absorption band (CT) by non-radiative energy transfer process.
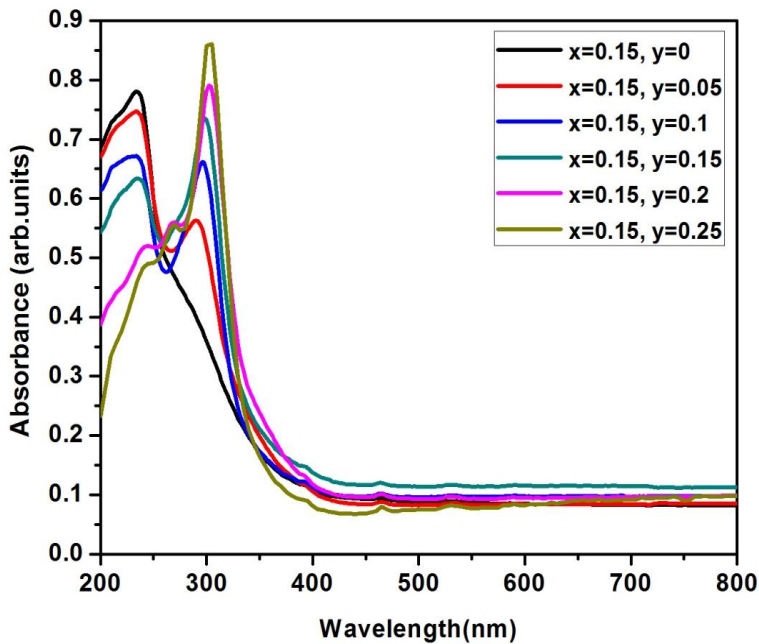
Figure 6.9 UV-Visible absorption spectra of $Gd_{2-x-y}GaTaO_7 : xEu^{3+}, yBi^{3+}$ ($x = 0.15; y = 0.05, 0.10, 0.15, 0.20, 0.25$).

Photoluminescence emission spectra of Bi^{3+} co-doped and un-co-doped $Gd_{2-x-y}GaTaO_7 : xEu^{3+}, yBi^{3+}$ and the standard red phosphor

Y_2O_3 : Eu^{3+} phosphors under 394 nm excitation are given in figure 6.10. In the emission spectra, Bi^{3+} did not alter the peak position but enhanced the emission intensity. The luminescence intensity gradually increased with increasing doping concentration of Bi^{3+} and this trend is ascribed to the increase in the absorption strength as explained earlier. In the figure, the prepared samples are compared with standard red phosphor Y_2O_3 : Eu^{3+} and it could be clearly understood that the prepared samples exhibited higher emission intensities making it promising red component for WLEDs.
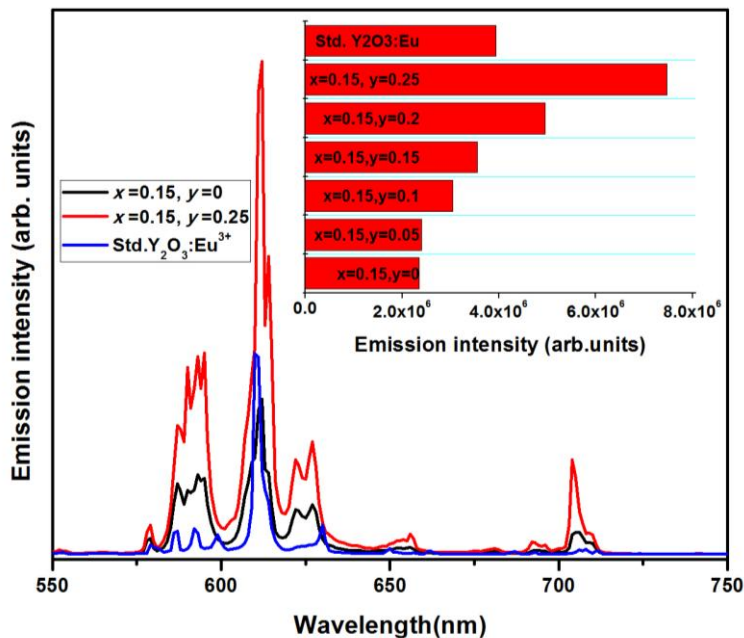
Figure 6.10 Photoluminescence emission spectra of prepared samples and standard Y_2O_3 : Eu^{3+} phosphors under 394 nm excitation (Inset: comparison of emission intensity of phosphors).

The decay curves of the samples under near UV excitation with different Eu^{3+} and Bi^{3+} concentrations are shown in figure 6.11. The

decay curves exhibit a single exponential behavior and is well fitted with the function

$$I = A \exp(-x/\tau) \qquad\qquad 6.1$$

where I, τ and A are intensity, decay time and fitting parameter respectively.
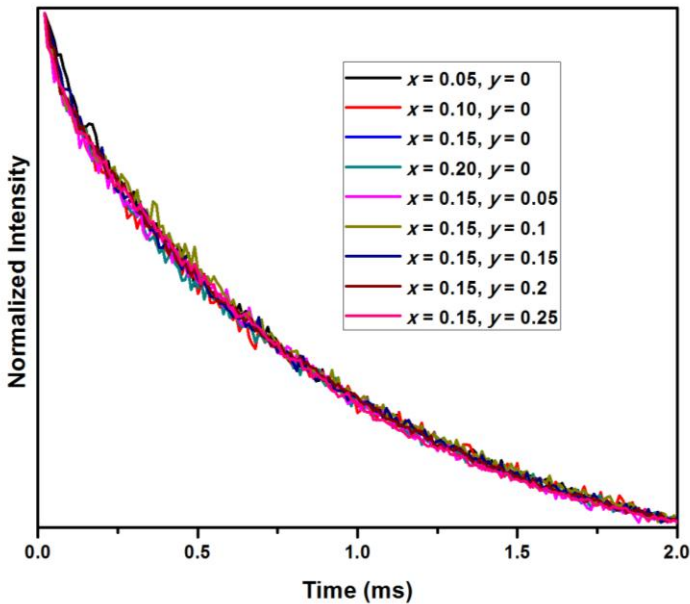
Figure 6.11 Decay curves of $Gd_{2-x-y}GaTaO_7$: xEu^{3+}, yBi^{3+} (x = 0.05, 0.10, 0.15, 0.20; y = 0.05, 0.10, 0.15, 0.20, 0.25) under near UV excitation.

Lifetime values of the phosphors are given in the table 6.1. With Bi^{3+} co-doping, the CT band is shifted to a lower energy, thereby increasing the probability of non-radiative transition through CT state, leading to faster decay. The decreasing trend in the decay time with Bi^{3+} doping further confirms the successful transfer of energy from the sensitizer (Bi^{3+}) to the activator (Eu^{3+}).

The quantum efficiency of Eu^{3+} ion in the $^5D_0$ excited state can be calculated from the emission spectra and the lifetime values of the $^5D_0$ emitting level. Assuming that only radiative and non-radiative processes are essentially involved in the depopulation of $^5D_0$ states of Eu^{3+} ion, the quantum efficiency (η) can be expressed as;

$$\eta = A_{rad}/(A_{rad} + A_{nrad}) \qquad 6.2$$

where A_{rad} and A_{nrad} are radiative and non-radiative transition probabilities respectively.

The emission intensity (I) can be taken as the integrated (S) of $^5D_0 \rightarrow {}^7F_{0-4}$ emission curves as;

$$I_{i-j}= \hbar \, \omega_{i-j} \, A_{i-j} \, N_i \sim S_{i-j} \qquad 6.3$$

where i and j are initial ($^5D_0$) and final ($^7F_{0-4}$) levels respectively; $\hbar\omega_{i-j}$ is the transition energy, A_{i-j} is the Einstein's coefficients of spontaneous emission and N_i the population of $^5D_0$ emitting level. As $^5D_0 \rightarrow {}^7F_5$ and $^5D_0 \rightarrow {}^7F_6$ transitions are not experimentally observed, their contribution to the emission intensity is neglected

The experimental coefficient of spontaneous emission (A_{0j}) can be calculated based on the relation

$$A_{0j} = A_{01} (I_{0j}/ I_{01}) (\upsilon_{01}/ \upsilon_{0j}) \qquad 6.4$$

υ_{01} and υ_{0j} are the energy baricenters of the $^5D_0 \rightarrow {}^7F_1$ and $^5D_0 \rightarrow {}^7F_j$ energy levels determined from the emission peaks of Eu^{3+} ion.

A_{01} is the Einstein's coefficients of spontaneous emission between $^5D_0$ and $^7F_1$ energy levels.

In vacuum, the average refractive index (n) is 1.506 and $(A_{0-1})_{vac}$ = 14.65 s^{-1} is considered. Then;

$$A_{0-1} = n^3(A_{0-1})_{vac} \sim 50s^{-1} \qquad 6.5$$

The lifetime (τ) of the $^5D_0$ states, A_{rad}, A_{nrad} are related as ;

$$A_{tot} = 1/\tau = A_{rad} + A_{nrad} \qquad\qquad 6.6$$

Using the equations 6.2 - 6.6 quantum efficiency of the samples was also calculated and presented in table 6.1. It was found that the value increases from 13.8 % to 16.4 % when *0.2* Bi was co-doped to $Gd_{1.85}GaTaO_7$: *0.15*Eu^{3+} composition.

Table 6.1 Lifetime, efficiency and color co-ordinates of $Gd_{2-x-y}GaTaO_7$: xEu^{3+}, yBi^{3+} phosphors.

Sample	Lifetime (ms)	Efficiency (%)	CIE color coordinates
$x = 0.05; y = 0$	0.822	12.8	(0.57, 0.35)
$x = 0.10; y = 0$	0.848	12.9	(0.59, 0.35)
$x = 0.15; y = 0$	0.867	13.8	(0.60, 0.35)
$x = 0.20; y = 0$	0.843	12.5	(0.61, 0.35)
$x = 0.15; y = 0.05$	0.929	15.8	(0.61, 0.35)
$x = 0.15; y = 0.10$	0.915	15.6	(0.61, 0.35)
$x = 0.15; y = 0.15$	0.901	16.5	(0.62, 0.35)
$x = 0.15; y = 0.20$	0.879	16.4	(0.63, 0.35)

The CIE color coordinates of the samples were calculated and given in table 6.1. The values were well matching to the standard NTSC color coordinates for red. The color purity of emission was found to be improving with increasing concentration of Bi^{3+}.

6.4 Conclusions

Novel red phosphor materials $Gd_{2-x-y}GaTaO_7 : x$Eu^{3+}, yBi^{3+} were prepared using a high temperature solid state reaction route and the structural, morphological and the photoluminescence properties were studied. The excitation and emission spectra of the prepared samples indicate that phosphor material could be effectively excited by UV light (394 nm) and it exhibits intense red emission at $\sim$ 612 nm. The optimum doping concentration of Eu^{3+} and Bi^{3+} ions in the host lattice was experimentally determined. Emission intensity was found to be highly enhanced with Bi^{3+} co-doping due to the increased absorption in the UV region. The emission intensity of the samples with higher doping concentrations (y = 0.15, 0.2, 0.25) of Bi^{3+} sample was found to be better than the standard red phosphor $Y_2O_3 : $Eu^{3+}. Thus the prepared samples could be used as potential red phosphor material nicely fitting in with the widely applied UV and blue LED chips. These developed powders along with other blue and green phosphor materials finds application in pc white LED devices.

7

CONCLUSIONS AND FUTURE ASPECTS
_____

This chapter summarizes the general conclusions, relevance and the present status of the work. The conclusions drawn from the studies can serve as a guideline for the designing of new phosphor materials with improved properties. The future scope of the present work is also discussed.
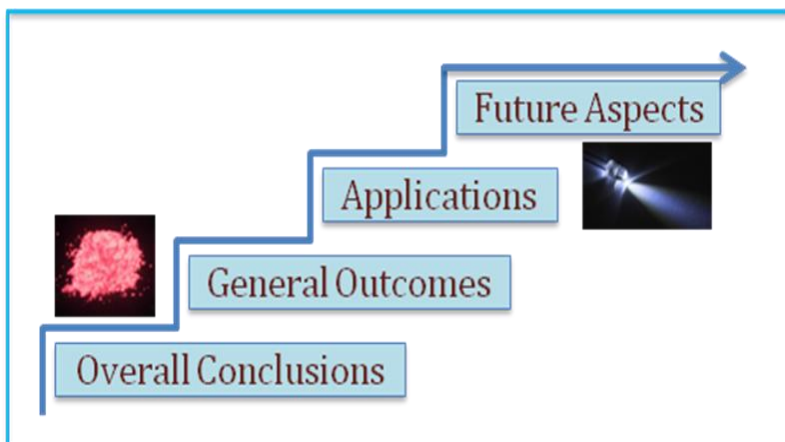
7.1 General conclusions

Several series of Eu^{3+} based red emitting phosphor materials were synthesized using solid state reaction route and their properties were characterized. The present studies primarily investigated the photoluminescence properties of Eu^{3+} in a family of closely related host structure with a general formula Ln_3MO_7. The results presented in the previous chapters throws light to a basic understanding of the structure, phase formation and the photoluminescence properties of these compounds and their co-relations.

- The variation in the Eu^{3+} luminescence properties with different M cations was studied in $Gd_{3-x}MO_7$ (M = Nb, Sb, Ta) system.

- More ordering in the host lattice and more uniform distribution of Eu^{3+} ions resulting in the increased emission properties were observed in tantalate system.

- Influence of various lanthanide ion (Lu, Y, Gd, La) substitutions on the Eu^{3+} photoluminescence properties in Ln_3MO_7 host structures was also studied.

- The difference in emission profiles with different Ln ions demonstrated the influence of long range ordering, coordination of cations and ligand polarizability in the emission probabilities, intensity and quantum efficiency of these phosphor materials.

- Better luminescence of almost equally competing intensities from all the 4f transitions of Eu^{3+} was noticed for La_3TaO_7 system.

- Photoluminescence properties were further improved in La_3TaO_7 : Eu^{3+} phosphors by the incorporation of Ba^{2+} ions in La^{3+} site.

- New red phosphor materials $Gd_{2-x}GaTaO_7$: $x$$Eu^{3+}$ exhibiting intense red emissions under UV excitation were prepared.

- Optimum doping level of Eu^{3+} in these different host lattices were experimentally determined.

- Some of the prepared samples exhibited higher emission intensities than the standard $Y_2O_3 : Eu^{3+}$ red phosphors.

The general conclusions drawn from the thesis work contribute to different sectors. This can be broadly classified as three parts:

7.1.1 Contribution to basic science

In the present studies, Eu^{3+} acts as a structural probe determining the coordination and symmetry of the atoms in the host lattice. Results from the photoluminescence studies combined with the powder XRD and Raman spectroscopy investigations helped in the determination of the correct crystal structures and phase formation of the prepared compounds. Thus the controversy regarding the space groups of these compounds could be solved to a great extent. The variation in the space groups with different cation substitutions were discussed.

There was only limited understanding regarding the various influential parameters of the photoluminescence properties of phosphor materials. From the given studies, the dependence of photoluminescence properties on the crystal structure and ordering of the host lattice, site symmetries, polarizability of the ions, distortions around the activator ion, uniformity in the activator distribution, concentration of the activator ion etc. were explained.

7.1.2 Technological applications

Although the presented work does not directly evidence any application, the materials developed in the studies can be used for lighting applications together with other components for LED lighting. All the prepared samples were well excitable under near UV radiation. $La_3TaO_7 : $ *0.15*Eu^{3+} phosphor with high efficiency and intense orange

red emissions can be used as a potential red component for the realization of white light with better color rendering properties. Gd_2GaTaO_7 : Eu^{3+}, Bi^{2+} red phosphors give good color purity matching to NTSC standards of red. Some of these compounds exhibited higher emission intensities than the standard Y_2O_3 : Eu^{3+} red phosphors. However thermal stability and electrical output using these compounds should be studied further before applications.

71.3 Ideas that could be adopted to other phosphor systems

Based on the studies in the closely related Ln_3MO_7 structures, some ideas on selecting better host lattice for improved luminescence properties could be drawn. Analyzing the CTB position and the number of emission splits, a general understanding on the doping sites can be obtained. These results could be helpful for phosphor designs in other host systems also, for enhanced emission intensity and efficiency.

7.2 Future aspects of this work

Luminescence in Ln_3MO_7 compounds are of both academic and technological interests. This thesis explains the structure and photoluminescence of some compounds that promises future scope of work and applications. To analyze the site occupancy of the Eu^{3+} activator ions, studies using time resolved emission spectroscopy (TRES) and electron paramagnetic resonance (EPR) studies are suggested. A further enhancement in the emission intensity and efficiency can be expected by different cationic modifications, different codoping techniques, alternate synthesis routes, alteration in the morphology of the particles, etc. Analysis of the thermal stability and its optimization is required. Incorporation of the developed phosphor

powders to UV chip and the study of the output characteristics could be a future prospect of this work.

References

1. S. Tonzani, Nature. 459 (2009) 312.

2. Center for climate and energy solutions, Lighting efficiency : Climate TechBook, April 2011.

3. D.A. Steigerwald, J.C. Bhat, D. Collins, R.M. Fletcher, M.O. Holcomb, M.J. Ludowise, P.S. Martin, S.L. Rudaz IEEE J. Sel. Topics Quantum Electron. 8 (2002) 310.

4. Department of Energy, Office of Energy Efficiency and Renewable Energy, Solid-State Lighting Research and Development Multi-Year Program Plan, April 2013. (http://apps1.eere.energy.gov/buildings/ publications/pdfs/ssl/ssl_mypp2013_web.pdf.)

5. J.E. Kaufman, J.F. Christensen, Lighting Handbook, Waverly Press, Maryland (1972).

6. M. Nisa Khan, Understanding LED illumination, CRC Press, Taylor & Francis group, Florida (2014).

7. W.R. Stevens, Building Physics: Lighting, Pergamon Press, London, (1969).

8. Q.Y. Zhang, K. Pita, W. Ye, W.X. Que, Chem. Phys. Lett. 351 (2002) 163.

9. Q.Y. Zhang, K. Pita, S. Buddhudu, C.H. Kam, J. Phys. D. 35 (2002) 3085.

10. J.E. Schanda, Colorimetry: Understanding the CIE system, Wiley, Hoboken, New Jersey (2007).

11. Department of Energy, Office of Energy Efficiency and Renewable Energy, Lighting Research and Development, Solid-State Lighting Research and Development, Multi-Year Program Plan FY'09- FY-14, prepared by Navigant Consulting Inc., Radcliffe Advisors and SSLS Inc., Washington DC, March 2008. (http://apps1.eere.energy.gov/ buildings/publications/pdfs/ssl/ssl_mypp2008_web.pdf.)

12. Department of Energy, Office of Energy Efficiency and Renewable Energy, Solid-State Lighting Research and Development Multi-Year

Program Plan, prepared by Bardsley Consulting, Navigant Consulting Inc., Radcliffe Advisors Inc. and SB Consulting, Solid State Lighting Services Inc., Washington DC., April 2012. (http://apps1.eere.energy .gov/buildings/publications/pdfs/ssl/ssl_mypp2012_web.pdf.)

13. N. Khan, N. Abas, Renew. Sust. Energ. Rev. 15 (2011) 296.

14. H.J. Round, Electr. World 49 (1907) 309.

15. O.V. Losev, Telegrafi ya i Telefoniya bez Provodov. 44 (1927) 485. USSR patent 12191 (1929).

16. N. Holonyak, S.F. Bevacqua, Appl. Phys. Lett. 1 (1962) 82

17. G. Fasol, S. Nakamura, The Blue Laser Diode: GaN Based Blue Light Emitters and Lasers, Springer, Berlin (1997).

18. N.S. Shinbun, "p-n junction DH blue LEDs with a brightness of more than 1000 mcd were developed by Nichia Chemical Industries Ltd.," Japanese newspaper press release, Nov. 30 (1993).

19. J. McKittrick, L.E. Shea-Rohwer, J. Am. Ceram. Soc. 97 (2014) 1327.

20. C.C. Lin, R. Liu, J. Phys. Chem. Lett 2 (2011) 1268.

21. C. Ronda, Luminescence from Theory to Applications, Wiley-VCH Verlag GmbH & Co. KGaA, Weinheim, 2008.

22. K.N. Shinde, Phosphate Phosphors for Solid-State Lighting, Springer Series in Materials Science 174, Springer-Verlag Berlin Heidelberg (2013).

23. C. Feldmann, T. Justel, C.R. Ronda, P.J. Schmidt, Adv. Funct. Mater. 13 (2003) 511.

24. G. Blasse, Handbook on Physics and Chemistry of Rare earths, North Holland Publishing Company, Netherlands (1979).

25. H.S. Nalwa, L.S. Rohwer, Handbook of Luminescence, Display Materials and Display Devices, American Scientific Publishers, California (2003).

26. G. Blasse, Chem. Mater. 1 (1989) 294.

27. Hardy, E. Austin, IEEE Trans. Broadcast Telev. Receivers, 11 (1965) 33.

28. A.K. Levine, F.C. Palilla, App. Phys. Lett. 5 (1964) 118.

29. J. Silver, SID Symposium Digest of Technical Papers, 36 (2005) 594.

30. C.R. Ronda, T. Justel, H. Nikol, J. Alloys Compd. 275 (1998) 669.

31. R.J. Xie, N. Hirosaki, Sci. Technol. Adv. Mater. 8 (2007) 588.

32. P.A. Tick, J. Appl. Phys. 78(1995) 6367.

33. S. Tanabe, J. Non-Cryst. Solids. 259 (1999) 1.

34. S. Jiang, M. Myers, N. Peyghambarian, J. Non-Cryst. Solids. 239 (1998) 143.

35. M.F. Joubert, Opt. Mater. 11 (1999) 181.

36. M. Jayasimhadri, J. Phys. D: Appl. Phys. 39 (2006) 635.

37. M.H. Huang, S. Mao, H. Feick, H. Yan, Y. Wu, H. Kind, E. Weber, R. Russo, P. Yang, Science. 292 (2001) 1897.

38. H. Ratinen, Phys. Status Solidi A. 12 (1972) 447.

39. R.V. Alves, R.A. Buchanan, IEEE Trans. Nucl. Sci. 20 (1973) 415.

40. S.L. Issler, C.C. Torardi, J. Alloys Compd. 229 (1995) 54.

41. W. Kostler, A. Winnacker, W. Rossner, B.C. Grabmaier, J. Phys. Chem. Solid 56 (1995) 907.

42. R. Nakamura, J. Am. Ceram. Soc. 82 (1999) 2407.

43. K. Tanaka, J. Appl. Phys. 89 (2001) 5449.

44. N. Kalivas, L. Costaridou, I. Kandarakis, D. Cavouras, C.D. Nomicos, G. Panayiotakis, Nucl. Instrum. Methods Phys. Res., Sect. A. 490 (2002) 614.

45. Y. Tian, W.H. Cao, X.X. Luo, Y. Fu, J. Alloys Compd. 433 (2007) 313.

46. G. Fern, T. Ireland, J. Silver, R. Withnall, A. Michette, C. McFaul, S. Pfauntsch, Nucl. Instrum. Methods Phys. Res. Sect. A. 600 (2009) 434.

47. I.D. Jung, M.K. Cho, S.M. Lee, K.M. Bae, P.G. Jung, C.H. Lee, J.M. Lee, S. Yun, H.K. Kim, S.S. Kim, J.S. Ko, J. Micromech. Microeng 19 (2009) 015014.

48. J. Zhang, Z. Hao, X. Zhang, Y. Luo, X. Ren, X.J. Wang, J. Zhang, J. Appl. Phys. 106 (2009) 034915.

49. G. Blasse, Chem. Mater. 6 (1994) 1465.

50. C. Greskovich, S. Duclos, Annu. Rev. Mater. Sci. 27 (1997) 69.

51. C.W.E. van Eijk, Phys. Med. Biol. 47 (2002) R85.

52. A.M. Srivastava, J. Lumin. 129 (2009) 1419.

53. T. Justel, H. Nikol, C. Ronda, Angew. Chem. Int. Ed. 37 (1998) 3085.

54. J.C.G. Bunzli, C. Piguet, Chem. Soc. Rev. 34 (2005) 1048.

55. S. Shionoya, W.M. Yen, H. Yamamoto, Phosphor Handbook. Second Edition. CRC press: Boca Rotan (2006).

56. S. Ekambaram, K.C. Patil, M. Maaza, J. Alloys Compd. 393 (2005) 81.

57. S.V. Eliseeva, J.C.G. Buenzli, Chem. Soc. Rev. 39 (2010) 189.

58. A. Shalav, B.S. Richards, M.A. Green, Sol. Energy Mater. Sol. Cells 91 (2007) 829.

59. B.S. Richards, Sol. Energy Mater. Sol. Cells 90 (2006) 189.

60. A. Shalav, B.S. Richards, T. Trupke, K.W. Kramer, H.U. Gude, Appl. Phys. Lett. 86 (2005) 013505.

61. T. Trupke, M.A. Green, Wurfel, J. Appl. Phys. 92 (2002) 4117.

62. C.C. Chen, E. Xie, Sci. China, Ser. G. 57 (2014) 433.

63. H.L. Li, R.J. Xie, N. Hirosaki, T. Takeda, G.H. Zhou, Int. J. Appl. Ceram. Tec. 6 (2009) 459.

64. H.S. Kim, T. Horikawa, H. Hanzawa, K. Machida, J. Phys. Conference Series 379 (2012) 012016.

65. X. Piao, K. Machida, T. Horikawa, H. Hanzawa, Chem. Mater. 19 (2007) 4592.

66. A.A. Setlur, W.J. Heward, Y. Gao, A.M. Srivastava, R. GopiChandran, M.V. Shankar, Chem. Mater. 18 (2006) 3314.

67. P.S. Dutta, A. Khanna, ECS J. Sol. Stat. Sci. Technol. 2 (2013) R3153.

68. S. Neeraj, N. Kijima, A.K. Cheetham, Solid State Commun. 131 (2004) 65.

69. A.K. Parchura, R.S. Ningthoujam, Dalton Trans. 40 (2011) 7590.

70. Z.J. Zhang, H.H. Chen, X. Yang, Zhao, J. Mater. Sci. Eng. B. 145 (2007) 34.

71. S. Lei, X. Zhang, Z. Li, T. Yu, Z. Zou, J. Electrochem. Soc. 156 (2009) 367.

72. X. Li, X. Su, P. Liu, J. Liu, Z. Yao, J. Chen, H. Yao, X. Yu, M. Zhan, Cryst. Eng. Comm. 17 (2015) 930.

73. C. Liao, R. Cao, Z. Ma, Y. Li, G. Dong, K.N. Sharafudeen, J. Qiu, J. Am. Ceram. Soc. 96 (2013) 3552.

74. Z. Jiang, Y. Wang, L. Wang, J. Electrochem. Soc. 157 (2010) J155.

75. P. Huang, D. Liu, C.E. Cui, L. Wang, G. Jiang, Appl. Phys. A. 116 (2014) 759.

76. Y. Fu, J. Mater Sci. 42 (2007) 5165.

77. L.S. Chi, R.S. Liu, B.J. Leeb, J. Electrochem. Soc. 152 (2005) J93.

78. X. Luo, W. Cao, M. Xing, J. Rare Earth. 24 (2006) 20.

79. Y. Kim, S. Choi, J. Park, E. Bok, B. Kim, S. Hong, ECS J. Solid State Sci. Technol. 2 (2013) R3021.

80. Z. Xinmin, W. Hao, Z. Heping, S. Qiang, J. Rare Earth. 25 (2007) 701.

81. J. Kim, J. Park, K. Kim, S. Lee, C. Kim, J. Inform. Display. 7 (2006) 13.

82. I. Baginskiy, R.S. Liu, C.L. Wang, R.T Lin, Y.J. Yao, J. Electrochem. Soc. 158 (2011) 118.

83. J. Botterman, K.V. Eeckhout, A.J.J. Bos, P. Dorenbos, P.F. Smet, Opt. Mater. Exp. 2 (2012) 341.

84. H. Yang, Q. Liu, Q. Wei, Z. Zhou, J. Wan, G. Liu, R. Xie, J. Am. Ceram. Soc 97 (2014) 3164.

85. E. Kang, S. Choi, S. Hong, ECS J. Solid State Sci. Technol. 1 (2012) R11.

86. Y. Shimomura, T. Kurushima, N. Kijima, J. Electrochem. Soc. 154 (2007) J234.

87. C. Corrado, Y. Jiang, F. Oba, M. Kozina, F. Bridges, J.Z. Zhang, Phys. Chem. A. 113 (2009) 3830.

88. L. Wei, H. Zhendong, Z. Xia, L. Yongfu, L. Yongshi, L. Xingyuan, W. Xiaojun, Z. Jiahua, J. Electrochem. Soc. 158 (2011) H124.

89. G. Zhu, S. Yurong Shi, M. Masayoshi, Y. Shimomura, Y. Wang, Opt. Mater. Exp. 3 (2013) 229.

90. K. Komatsu, A. Nakamura, A. Kato, S. Ohshio, H. Saitoh, Phys. Status Solidi C. 12 (2015) 809.

91. Z.C. Wu, J.X. Shi, J. Wang, M.L. Gong, Q. Su, J. Solid State Chem. 179 (2006) 2356.

92. Y. Ruijin, J. Wang, M. Zhang, J. Zhang, H. Yuan, Q. Su, Chem. Phys. Lett. 453 (2008) 197.

93. W.B. Im, Y.I. Kim, H.S. Yoo, D.Y. Jeon, Inorg Chem. 19 (2009) 557.

94. D. Kim, S. Park, S. Kim, S. Kang, J. Park, Inorg. Chem. 53 (2014) 11966.

95. Y. Wen, Y.H. Wang, B.T. Liu, F. Hang, Y.R. Shi, Funct. Mater. Lett. 5 (2012) 1250048

96. J.S. Kim, P.E. Jeon, Y.H. Park, J.C. Choi, H.L. Park, Appl. Phys. Lett. 85 (2004) 3696.

97. T. Nishida, T. Ban, N. Kobayashi, Appl. Phys. Lett. 82 (2003) 3817.

98. J. Jeong, V.R. Bandi, B.K. Grandhe, K. Jang, H.S. Lee, J. Korean Phys. Soc. 58 (2011) 306.

99. M. Nazarov, D. Y. Noh, New Generation of Europium and Terbium Activated Phosphors: From Syntheses to applications, Pan Stanford Publishing, Pte. Ltd., Singapore (2011).

100. C. Gorller-Walrand, K. Binnemans, Rationalization of Crystal-Field Parametrization, in Handbook on the Physics and Chemistry of Rare Earths, ed. K. A. Gschneidner Jr. and L. Eyring, North-Holland, Amsterdam. 23 (1996).

101. Y.D. Huh, J.H. Shim, Y. Kim, Y.R. Do, J. Electrochem. Soc. 150 (2003) H57.

102. Y. Sato, N. Takahashi, S. Sato, J. Appl. Phys. 35 (1996) L838.

103. Y.D. Huh, J.Y. Park, S.S. Kweon, J.H. Kim, J.G. Kim, Y.R. Do, Bull. Korean Chem. Soc. 25 (2004) 1585.

104. Y.C. You, J.S. Choi, Y.R. Do, T.W. Kim, H.L. Park, Solid State Commun. 99 (1996) 961.

105. K. Kato, F. Okamoto, J. Appl. Phys. 22 (1983) 76.

106. N. Yamashita, O. Harada, K. Nanamura, J. Appl. Phys. 34 (1995) 5539.

107. Y.S. Hu, W.D. Zhuang, H.Q. Ye, S.S. Zhang, Y. Fang, X.W. Huang, J. Lumin. 111 (2005) 139.

108. P. Thiyagarajan, M. Kottaisamy, M.S. RamachandraRao, J. Phys. D: Appl. Phys. 39 (2006) 2701.

109. Z. Wang, H. Liang, M. Gong, Q. Su, J. Alloys Compd. 432 (2007) 308.

110. S. Neeraj, N. Kijima, A.K. Cheetham, Chem. Phys. Lett. 387 (2004) 2.

111. C.H. Chiu, C.H. Liu, S.B. Huang, T.M. Chen, J. Electrochem. Soc. 154 (2007) J181.

112. P.L. Li, Z.P. Yang, Z.J. Wang, Q.L. Guo, Mater Lett 62 (2008) 1455.

113. P. Ghosh, S. Sadhu, A. Patra, Phys. Chem. Chem. Phys. 28 (2006) 3342.

114. J. Llanos, R. Cortes, J. Lumin 129 (2009) 465.

115. W. Chen, X. Dai, X. Yang, Y. Liu, Res. Mater. Sci. 3 (2014) 52.

116. P. Sharma, S. Brown, G. Walter, S. Santra, B. Moudgil, Adv. Colloid Interface Sci. 471 (2006) 123.

117. M.H. Hwang, Y.J. Kim, Ceram. Inter. 34 (2008) 1117.

118. Y. Zhou, Q. Ma, M. Lu, Z. Qiu, A. Zhang, J. Phys. Chem. C. 112 (2008) 19901.

119. B. Li, Z. Gu, J. Mater. Sci. 35 (2000) 1139.

120. G.C. Bleier, M. Nyman, L.E.S. Rohwer, M.A. Rodriguez, J. Solid State Chem. 84 (2011) 3221.

121. H. Junli, Z. Liya, L. Zhaoping, G. Fuzhong, H. Jianpeng, W. Rongfang, J. Rare Earth. 28 (2010) 356.

122. V.B. Maggay, P. Lin, W. Liu, J. Solid State Lighting. 13 (2014) 1.

123. Z. Xia, D. Chen, M. Yang, T. Ying, J. Phys. Chem. Solids. 71 (2010) 175.

124. F. Li, Y. Wang, S. Xin, F. Zhang, J. Zhang, J. Nanosci. Nanotechnol. 14 (2014) 3440.

125. X. Zhou, G. Wang, T. Zhou, K. Zhou, Q. Li, Z. Wang. J. Nanosci. Nanotechnol. 14 (2014) 3494.

126. X. Geng, Y. Tian, Y. Chen, L. Xiao, Y. Xie, Appl. Phys. B. 107 (2012) 177.

127. H.J. Rossell, J. Solid State Chem. 2 (1979) 115.

128. L. Cai, S. Denev, V. Gopalan, J.C. Nino, J. Am. Ceram. Soc. 93 (2010) 875.

129. L. Cai, J.C. Nino, J. Solid State Chem. 184 (2011) 2263.

130. G. King, C.M. Thompson, J.E. Greedan, A.J. Llobet, J. Mater. Chem A. 1 (2013) 10487.

131. C.R. Stanek, Atomic scale disorder in fluorite and fluorite related oxides, Ph.D Thesis, University of London, London (2003).

132. M.A. Subramanian, G. Aravamudan G.V. SubbaRao, Prog. Solid State Chem. 15 (1983) 55.

133. A.K. Harari, L. Mazerolles, D. Michel, F. Robert, J. Solid state Chem. 116 (1995) 103.

134. L. Cai, J.C. Nino, Acta Cryst. B65 (2009) 269.

135. Y. Hinatsu, Y. Doi, J. Solid State Chem, 198 (2013) 176.

136. E. Grey, W.G. Mumme, T.J. Ness, R.S. Roth, K.L. Smith J. Solid State Chem. 174 (2003) 285.

137. W.T. Fu, D.J. W. Ijdo, J. Solid State Chem. 182 (2009) 2451.

138. K.P.F. Siqueria, R.M. Borhes, E. Granado, L.M. Malard, A.M. de Paula, R.L. Moreira, E.M. Bittar, A. Dias, J. Solid State Chem. 203 (2013) 326.

139. K.P.F. Siqueira, J.C. Soares, E. Granado, E.M. Bittar, A.M. de Paula, J. Solid State Chem. 209 (2014) 63.

140. R.C Severence, A.H. Fox, S.J. Mugavero, M.D. Smith, J. Chem Crystallogr. 41 (2011) 496.

141. S.A. Kovyazina, L.A. Perelyaeva, I.A. Leonidov, Yu. A. Bakhteeva, J. Struct. Chem. 44 (2003) 975.

142. H. Nishimine, M. Wakeshima, Y. Hinatsu, J. Solid State Chem. 177 (2004) 739.

143. H. Nishimine, M. Wakeshima, Y. Hinatsu, J. Solid State Chem. 178 (2005) 1221.

144. M. Wakeshima, Y. Hinatsu, J. Solid State Chem. 179 (2006) 3575.

145. M. Wakeshima, H. Nishimine, Y. Hinatsu, J. Phys.: Condens. Matter. 16 (2004) 4103.

146. J. Reading, C.S. Knee, M.T. Weller, J. Mater. Chem. 12 (2002) 2376.

147. J.E. Greedan, N.P. Raju, A. Wegner, J. Solid State Chem. 129, (1997) 320.

148. L. Cai, J.C. Nino, J. Eur. Ceram. Soc. 27 (2007) 3971.

149. L. Cai, J.C. Nino, J. Eur. Ceram. Soc. 30 (2010) 307.

150. L. Cai, Fundamental structure-dielectric property relationships in fluorite-related ceramics, PhD Thesis, University of Florida, (2010)

151. N. Preux, A. Rolle, C. Merlin, M. Benamira, M. Malys, C. Estournes, A. Rubbens, R.N. Vannier, Comptes Rendus Chimie. 13 (2010) 1351.

152. R. Abe, M. Higashi, Z. Zou, K. Sayama, Y. Abe, H. Arakawa, J. Phys. Chem. 108 (2004)3.

153. D. Yanyan, Z. Yuan, H. Keke, W. Shan, Y. Long, F. Shouhua, Dalton Trans. 42 (2013) 8041.

154. Z. Yuan, F. Wenchun, H. Keke, Y. Long, D. Yanyan, W. Xiaofeng, S. Feng, Eu. J. Inorg. Chem. I4 (2015) 90.

155. J. Wang, Y. Cheng, Y. Huang, P. Cai, S. Kim, H.J. Seo, J. Mater Chem. 2 (2014) 5559.

156. A.R. West, Solid State Chemistry and its Applications, John Wiley and Sons, Singapore (1984).

157. M.N. Rahaman, Ceramic processing and sintering Dekker: New York (2003).

158. B.D. Cullity, Elements of X-ray Diffraction, 2nd Ed, Addison Wesley Publishing Company, Massachusetts (1978).

159. H.M. Rietvelt, J. Appl. Cryst. 2 (1969) 65.

160. J.J. Bozzola, L.D. Russell, Electron Microscopy, Jones and Bartlett Publishers Inc, Boston (1992).

161. J.I. Goldstein, D.E. Newbery, P. Echlin, D.C. Joy, C. Fiori, E. Lifshin, Scanning electron microscopy and X-ray microanalysis, Plenum press, New York (1981).

162. S.L. Flegler, J.W. Heckman, K.L. Klomparens, Scanning and Transmission Electron Microscopy, W. H. Freeman and Company, New York (1993).

163. Revised from commercial literature provided by SLM Instruments.

164. B. Henderson, G.F. Imbusch, Optical Spectroscopy of Inorganic Solids, Clarendon Press, Oxford (1989).

165. I. Pelant, J. Valenta, Luminescence Spectroscopy of Semiconductors, Oxford University Press, New York (2012).

166. HORIBA Jobin Vyon Inc. Operation manual Part number J81014 rev. D. March (2008) and J81075 rev. B. August (2003).

167. S . Fujihara, K. Tokumo, Chem Mater. 17 (2005) 5587.

168. J.C.G. Bünzli, G.R. Choppin, Lanthanide probes in life, chemical and earth sciences: Theory and practice, Elsevier, New York, (1989).

169. K. Binnemans, C. Gorller-Walrand, J. Rare Earth. 14 (1996) 173.

170. H.P. Rooksby, E.A.D. White, J. Am. Ceram. Soc. 47 (1964) 94.

171. G. Tilloca, M.Perez, Y. Jorba, Comp. Rend. acad. Sci. 271 (1970) 134.

172. N. Ishizawa, K. Tateishi, S. Kondo, T. Suwa, Inorg. Chem. 47 (2008) 558 .

173. Y. Yokogawa, M. Yoshimura, S. Somiya, Solid State Ionics. 35 (1989) 275.

174. T. Fennell, S.T. Bramwell, M.A. Green, Can. J. Phys. 79 (2001) 1415

175. Shannon R, Acta Cryst. A. 32 (1976) 751.

176. M. Glerup, O.F. Nielsen F.W. Poulsen, J. Solid State Chem. 160 (2001) 25.

177. X. Yin, Y. Wang, F. Huang, Y. Xia, D. Wan, J. Yao, J. Solid State Chem. 184 (2011) 3324.

178. M.J.A. de Dood, J. Knoester, A. Tip, A. Polman, Phys Rev B. 71 (2005) 115102.

179. D.R. Tallant, C.H. Seager, R.L. Simpson, J. Appl Phys. 91 (2002) 4053.

180. J.C. Krupa, J. Solid State Chem. 178 (2005) 483.

181. J.M. Phillips, M.E. Coltrin, M. Crawford, A.J. Fischer, M.R. Krames, R.M. Mach, G. Mueller, Y. Ohno, L. Rohwer, J. Simmons, J. Tsao, Laser Photonics. Rev. 1 (2007) 307.

182. G. Blasse, B.C. Grabmeyer, Luminescent Materials. Springer, Berlin (1994).

183. M. Nazarov, Y. Noh, J. Rare Earths. 28 (2010) 1.

184. Z. Fu, X. Cui, S. Cui, X. Qi, S. Zhou, S. Zhang, J.H. Jeong, Crystengcomm. 14 (2012) 3915.

185. H.J. Rossel, H.G. Scott, J. Phys. Colloques. 38 (1977) C7.28.

186. T.L. Francis, P.P. Rao, M. Thomas, S.K. Mahesh, V.R. Reshmi, T.S. Sreena, Phys. Chem. Chem. Phys. 16 (2014) 17108.

187. Y. Yokogawa, M. Yoshimura, S. Somiya, Mater. Res. Bull. 22 (1987) 1449.

188. Y. Yokogawa, M. Yoshimura, S. Somiya, Solid State Ionics. 28 (1988) 1250.

189. P. Dorenbos, J. Lumin. 111 (2005) 89.

190. H.E. Hoefdraad, J. Solid State Chem. 15 (1975) 175.

191. X. Liu, L. Li, H.M. Noh, B.M. Moon, B.C. Choi, J.H. Jeong, Dalton Trans. 43 (2014) 8814.

192. P.A. Taneer, Chem. Soc. Rev. 42 (2013) 5090.

193. G. Vicentini, L.B. Zinner, J. Zukerman-Schpector, K. Zinner, Coord. Chem. Rev. 196 (2000) 353.

194. E.M. Arico, L.B. Zinner, C. Apostolidis, E. Dornberger, B. Kanellakopulos, J. Rebizant, J. Alloys. Comp. 249 (1997) 111.

195. R.A. SaFerreira, S.S. Nobre, C.M. Granadeiro, H.I.S. Nogueira, L.D. Carlos, O.L. Malta, J. Lumin. 121 (2006) 561.

196. Y. Huang, H. Seo, J. Mater. Lett. 84 (2012) 107.

197. R. Skaudzius, A. Katelnikovas, D. Enseling, A. Kareiva T. Justel, J. Lumin. 147 (2014) 290.

198. O.L. Malta, H.F. Britob, J.F.S. Menezes, F.R. Goncalves e Silva, S. Alves, F.S. Farias, A.V.M. de Andrade, J. Lumin. 75 (1997) 255.

199. R.D. Peacock, Structure and Bonding, 22 (1975) 83.

200. S. Ishihara, M. Tachiki, T. Egami, Phys. Rev. B. 49 (1994) 16123.

201. M. Kumar, T.K. Seshagiri, S. Godbole, Physica B. 410 (2013) 141.

202. Y. Su, L. Li, G. Li, Chem. Mater. 20 (2008) 6060.

203. C. Peng, H. Zhang, J. Yu, Q. Meng, L. Fu, H. Li, L. Sun, X. Guo, J. Phys. Chem. B. 109 (2005) 15278.

204. C.R. Paula, S. Santos, H.I.S. Nogueira, V. Felix , M.G.B. Drew, R.A. Sa Ferreira, L.D. Carlos, T. Trindade, Chem. Mater. 15 (2003) 100.

205. R.A. SaFerreira, L.D. Carlos, R.R. Goncalves, S.J.L. Ribeiro, V.Z. Bermudez, Chem. Mater. 13 (2001) 2991.

206. L.D. Carlos, Y. Messaddeq, H.F. Brito, R.A. SaFerreira, V.Z. Bermudez, S.J. Ribeiro, L. Adv. Mater. 12 (2000) 594.

207. J. Tang, J. Gao, J. Chen, L. Hao, X. Xu, M. Lee, Comp. Mater. Sci. 79 (2013) 478.

208. G. Chena, H. Takenoshitaa, J. Kondoa, N. Kamegashiraa, J. Alloys Compd. 359 (2003) 209.

209. S. Ueno, K. Takasaka, H. Saito-Nakano, K. Enami, N. Kamegashira, Mater. Lett. 28 (1996) 269.

210. I. Levin, T.G. Amos, J.C. Nino, T.A. Vanderah, C.A. Randall, M.T. Lanaganw, J. Solid State Chem. 168 (2002) 69.

211. G. Chen, H. Takenoshita, N. Kamegashira, J. Alloys Compd. 238, (1996) 28.

212. H. Wang, S. Kamba, M. Zhang, X. Yao, S. Denisov, F. Kadlec, J. Petzelt, J. Appl. Phy. 100 (2006) 1.

213. X. Liu, K. Han, M. Gu, L. Xiao, C. Ni, S. Huang, B. Liu, Solid State Commun. 142 (2007) 680.

214. P. Du, L.K. Bharat, J.S. Yu, J. Alloys Compd. 633 (2015) 37.

215. R. Cao, G. Chen, X. Yu, C. Cao, K. Chen, P. Liu, S. Jiang, J. Solid State Chem. 220 (2014) 97.

216. W. Liu, C.C. Lin, Y. Chiu, Y. Yeh, S. Jang, R. Liu, Opt. Exp. 18 (2010) 2946.

217. Q. Zhang, H. Sun, T. Kuang, R. Xing, X. Hao, RSC Adv. 5 (2015) 4707.

218. P. Yu, L. Su, J. Xu, Opt. rev. 21 (2014) 455.

219. Z. Liang, F. Mo, X. Zhang, L. Zhou, J. Lumin. 151 (2014) 47.

220. R. K. Datta, J. Electrochem. Soc. 114 (1967) 1057.

221. S. Li, X. Li, K. Deng, X. Wei, Y. Chen, Y. Chen, J. Nanosci. Nanotechnol. 14 (2014) 3631.

222. M. Thomas, P.P. Rao, S.K. Mahesh, L. SandhyaKumari, P. Koshy, Phys. Status Solidi A. 208 (2011) 2170.

223. H. Zhu, Z. Xia, H. Liu, R. Mi, Z. Hui, Mater. Res. Bull. 48 (2013) 3513.

224. K. Fengwen, H. Yihua, W. Haoyi, J. Guifang, M. Zhongfei, L. Nana, J. Rare Earths. 29 (2011) 837.

225. G.M. Veith, M.V. Lobanov, T.J. Emge, M. Greenblatt, M. Croft, F. Stowasser, J. Haderman, G.V. Tendeloo, J. Mater. Chem. 14 (2004) 1623.

226. W.M. Yen, S. Shionoya, H. Yamamoto, Phosphor Handbook, Taylor & Francis Group, Florida (2006).

227. A. Xie, X. Yuan, S. Hai, J. Wang, F. Wang, L. Li, J. Phys. D: Appl. Phys. 42 (2009) 1.

List of publications in SCI journals

1. **Linda Francis T.**, P. Prabhakar Rao, S.K. Mahesh, V.R. Reshmi, Sreena T.S., Parvathi S. Babu, "Novel red phosphors Gd_2GaTaO_7 : Eu^{3+}, Bi^{3+} for white LED applications," J. Mater Sci: Mater Electron 26 (2015) 5743–7.

2. **Linda Francis T.**, P. Prabhakar Rao, Mariyam Thomas, S.K. Mahesh, V.R. Reshmi, T.S. Sreena, "Structural influence on the photoluminescence properties of Eu^{3+} doped Gd_3MO_7 (M = Nb, Sb,Ta) red phosphors," Phys. Chem. Chem. Phys. 16 (2014) 17108 -15.

3. **Linda Francis T.**, P. Prabhakar Rao, Mariyam Thomas, S.K. Mahesh, V.R. Reshmi, "Effect of Zr^{4+} and Si^{4+} substitution on the luminescence properties of $CaMoO_4$: Eu^{3+} red phosphors," J. Mater Sci: Mater Electron 25(2014) 2387-93.

4. **Linda Francis T.**, P. Prabhakar Rao, Mariyam Thomas, S.K. Mahesh, Reshmi V.R., "New orange-red emitting phosphor La_3NbO_7 : Eu^{3+} under blue excitation," Mat. Lett, 81 (2012) 142-4.

5. **Linda Francis T.**, P. Prabhakar Rao, S.K. Mahesh, V.R. Reshmi, Sreena T.S., Parvathi S. Babu, "Effect of host structure on the photoluminescence properties of Eu^{3+} doped Ln_3TaO_7 (Ln = La, Gd, Y, Lu) red phosphors," (communicated)

6. T.S. Sreena, P. Prabhakar Rao, **Linda Francis T.**, Athira K.V. Raj Parvathi S. Babu, "Structural and photoluminescence properties of stannate based displaced pyrochlore-type red phosphors: $Ca_{3-x}Sn_3Nb_2O_{14}$:$x$$Eu^{3+}$," Dalton Trans. 44 (2015) 8718-28.

7. Mahesh S.K., Prabhakar Rao P., **Linda Francis,** Peter Koshy, "Intense red line emitting phosphor $LuNbO_4$: Eu^{3+} for white light emitting diode applications," Mater. Lett. 120 (2014) 115–7.

8. Mahesh S.K., Prabhakar Rao P., Mariyam Thomas, **Linda Francis,** Peter Koshy, "Influence of cation substitution and activator site exchange on the photoluminescence properties of Eu^{3+} doped quaternary pyrochlore oxides," Inorg. Chem. 52 (2013) 13304–13.

9. V.R. Reshmi, P. Prabhakar Rao, Mariyam Thomas, S.K. Mahesh, **Linda Francis**, "Enhanced Eu^{3+} red luminescence in scheelite based oxides, $CaLaSbWO_8$," ECS J. Solid State Technol. 2 (2013) R44-8.

10. Mariyam Thomas, P. Prabhakar Rao, S.K. Mahesh, V.R. Reshmi, **T. Linda Francis**, Peter Koshy, "Improvement of morphology and luminescence properties of powellite type red phosphors $CaGd_{1-x}NbMoO_8 : x$$Eu^{3+}$ synthesized via citrate gel route," J. Am. Ceram. Soc. 95 (2012) 2260-5.

List of conference papers

1. **Linda Francis T**., P. Prabhakar Rao, Mahesh S.K., Reshmi V.R., Sreena T.S., Parvathi S. Babu, "Effect of Ba^{2+} substitution in Ln^{3+} site in the photoluminescence properties of Eu^{3+} activated Ln_3MO_7 Red Phosphors," International Conference on Luminescence and its Applications (ICLA), Bangalore, February 9-12, 2015.

2. **Linda Francis T**., P. Prabhakar Rao, Mahesh S.K., Reshmi V.R., Sreena T.S., "Photoluminescence properties and the structural studies of Eu^{3+} doped Gd_3MO_7 (M = Nb, Sb, Ta)," International conference on advanced functional materials (ICAFM), Thiruvananthapuram, February 19-21, 2014.

3. **Linda Francis T.**, Prabhakar Rao P., Anila Raj, Mariyam Thomas, Mahesh S.K., Reshmi V.R., "Enhanced photoluminescence Of $CaMoO_4 : Eu^{3+}$ red phosphors by $ZrSiO_4$ addition," 25th Kerala science congress, Technopark, Trivandrum, 29-31, January 2013.

4. **Linda Francis T**., P. Prabhakar Rao, Mariyam Thomas, Mahesh S.K., Reshmi V.R., "Photoluminescence properties of new $Gd_2GaTaO_7 : Eu^{3+}$, Bi^{3+} red phosphors; National Conference on Luminescence & its Applications (NCLA), Bangalore, January 8-10, 2013.

5. **Linda Francis T**, P. Prabhakar Rao, M. Thomas, S.K. Mahesh, V.R. Reshmi., "Intense orange-red emitting phosphor $La_3NbO_7:Eu^{3+}$ under blue excitation," International Conference on Luminescence & its Applications (ICLA), Hyderabad, February 7-12, 2012.

6. **Linda Francis T**, P. Prabhakar Rao, Mariyam Thomas, S.K. Mahesh, V.R. Reshmi., "Photoluminescence properties in new pyrochlore type oxides $Gd_{3-x}Y_xMO7:yEu^{3+}$ [M=Nb, Ta, Sb]," National Conference on

Science, Technology and Applications of Rare earths (STAR), Munnar, Kerala, August 19-20,2011.

7. S.K. Mahesh, P. Prabhakar Rao, **T. Linda Francis**, V.R. Reshmi, T.S. Sreena, Peter Koshy. "Luminescence enhancement through compositional modifications in quaternary pyrochlore type red phosphors for pc-WLED applications," International conference on advanced functional materials (ICAFM), Thiruvananthapuram, February 19-21, 2014.

8. V.R. Reshmi, P. Prabhakar Rao, Mariyam Thomas, S.K. Mahesh, **Linda Francis**, "New molybdenum based pyrochlore type red phosphors $KGd_{1-x}SnMoO_7 : x$Eu^{3+}," International Conference on Luminescence & its Applications (ICLA), Hyderabad, February 7-12, 2012.

9. Mariyam Thomas, P. Prabhakar Rao, S.K. Mahesh, V.R. Reshmi, **Linda Francis T.**, Peter Koshy. "Luminescence properties of Bi^{3+} co-activated novel red phosphors $CaGd_{0.75-y}NbWO_8$: *0.25*Eu^{3+}, *y*Bi^{3+} for white light emitting diodes," National Conference on Science, Technology and Applications of Rare earths (STAR), Munnar, Kerala, August 19-20, 2011.

10. V.R. Reshmi, P. Prabhakar Rao, Mariyam Thomas, S.K. Mahesh, **Linda Francis T.**, "New Powellite based red phosphors $CaLa_{1-x}NbMo/WO_8 : x$Eu^{3+} for WLED applications," National Conference on Science, Technology and Applications of Rare earths (STAR), Munnar, Kerala, August 19-20, 2011.

11. Mariyam Thomas, P. Prabhakar Rao, S.K. Mahesh, V.R. Reshmi, **Linda Francis T.**, Peter Koshy., "Synthesis and luminescent properties of novel red phosphors $CaGd_{1-x}NbMoO_8 : x$Eu^{3+} for white light emitting diodes," 23rd Kerala science congress, Thiruvananthapuram, Kerala, January 29-31, 2011.

12. S.K. Mahesh, P. Prabhakar Rao, Mariyam Thomas, V.R. Reshmi, **T. Linda Francis**, Peter Koshy., "Red luminescence in Stannate Based Pyrochlore type phosphors $CaYSnNbO_7 : $ Eu^{3+}," 7th National Symposium and conference on Solid state Chemistry and Allied areas (ISCAS), Thiruvananthapuram, Kerala, November 24-26, 2011.